# **Springer Theses**Recognizing Outstanding Ph.D. Research

Jinsong Zhang

Transport Studies of the Electrical, Magnetic and Thermoelectric Properties of Topological Insulator Thin Films



# **Springer Theses**

Recognizing Outstanding Ph.D. Research

#### **Aims and Scope**

The series "Springer Theses" brings together a selection of the very best Ph.D. theses from around the world and across the physical sciences. Nominated and endorsed by two recognized specialists, each published volume has been selected for its scientific excellence and the high impact of its contents for the pertinent field of research. For greater accessibility to non-specialists, the published versions include an extended introduction, as well as a foreword by the student's supervisor explaining the special relevance of the work for the field. As a whole, the series will provide a valuable resource both for newcomers to the research fields described, and for other scientists seeking detailed background information on special questions. Finally, it provides an accredited documentation of the valuable contributions made by today's younger generation of scientists.

#### Theses are accepted into the series by invited nomination only and must fulfill all of the following criteria

- They must be written in good English.
- The topic should fall within the confines of Chemistry, Physics, Earth Sciences, Engineering and related interdisciplinary fields such as Materials, Nanoscience, Chemical Engineering, Complex Systems and Biophysics.
- The work reported in the thesis must represent a significant scientific advance.
- If the thesis includes previously published material, permission to reproduce this must be gained from the respective copyright holder.
- They must have been examined and passed during the 12 months prior to nomination.
- Each thesis should include a foreword by the supervisor outlining the significance of its content.
- The theses should have a clearly defined structure including an introduction accessible to scientists not expert in that particular field.

More information about this series at http://www.springer.com/series/8790

Transport Studies of the Electrical, Magnetic and Thermoelectric Properties of Topological Insulator Thin Films

Doctoral Thesis accepted by Tsinghua University, Beijing, China



Author
Dr. Jinsong Zhang
Tsinghua University
Beijing
China

Supervisor Prof. Yayu Wang Tsinghua University Beijing China

ISSN 2190-5053 ISSN 2190-5061 (electronic) Springer Theses ISBN 978-3-662-49925-2 ISBN 978-3-662-49927-6 (eBook) DOI 10.1007/978-3-662-49927-6

Library of Congress Control Number: 2016936971

#### © Springer-Verlag Berlin Heidelberg 2016

This work is subject to copyright. All rights are reserved by the Publisher, whether the whole or part of the material is concerned, specifically the rights of translation, reprinting, reuse of illustrations, recitation, broadcasting, reproduction on microfilms or in any other physical way, and transmission or information storage and retrieval, electronic adaptation, computer software, or by similar or dissimilar methodology now known or hereafter developed.

The use of general descriptive names, registered names, trademarks, service marks, etc. in this publication does not imply, even in the absence of a specific statement, that such names are exempt from the relevant protective laws and regulations and therefore free for general use.

The publisher, the authors and the editors are safe to assume that the advice and information in this book are believed to be true and accurate at the date of publication. Neither the publisher nor the authors or the editors give a warranty, express or implied, with respect to the material contained herein or for any errors or omissions that may have been made.

Printed on acid-free paper

This Springer imprint is published by Springer Nature The registered company is Springer-Verlag GmbH Berlin Heidelberg

### **Supervisor's Foreword**

This thesis reports systematic transport studies on the electrical, magnetic, and thermoelectric properties of topological insulator (TI)—thin films grown by molecular beam epitaxy. TI is one of the most important frontiers in condensed matter physics in recent years. Due to the existence of strong spin-orbital coupling (SOC) in TIs, the electronic band structure shows a non-trivial topology, which promotes the formation of massless Dirac fermions in the TI surfaces. These unique properties not only generate novel physical phenomena in the fundamental researches, but may also have unique applications in spintronics and quantum computation. The experimental results presented in this thesis offer useful information for understanding the peculiar properties in TIs and demonstrate the feasibility of application in future devices.

The main conclusions and contributions of this thesis are as follows:

- (1) One of the most challenging problems in TI is the elimination of bulk carriers, so that one can investigate the intrinsic properties of surface states. By using isostructural isovalent mixtures of two prototypical TIs, Bi<sub>2</sub>Te<sub>3</sub>, and Sb<sub>2</sub>Te<sub>3</sub> both of which are V-VI compounds and have opposite bulk carriers, we successfully fabricated ideal TIs with truly insulating bulk and tunable charge carriers (electron- or hole-like) in the surface states (see Chap. 3). Thermoelectric measurements reveal that when the Fermi level lies around the Dirac point, the magnetoelectric properties are dominated by the surface-state electrons, whereas the thermoelectric effect at room temperature is predominately controlled by bulk states (see Chap. 6). These results demonstrate new routes for investigating the novel quantum transport properties of the topological surface states and designing high-performance TI devices.
- (2) With increasing Se concentration in Cr-doped Bi<sub>2</sub>(Se<sub>x</sub>Te<sub>1-x</sub>)<sub>3</sub> TI thin films, we observe a magnetic quantum phase transition from ferromagnetism to paramagnetism accompanied by a sign reversal of the anomalous Hall effect. Across the critical point, a topological quantum phase transition of the band structures is confirmed by angle-resolved photoemission measurements and density functional theory calculations. Finally, the effective model calculations

- show that the bulk band topology is the fundamental driving force for the magnetic quantum phase transition. More specifically, the topologically non-trivial band structure prefers ferromagnetic ordering at low temperatures, while the topologically trivial band structure tends to form paramagnetic ordering (see Chap. 4). These findings significantly increase the understanding and controlling of the topological and magnetic properties, providing an ideal platform for realizing the exotic topological quantum phenomena induced by breaking the time reversal symmetry in magnetic TIs.
- (3) By fine tuning the chemical composition, film thickness and substrate morphology, the quantum anomalous Hall effect (QAHE) is experimentally observed in Cr-doped (Bi, Sb)<sub>2</sub>Te<sub>3</sub> TI thin films (see Chap. 5). At zero magnetic field and ultralow temperature (30 mK), the anomalous Hall resistance reaches the quantized value of  $h/e^2$  when the Fermi level is tuned into the sub-band-gap. Here h is the Planck constant and e is the elementary charge. Meanwhile, the longitudinal resistance shows a considerable drop that is consistent with the dissipationless edge state transport. Under strong magnetic fields, the longitudinal resistance totally vanishes, whereas the Hall resistance remains quantized. Moreover, the exact quantization is achieved on a macroscopic scale sample with relatively low mobility. Such a robust QAHE implies that it may be used in future low-energy-consumption electronics and quantum computation.

Beijing February 2016 Yayu Wang

#### **Abstract**

The non-trivial bulk band topology and massless surface Dirac fermions are the most peculiar features of topological insulators, which are generated by strong spin-orbit coupling and protected by the time reversal symmetry. In this thesis, we present transport studies of the electrical, magnetic and thermoelectric properties of topological insulator thin films grown by molecular beam epitaxy. The transport measurements are performed on the isostructural isovalent mixtures of Bi<sub>2</sub>Se<sub>3</sub> family compounds as well as the Cr-doped alloys in temperature range from 0.03 to 300 K and magnetic field up to 18 T. The experimental results reported here provide useful information for understanding and utilizing the unique properties of topological insulators.

The existence of significant bulk conduction is a challenging problem for the experimental observation of novel quantum phenomena in topological insulators. To eliminate the bulk-carrier contribution, we employ the band structure engineering method in  $(Bi_{1-x}Sb_x)_2Te_3$  ternary compounds. Electrical transport and angle-resolved photoemission spectroscopy (ARPES) measurements show that the Fermi energy can be tuned systematically across the Dirac point and the electrical properties are consistent with that of a single spin-polarized Dirac cone. Most remarkably, through the band engineering we have achieved ideal topological insulators with truly insulating bulk and tunable surface states. Further thermoelectric effect measurements on the same system displays a sign disparity between the Hall and Seebeck coefficients at certain Sb concentrations and temperatures, where the Hall effect has a negative sign but the thermopower is positive. Theoretical calculations and analyses reveal that this anomalous effect is produced by the high-mobility surface Dirac fermions and large bulk Seebeck effect when the Fermi level is in the vicinity of valence band maximum. Around the charge neutral point, the surface Dirac fermions always dominate electrical transport up to room temperature but the thermoelectric effect is predominately controlled by bulk electrons at high temperatures.

Breaking the time reversal symmetry is generally detrimental to the gapless surface states, but it may lead to exotic topological quantum effects. In Cr-doped  $Bi_2(Se_xTe_{1-x})_3$  topological insulator films, we observed a magnetic quantum phase

viii Abstract

transition accompanied by the sign reversal of the anomalous Hall effect. Across the same critical point, a topological quantum phase transition is revealed by both ARPES measurements and density functional theory calculations. We present strong evidence that the bulk band topology is the fundamental driving force for the magnetic quantum phase transition, where the ferromagnetic order is strongly promoted in the inverted band structures.

Based on the above experimental achievements, we have been capable of fabricating ferromagnetic insulators through band structure engineering method. In the resulting Cr-doped  $(Bi,Sb)_2Te_3$  thin films, the predicted quantum anomalous Hall effect is experimentally realized: when the Fermi level is tuned into the sub-band gap, the anomalous Hall resistance shows a quantized value of  $h/e^2$  in the absence of external magnetic field, accompanied by a considerable drop in the longitudinal resistance. Intriguingly, the exact quantization is observed on a macroscopic sample with relatively low mobility and non-zero bulk conduction. Such a robust quantum state not only reflects the topological nature of the quantum transport but also provides an ideal platform for the realization of potential application in future devices.

**Keywords** Topological insulator • Transport measurements • Magnetism • Quantum anomalous Hall effect • Thermoelectric effect

## Acknowledgments

First of all, I would like to express my sincere gratitude to my advisor Prof. Yayu Wang for his generous support, patience, and guidance in the past five years. He is a scholarly mentor and a beneficial friend with his enthusiasm for research inspiring me all the time. He not only guided me about the experimental details of low-temperature transport measurements, but also taught me the deep and insightful physics ideas. He also gave me lots of valuable suggestions on my research projects and afforded plenty of opportunities to collaborate with other outstanding research groups.

I am grateful to my colleagues in Prof. Wang's group. Dr. Minhao Liu taught me a lot, from the basic knowledge of cryogenics, to sample mounting techniques and instrument operation. Zuocheng Zhang and Minghua Guo helped me a lot with the projects in my thesis. Yang Feng manufactured the switch box and bought many useful tools. I would also like to thank Cun Ye, Xiaodong Zhou, Peng Cai and Wei Ruan for their supportive assistance and helpful discussion.

The collaboration with Prof. Qikun Xue, Prof. Ke He, and their group members has been vital to my projects. In particular, thanks to Dr. Cuizu Chang and Xiao Feng's hard work, we are never short of samples. It is pleasant and helpful to cooperate with theorists, including Prof. Wenhui Duan, Prof. Chaoxing Liu, Dr. Yong Xu, and Peizhe Tang. Support from Prof. Li Lv and his group is also greatly appreciated. I am also grateful to Prof. Ivan Bozovic and Prof. Adrian Gozar during my one-year visit in Brookhaven National Lab.

Finally, I would like to thank my family for their endless understanding and encouragement. My wife, Dan Wang, brought me love and gave me lots of supports. I really appreciate her for looking after our home.

The researches in this thesis were supported by the funding from NSF of China.

# **Contents**

1	Introduction				
	1.1	Overview of Topological Insulators	1		
	1.2	Historical Perspective of Topological Insulators	2		
	1.3	General Theory of Topological Insulators	4		
		1.3.1 Topological Band Theory	4		
		1.3.2 Topological Field Theory	7		
	1.4	Prototypical 3D Topological Materials	8		
		1.4.1 Theoretical Models	Ģ		
		1.4.2 Experimental Results	12		
	1.5	Organization	18		
	Refer	ences	19		
2	Experimental Setup and Methods				
	2.1	Helium-4 Refrigerator and Superconducting Magnet	23		
	2.2	Dilution Refrigerator	26		
	2.3	Probe Design and Temperature Control	29		
	2.4	Experimental Details of Transport Measurements			
		2.4.1 Electrical Transport Measurements	31		
		2.4.2 Thermoelectric Transport Measurements	33		
	2.5	Sample Growth by Molecular Beam Epitaxy	34		
	2.6	Angle-Resolved Photoemission Spectroscopy	36		
	Refer	ences	37		
3	Band	Structure Engineering in TIs	39		
	3.1	Band Structure Engineering in Traditional Semiconductors	39		
	3.2	Motivation and Experimental Design			
	3.3	Experimental Results			
		3.3.1 Sample Characterization	43		
		3.3.2 Electronic Structure	43		
		3.3.3 Analysis of the ARPES Data	45		

xii Contents

		3.3.4	Transport Properties	46			
		3.3.5	Effect of the Te Capping Layer	50			
	3.4	Discuss	sion and Conclusion	51			
	Refer	ences		52			
4	Торо	logy-Dri	ven Magnetic Quantum Phase Transition	55			
	4.1		ction to Magnetic Topological Insulator	55			
	4.2		tion and Experimental Design	57			
	4.3		Characterization	58			
	4.4	<u>*</u>					
		4.4.1	Magnetic Quantum Phase Transition				
			in $Bi_{1.78}Cr_{0.22}(Se_xTe_{1-x})_3$	60			
		4.4.2	Methods for the Detection of $\rho_{yx}^0$ and $x_c$	64			
		4.4.3	The High-Field Hall Effect in Bi <sub>1,78</sub> Cr <sub>0,22</sub> Te <sub>3</sub>	64			
		4.4.4	Magnetic Anisotropy Measurements				
			in $Bi_{1.78}Cr_{0.22}Te_3$	65			
		4.4.5	Further Proof of Paramagnetism in Bi <sub>1.78</sub> Cr <sub>0.22</sub> Se <sub>3</sub>	66			
	4.5	SQUID	Magnetization Measurements	67			
	4.6	ARPES	Band Mapping	69			
		4.6.1	Topological Quantum Phase Transition				
			in $Bi_{1.78}Cr_{0.22}(Se_xTe_{1-x})_3 \dots$	69			
		4.6.2	Similar Topological QPT in Bi <sub>2-y</sub> Cr <sub>y</sub> Se <sub>3</sub>				
			and $Bi_{2-y}Cr_yTe_3$	69			
	4.7	-	Functional Theory Calculations	72			
		4.7.1	Calculation Method	72			
		4.7.2	Band Structures of $Bi_{2-y}Cr_ySe_3$ and $Bi_{2-y}Cr_yTe_3$	72			
		4.7.3	The Corroboration of Topological QPT				
			in $Bi_{1.75}Cr_{0.25}(Se_xTe_{1-x})_3$	75 77			
	4.8	Relationship Between Topological QPT and Magnetic QPT					
	4.9		re Four-Band Model Calculations	77			
		4.9.1	The Spin Susceptibility in z Direction	78			
		4.9.2	Sign Change of the AHE at QCP	79			
		4.9.3	Physical Meaning and Estimation of $G_{z1}$ and $G_{z2}$	82 82			
	4.10	The van Vleck Mechanism in TIs					
	4.11						
	Refer	ences		85			
5	Quantum Anomalous Hall Effect						
	5.1		ction to QAHE	87			
	5.2	Sample Preparation and Characterization					
	5.3	Quantized Hall Resistance at Zero Magnetic Field					
	5.4	Vanishing Residual Resistance at High Magnetic Field 94					
	5.5	Evolution of QAHE with Varied Temperatures					
	5.6		sion	96			
	Refer	ences		97			

Contents xiii

6	Dich	otomy Between Electrical and Thermoelectric Properties	99		
	6.1	Introduction to Thermoelectric Effect in TIs	99		
	6.2	Experimental Design	101		
	6.3	Electrical and Thermoelectric Measurements	102		
	6.4	DFT Calculated Band Structures	104		
	6.5	Calculated Seebeck Coefficient	105		
	6.6	Discussion on the Sign Anomaly Between $R_H$ and $S_{xx}$	106		
	6.7	Conclusion	107		
	References				
7	Conc	cluding Remarks	109		
Aj	pendi	ix A: Complete Transport Results of QAHE	111		
Αį	pendi	ix B: Simple Picture for the Sign of AHE	113		

#### **Publications**

- [1] **Zhang J S\***, Chang C-Z\*, Tang P Z\*, et al. Topology-Driven Magnetic Quantum Phase Transition in Topological Insulators. Science, 2013, 339:1582–1586. (SCI, IDS Number: 114HL)
- [2] **Zhang J S\***, Chang C-Z\*, Zhang Z C, et al. Band structure engineering in  $(Bi_{1-x}Sb_x)_2Te_3$  ternary topological insulators. Nat Commun, 2011, 2:574. (SCI, IDS Number: 877EM)
- [3] **Zhang J**\*, Feng X\*, Xu Y\* et al. Disentangling the magnetoelectric and thermoelectric transport in topological insulator thin films. Phys Rev B, 2015, 91:075431
- [4] Chang C-Z\*, **Zhang J S**\*, Feng X\*, Shen Jie\*, et al. Experimental Observation of the Quantum Anomalous Hall Effect in a Magnetic Topological Insulator. Science, 2013, 340:167–170. (SCI, IDS Number: 122TO)
- [5] Chang C-Z, **Zhang J S**, Liu M H, et al. Thin Films of Magnetically Doped Topological Insulator with Carrier-Independent Long-Range Ferromagnetic Order. Adv Mater, 2013, 25:1065–1070. (SCI, IDS Number: 092AS)
- [6] Liu M H, Zhang J S, Chang C-Z, et al. Crossover between Weak Antilocalization and Weak Localization in a Magnetically Doped Topological Insulator. Phys Rev Lett, 2012, 108:036805. (SCI, IDS Number: 879KW)
- [7] Zhang Z C, Feng X, Guo M H, et al. Transport properties of Sb<sub>2</sub>Te<sub>3</sub>/Bi<sub>2</sub>Te<sub>3</sub> topological insulator heterostructures. Phys Status Solidi (RRL), 2013, 7:142-144. (SCI, IDS Number: 132LG)
- [8] Wang Q Y, Li Z, Zhang W H, et al. Interface-Induced High-Temperature Superconductivity in Single Unit-Cell FeSe Films on SrTiO<sub>3</sub>. Chinese Phys Lett, 2012, 29:037402. (SCI, IDS Number: 917CI)

xvi Publications

[9] Deng Z, Jin C Q, Liu Q Q, et al. Li(Zn,Mn)As as a new generation ferromagnet based on a I–II–V semiconductor. Nat Commun, 2011, 2:422. (SCI, IDS Number: 819DV)

[10] Deng Z, Zhao K, Gu B, et al. Diluted ferromagnetic semiconductor Li(Zn, Mn)P with decoupled charge and spin doping. Phys Rev B, 2013, 88:081203. (SCI, IDS Number: 205DD)

<sup>\*</sup>Equal contribution.

# Chapter 1 Introduction

#### 1.1 Overview of Topological Insulators

Topological insulators (TIs) are new states of quantum materials with an insulating bulk and metallic surface or edge states. These states are characterized by the spin-helical texture and Dirac-like energy dispersion, which are originated from strong spin-orbit coupling and protected by the time-reversal symmetry (TRS) [1–4]. The electrons in the gapless surface or edge states cannot be reflected backward when scattered by nonmagnetic impurities [5, 6]. These unique properties are expected to possess exotic topological quantum effects [7–9], and find applications in low-dissipation electronics and quantum computation.

The reason why TIs are called "topological" is because the wave function of electrons in the momentum space has a nontrivial topology (usually represented by a  $Z_2$  topological invariant). Topology is a branch of mathematics that studies the properties of objects that are invariant under smooth deformations. A classic example is, a doughnut could be transformed into a coffee cup but never into an orange without cutting it; this is because the topological structure of a doughnut is totally different from that of orange. The nontrivial topology ( $Z_2$  topological invariant) of the bulk band structure is discrete and cannot change as long as the material remains insulating. As a consequence, when the TI is physically connected to an ordinary insulator (including the vacuum) a metallic interface state necessarily shows up in order to close the gap at the boundary, across which the topology changes. Therefore, three-dimensional (3D) TIs are always associated with gapless surface states, and two-dimensional (2D) TIs are always associated with gapless edge states.

Ever since the discovery of TIs, the unique surface or edge states have attracted a surge of research activities. Initially, the TI researches are focused mostly on the theoretical prediction and experimental demonstration of time-reversal (TR) invariant systems, including HgTe/CdTe quantum wells [10, 11],  $Bi_xSb_{1-x}$  alloys [12, 13], and  $Bi_2Se_3$  family crystals [14–17]. After the discovery of

numerous TI materials, more and more studies are concentrating on novel quantum phenomena relevant to the known TIs, such as dissipationless transport, topological superconductor and Majorana fermions. These phenomena can only be realized by the interplay between the nontrivial topology and conventional orders, like magnetism and superconductivity.

In this thesis, we investigate the electrical, magnetic, and thermoelectric properties of TI thin films using transport experiments. We perform systematic transport measurements on TI films as a function of temperature, magnetic field, and electron density varied by electric gating or chemical doping. The experimental results reported here provide useful information for understanding and utilizing the unique properties of TIs.

#### 1.2 Historical Perspective of Topological Insulators

In the last century, one of the greatest achievements of condensed matter physics is the classification of quantum states by the principle of spontaneous symmetry breaking [18]. For instance, the formations of ferromagnetic and superconducting states are accompanied by the breaking of rotation and gauge symmetries. Moreover, the pattern of symmetry breaking could be well expressed by a specific order parameter, which has a nonzero expectation value only in the ordered state. Based on the order parameter picture, a generalized effective field theory (Landau-Ginzburg theory) has been well established and gives a universal description of quantum state of matter [19].

However, in 1980 this simple paradigm becomes invalid in explaining a new quantum state, the quantum Hall (QH) effect, discovered by von Klitzing et al. in a high-mobility 2D electron gas under high magnetic fields [20]. It was realized that no spontaneous symmetry breaking could be found during the QH phase transitions. In the QH state, the localization of electrons in the bulk and the quantization of Landau levels (LLs) give rise to vanishing longitudinal conductance as well as quantized Hall conductance (exactly integer multiples of  $e^2/h$ ) when the Fermi level lies in between Landau levels. The electric current can only be carried out by the edge states, which are dissipationless and running unidirectionally along the boundary of the sample. Two years later, it was recognized by Thouless et al. (TKNN) [21] that the precise quantization of the Hall conductivity has a topological characteristic, which can be quantitatively specified by an integer topological invariant. This so-called TKNN invariant or first Chern number is related to the Berry curvature of the Bloch wave functions calculated around the Brillouin zone (BZ) boundary [22].

The QH state can be considered as the first example of a quantum state with nontrivial topology, which is distinct from all states of matter known before. However, a strong magnetic field is needed to achieve the QH state, which explicitly breaks the TRS. From the application point of view, it is highly desirable to achieve the QH state in zero magnetic field. An important step towards this

direction was the theoretical model proposed by Haldane, who constructed a theoretical model for realizing the QH without LL on the 2D honeycomb lattice with a periodic magnetic field (but no net magnetic flux) [23]. However, Haldane's model still breaks the TRS due to the requirement of the periodic magnetic field. Moreover, it is very difficult to be realized experimentally due to the lack of appropriate material systems. Nevertheless, this model introduces a new concept to realize QH state in the absence of net magnetic field. Around the same time, Volovik showed that helium-3A film displayed a topologically nontrivial structure without any orbital LLs [24].

Another frontier in condensed matter physics is the generation and manipulation of spin currents for potential application in spintronics [25]. A well-know phenomenon in this field is the spin Hall effect (SHE). It refers to the appearance of spin accumulation on the lateral surfaces of an electric current-carrying sample, where the signs of the spin orientations are opposite on the opposing boundaries. In 2004, the experimental confirmation of SHE by Kato et al. greatly encouraged further researches on this phenomenon. It was soon recognized that the SHE in nonmagnetic systems has intrinsic and extrinsic origins, similar to the anomalous Hall effect in ferromagnets [26]. The intrinsic mechanism of SHE stems from the integration of Berry curvature over the BZ [27, 28]. Since such an integral can become finite even in an insulator, Murakami et al. [29] proposed a concept of spin Hall insulator, which is a gapped insulator but has a finite spin Hall conductivity due to a finite Berry phase of the occupied states.

The concept of spin Hall insulator motivated Kane and Mele [30], who proposed that a quantized version, the quantum spin Hall (QSH) effect, could be realized in graphene, a 2D material first discovered experimentally in the same year. Working independently, Bernevig and Zhang [31] declared the existence of QSH effect in strained semiconductors. The QSH state is essentially two copies of the QH state, where the two chiral edge states have opposite spin polarization and propagate in opposite directions. As a consequence, the TRS is preserved in the QSH state and the spin-orbit coupling (SOC) plays the essential role in opening the gap of the bulk states and polarizing the spin directions of the surface states. Unfortunately, the energy gap in graphene caused by the intrinsic SOC is extremely small [32, 33], and hence it is too difficult to observe the OSH effect.

The insulators possessing QSH effect are synonymously called the 2D TSs. In 2006, the first realistic 2D TI was predicted by Bernevig et al. [10] in HgTe/CdTe quantum wells. Soon, this prediction was identified in 2007 by König et al. [11], who observed that in four-terminal geometry the longitudinal conductance in the QSH regime is quantized to  $2e^2/h$ , independent of the width of the sample. Further, nonlocal transport measurements gave the evidence for the edge state transport as predicted by theory [34]. Most remarkably, Kane and Mele [35] recognized that the TR invariant 2D TIs can be characterized by a new topological invariant, namely  $Z_2$  index, other than the first Chern number, which is invariably zero in TR invariant systems. The  $Z_2$  classification could be expressed as follows: materials with an even number of Kramers pairs of edge states that the boundaries are topologically trivial

 $(Z_2 \text{ index} = 0)$ , while those with an odd number are topologically nontrivial  $(Z_2 \text{ index} = 1)$ .

Soon after the predictions of 2D TIs, theorists noticed that this topological classification of insulators can be generalized to 3D [36–38], where four  $Z_2$  invariants are necessary to fully characterize the topology. The first 3D TI was predicted by Fu and Kane in the  $Bi_{1-x}Sb_x$  alloys [12] within a certain range of compositions x. And this prediction was soon confirmed by angle-resolved photoemission spectroscopy (ARPES) measurements, which showed an odd number of topologically nontrivial surface states [13]. In 2009, the  $Bi_2Te_3$ ,  $Sb_2Te_3$ , and  $Bi_2Se_3$  compounds are predicted to be 3D TSs [14, 15]. ARPES experiments indeed observed a large bulk band gap and a gapless surface state with linear dispersion, consistent with the predictions [15, 16].

These pioneering theoretical and experimental works opened the floodgates of extensive researches on TIs. Besides the materials mentioned above, more and more compounds have been predicted to be TIs. Interestingly, some of these topological materials have been well studied in the field of infrared detection or thermoelectric applications. More remarkably, the topological surface states are only determined by the intrinsic nature of TIs and do not require any external conditions such as low temperatures and high magnetic field. Thus, it is not surprising that the discovery of TIs has shocked the condensed matter community and should keep thriving in the years to come.

#### 1.3 General Theory of Topological Insulators

In general, there are two groups of theories for describing the TIs, namely the topological band theory (TBT) [12, 35–39] and topological field theory (TFT) [40]. The TBT is commonly used as a precise algorithm for the computation of  $Z_2$  topological invariant in non-interacting system without disorder. However, in some cases with weak disorder and interaction, the stability of topological phase described by TBT has also been studied through the boundary theory [41–43]. Most importantly, the TBT provides a simple and easy-to-understand criterion to describe whether an insulator has nontrivial topology. In contrast, the TFT is generally valid in the interacting and disordered systems, and thus it can be used as identification for some physical responses when the topological order meets other quantum orders. At the non-interacting limit, the TFT and TBT are equivalent. In this section, both of these general theories are briefly reviewed and discussed.

#### 1.3.1 Topological Band Theory

The TBT has become an important tool in the discovery of new topological materials, although this theory is only valid for non-interacting systems. In order to

evaluate the  $Z_2$  invariants for a general band structure, several approaches have been proposed successively, such as spin Chern numbers method [44–46], topological invariants constructed from Bloch wave functions [35, 37–39], and discrete indices calculated at TR invariant momentums (TRIMs) in the Brillouin zone [12, 36]. Below, we will introduce the last method proposed by Fu and Kane because of its simplicity.

One of the basic quantities in this method is the matrix element of the TR operator  $\Theta$  between Bloch wave functions with TR conjugate momentums  $\mathbf{k}$  and  $-\mathbf{k}$ , which is defined as [39]

$$w_{mn}(\mathbf{k}) \equiv \langle u_m(-\mathbf{k})|\Theta|u_n(\mathbf{k})\rangle. \tag{1.1}$$

Here,  $u_n(\mathbf{k})$  is the periodic part of Bloch wave function for the *n*th  $(n \le 2N)$  occupied band at momentum  $\mathbf{k}$ , and  $w(\mathbf{k})$  is a  $2N \times 2N$  unitary matrix. At each TRIM  $\Gamma_i$ ,  $w(\mathbf{k} = \Gamma_i)$  is antisymmetric, and the following parameter can be defined [39]:

$$\delta_i = \frac{\sqrt{\det[w(\Gamma_i)]}}{\operatorname{Pf}[w(\Gamma_i)]},\tag{1.2}$$

in which det and Pf stand for the determinant and Pfaffian function of the antisymmetric matrix  $w(\Gamma_i)$ . Because  $\operatorname{Pf}[w(\Gamma_i)]^2 = \det[w(\Gamma_i)]$ , then we have  $\delta_i = \pm 1$ . To avoid the ambiguity in the sign of  $\delta_i, u_n(\mathbf{k})$  is required to be continuous throughout the BZ.

For a given 2D surface, the TR polarization associated with surface momentum  $\Lambda_a$  was found to be

$$\pi_a = \delta_{a1}\delta_{a2}.\tag{1.3}$$

Thus, for 2D TSs, the  $Z_2$  invariant  $v_{2D}$  can be defined as

$$(-1)^{\nu_{2D}} = \prod_{a=1}^{2} \pi_a = \prod_{i=1}^{4} \delta_i, \tag{1.4}$$

where i = 1, 2, 3, and 4, labeling the four TRIMs in the 2D Brillouin zone. The invariant  $v_{2D}$  is gauge invariant and only has two values. That is,  $v_{2D} = 0$  implies a trivial insulator, while  $v_{2D} = 1$  implies a TI.

The reason why there are only two possible topological classifications of the band insulators with TRS could be easily understood by the way in which Kramers pairs of the surface or edge states are connected. This is also called bulk-edge correspondence in topological phases. Because the Kramers' theorem requires that the surface or edge states should be twofold degenerate at the TRIMs  $\Gamma_a = 0$  and  $\Gamma_b = \pi/a$  (which is the same as  $-\pi/a$ ). Away from these special points, a spin-orbit interaction will split the degeneracy. And there are two ways that the states at the

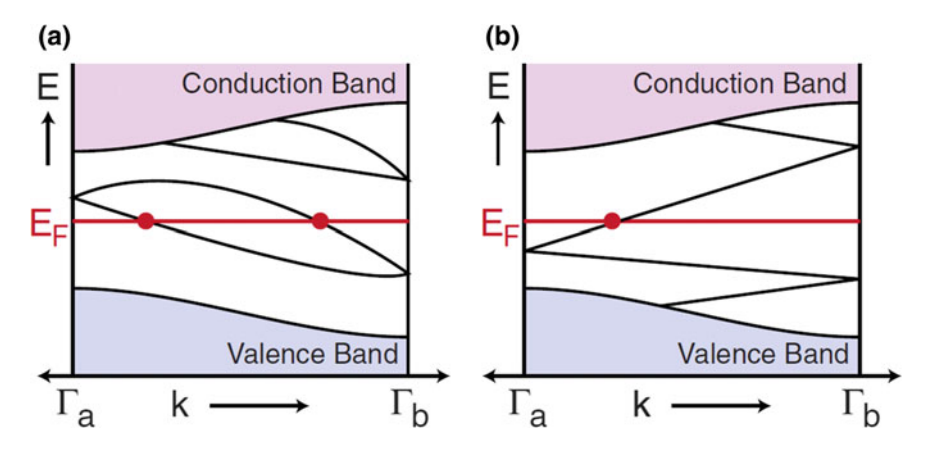


Fig. 1.1 Schematic electronic dispersion between two TRIMs,  $\Gamma_a$  and  $\Gamma_b = \pi/a$ . The surface or edge states at  $\Gamma_a$  and  $\Gamma_b$  can be connected to each other in two possible ways. In **a** the number of surface states crossing the Fermi energy  $E_{\rm F}$  is even, whereas in **b** it is odd. An odd number of crossing time leads to topologically protected metallic boundary states. Reprinted with permission from Ref. [2]. Copyright 2010 by American Physical Society

TRIMs could be connected by the surface or edge states. The first one is that the degenerate points are connected in pairs. In this case, the surface or edge bands intersect the Fermi level by even times between the two TRIMs as shown in Fig. 1.1a. In contrast, the second way is that the degenerate points are connected one by one resulting in odd numbers of crossing the Fermi level as shown in Fig. 1.1b. In the former case, the surface or edge states can be eliminated by pushing all of the bound states out of the bulk gap through weak perturbations. Thus, these bound states will not cross the Fermi level anymore and cannot exhibit any transport properties. However, in the latter case, the surface or edge states cannot be eliminated and always cross the Fermi level. Thus, these states are protected and robust again perturbations. The above argument explains straightforward the  $Z_2$  classification of gapped band insulators.

Similar to the 2D case, there are eight distinct TRIMs in the 3D Brillouin zone, which could be expressed in terms of primitive reciprocal lattice vectors as

$$\Gamma_{i=(n_1n_2n_3)} = (n_1\mathbf{b}_1 + n_2\mathbf{b}_2 + n_3\mathbf{b}_3)/2,$$
 (1.5)

with  $n_j = 0$ , 1. And they can be visualized as the vertices of a cube. Heuristically, the 3D topological (strong) invariant  $v_{\rm 3D}$  could be naturally defined as [12, 36]

$$(-1)^{\nu_{3D}} = \prod_{n_i=0,1}^{8} \delta_{i=(n_1 n_2 n_3)}.$$
 (1.6)

Besides this strong invariant  $v_{3D}$ , it has been shown that the product of any four  $\delta_i$  for which the corresponding  $\Gamma_i$  lie in the same plane is also gauge invariant [12]. This leads to the definition of three additional invariants in 3D TIs, expressed as

$$(-1)^{\nu_k} = \prod_{n_k = 1; n_{i \neq k} = 0, 1} \delta_{i = (n_1 n_2 n_3)}. \tag{1.7}$$

Here,  $(v_1 \ v_2 \ v_3)$  are also known as the weak topological invariants characterizing the band structures [12, 36–38]. Because the weak topological invariants  $v_k$  are not robust in the presence of disorders [12], the states with  $v_{3D} = 0$  and nonzero  $v_k$  are called weak TSs [36], which can also be interpreted as stacked QSH states. On the other hand,  $v_{3D}$  is more fundamental and distinguishes the strong TSs. The only TS that has been demonstrated experimentally with nonzero weak topological indices is the Bi<sub>1-x</sub>Sb<sub>x</sub> alloys [12, 13], in which  $v_{3D} = v_{k=1,2,3} = 1$ .

#### 1.3.2 Topological Field Theory

The TFT is a low-energy effective field theory which generally describes the universal topological properties of the quantum states. As that in QH system, the essential topological aspect was successfully captured by the original TFT, constructed upon the Chern-Simons term in 1989 [47]. Because the Chern-Simons term can exist in all even spatial dimensions, in 2001 Zhang and Hu [48] explicitly constructed a microscopic model to generalize the 2D QH state to a four-dimensional (4D) TR invariant state possessing an integer topological invariant. This generalization of QH state had basically removed the requirement of both the breaking of TRS and two dimensionality. Furthermore, it was demonstrated by Qi et al. [40] that the framework of 4D TFT is also useful in describing the 3D and 2D TIs, by the procedure of dimensional reduction. It is interesting to note that the natural route of TFT in describing TIs is dimensional reduction, in contrast to the dimensional increase procedure of TBT.

In general, the TFT can be defined for all kinds of insulators, with or without interactions. From this point of view, the TFT is more suitable for describing the electromagnetic response and predicting novel quantum effects in TIs [8, 9]. Even though the mathematical calculations are rather complex in TFT, Qi and Zhang [3] gave an intelligible explanation based on the elementary concepts in electromagnetism as shown in the following.

Inside an insulator, the electrical field  $\bf E$  and the magnetic field  $\bf B$  are both well defined. Thus, they define a topological term in the action of electromagnetic field:

$$S_{\theta} = \frac{\theta \alpha}{4\pi^2} \int d^3x dt \, \mathbf{E} \cdot \mathbf{B}, \tag{1.8}$$

in which  $\alpha=e^2/\hbar c$  is the fine-structure constant, and  $\theta$  is a parameter. Generally speaking, the action  $S_{\theta}$  is not invariant under TR operation because of the existence of **B** field in Eq. (1.8). However, in a periodic system when  $\theta=0$  or  $\pi$ , TRS could be preserved [40]. This conclusion can be easily understood by an analogy to a one-dimensional (1D) ring with a magnetic flux inside. Usually, the magnetic flux would break the TRS, whereas, for two special values of the flux, namely  $\Phi=0$  or  $\Phi=hc/2e$ , an electron's wave function just changes its phase by 0 or  $\pi$  when the electron is circling the ring either clockwise or counterclockwise, thus, TR symmetry is maintained. Moreover, an effective action  $S_{\theta}$  could be obtained by integrating out all the microscopic fermionic degrees of freedom. And all of the nonmagnetic insulators in the universe could be classified into two distinct topological classes, described by the effective TFT with  $\theta=0$  or  $\pi$ . The physically measurable  $\theta$  is a universally quantized parameter, with two possible values defining the topologically trivial and nontrivial insulators, namely, the  $Z_2$  classification again.

#### 1.4 Prototypical 3D Topological Materials

Up to now, numerous topological materials have been theoretically predicted and experimentally observed to be TIs. In general, the TIs that have been addressed experimentally could be classified into six groups: 2D quantum wells (HgTe/CdTe [11], InAs/GaSb [49]), Bi<sub>1-x</sub>Sb<sub>x</sub> (0  $\leq$  x  $\leq$  1) [13, 50, 51], Bi<sub>2</sub>Se<sub>3</sub> family (single crystals [15–17], alloys [52–55]), TlBiM<sub>2</sub> (M = Se, Te, or S) [56–58], AB<sub>2m</sub>Te<sub>3m+1</sub> (A = Ge, Pb; B = Bi, Sb; m = 1, 2) [59–61] and other heterostructures [62, 63]. In this section, we will introduce the most extensively studied 3D TIs, the Bi<sub>2</sub>Se<sub>3</sub> family, which is the primary object of research in my PhD period.

The 3D topological materials Bi<sub>2</sub>Se<sub>3</sub>, Bi<sub>2</sub>Te<sub>3</sub>, and Sb<sub>2</sub>Te<sub>3</sub> are theoretically described by a simple but realistic model, which is generalized from the basic template in the prediction of their 2D counterpart, HgTe/CdTe QWs. In these 3D TIs, the bulk band structure is inverted by the strong SOC at the  $\Gamma$  point in the BZ. Moreover, the bulk states are fully gapped, which is different from the zero-gap semiconductor HgTe. Inside the gap, there are topologically protected surface states consisting of a single Dirac cone. The 2D Dirac fermions have a special spin-helical texture, that is, the electron spins are perpendicular to their momentums, forming a left-handed or right-handed spin texture in the momentum space. The surfaces states are immune to TR invariant perturbations, but an energy gap could be opened when TR breaking perturbations are present on the surface, resulting in novel topological magnetoelectric effects [8, 9]. Soon after the theoretical prediction of 3D TI in the Bi<sub>2</sub>Te<sub>3</sub>, Sb<sub>2</sub>Te<sub>3</sub>, and Bi<sub>2</sub>Se<sub>3</sub> compounds [14], the ARPES experiments indeed observed a large bulk band gap and gapless surface states with a single Dirac cone [15, 16]. Further spin-resolved ARPES measurements observed a left-handed spin texture in the electron-type Bi<sub>2</sub>Se<sub>3</sub> and Bi<sub>2</sub>Te<sub>3</sub> crystals [64]. These pioneering theoretical and experimental works inspired much of the subsequent developments.

#### 1.4.1 Theoretical Models

 $Bi_2Se_3$ ,  $Bi_2Te_3$ , and  $Sb_2Te_3$  all crystallize in the same rhombohedral structure with space group  $D_{3d}^5$  ( $R\overline{3}m$ ) and have five atoms in the primitive unit cell as shown in Fig. 1.2. The crystal structure consists of a layered structure with individual layers forming a hexagonal lattice. Every five-atom layers stacked along the z direction form a periodic structure which is commonly called a quintuple layer (QL). Within a QL, the coupling between any neighboring layers is strong chemical binding. In contrary, the coupling between QLs is the van der Waals type and thus much weaker.

The inverted band structure of  $Bi_2Se_3$  at the  $\Gamma$  point could be understood in three successive stages: (I) chemical bonding of the atomic energy levels, (II) crystal field splitting, and (III) SOC (see Fig. 1.3). In stage (I), the chemical bonding between the p-orbitals of Bi and Se atoms within a QL produces the basic energy scale in this problem. Here, only the p-orbitals are taken into account and s-orbitals are all ignored because the electronic states near the Fermi level are mainly contributed by the p-orbitals. As a consequence of the chemical-bond hybridization, the Se-p orbitals are shifted down forming the valence bands. Similarly, the Bi p-orbitals are

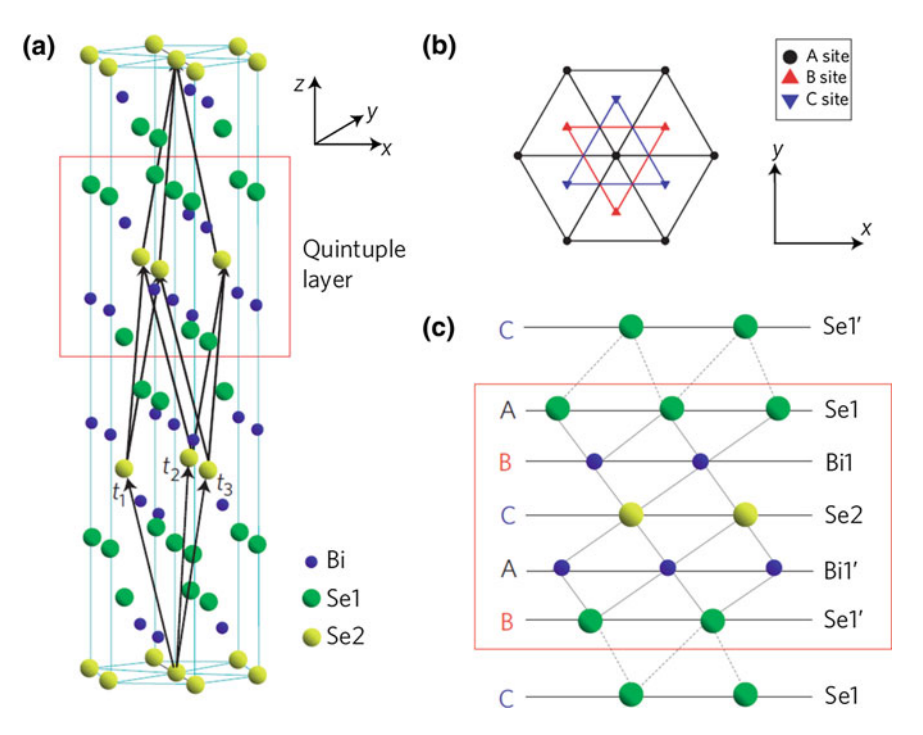
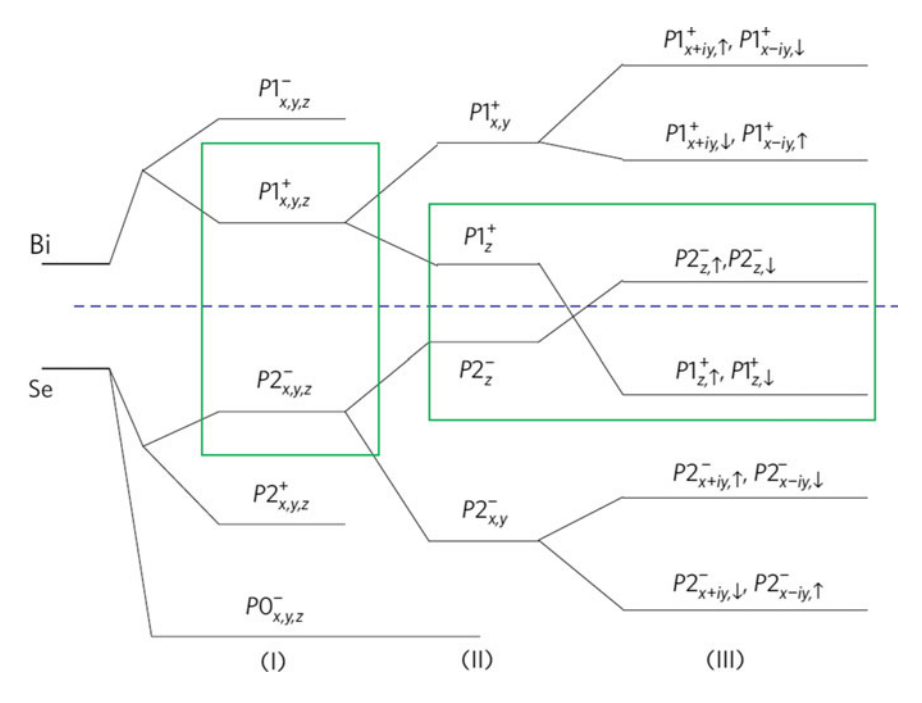


Fig. 1.2 Lattice structure of  $Bi_2Se_3$ . a The unit cell are presented by three primitive vectors labeled as  $t_{1,2,3}$ . A quintuple layer with Se1-Bi1-Se2-Bi1'-Se1' is shown in the red square both in (a) and (c). b The top view of a quintuple layer. The *triangle layers* in one quintuple layer have three different orientations. c Side view of a quintuple layer. Se2 atoms play the role of inversion centers. Reprinted by permission from Macmillan Publishers Ltd: Ref. [14], copyright 2009



**Fig. 1.3** Schematic diagram of the evolution from the atomic  $p_{x,y,z}$  orbitals of Bi and Se into the conduction and valence bands of Bi<sub>2</sub>Se<sub>3</sub> at the Γ point. The effect of chemical bonding, crystal field splitting, and SOC are presented by three different stages (*I*), (*II*) and (*III*). Fermi energy is indicated by the *blue dashed line*. The energy states enclosed by the *green box* are the closest states to the Fermi level. Reprinted by permission from Macmillan Publishers Ltd: Ref. [14], copyright 2009

lifted up forming the conduction bands. From the parity point of view, the valence band Se p-orbitals can be recombined into three states labeled as  $|P2_{x,y,z}^-\rangle$ ,  $|P2_{x,y,z}^+\rangle$  and  $|P0_{x,y,z}^-\rangle$ . Here the superscripts  $\pm$  correspond to the parity of the relevant states. Similarly, for the conduction bands, two states  $(|P1_{x,y,z}^-\rangle)$  and  $|P1_{x,y,z}^+\rangle$  are derived from the Bi p-orbitals. In stage (II), due to the effect of crystal field splitting, two  $p_z$  orbitals  $(|P1_z^+\rangle)$  and  $|P2_z^-\rangle$  are split away from the degenerate  $p_x$  and  $p_y$  orbitals and get close to the Fermi levels. In the last stage (III), the effect of SOC leads to a level repulsion between  $|P1_z^+,\uparrow\rangle$  and  $|P1_{x+iy}^+,\downarrow\rangle$  and similar combinations. Therefore, the energy state  $|P1_z^+,\uparrow\rangle$  ( $\downarrow\rangle$ )  $(|P2_z^+,\uparrow\rangle)$  is pushed down (lifted up) across the Fermi level, leading to an inverted band structure. Note that the parity between these two inverted states  $|P1_z^+,\uparrow\rangle$  ( $\downarrow\rangle$ ) and  $|P2_z^-,\uparrow\rangle$  ( $\downarrow\rangle$ ) is opposite, which drives the system into a topological nontrivial phase.

Because the physics near the  $\Gamma$  point in momentum space is solely responsible for the topological nature of Bi<sub>2</sub>Se<sub>3</sub>, it is reasonable to construct a simple and

realistic model to characterize the low-energy and long-wavelength properties in this system. By requiring the TR symmetry, inversion symmetry, and threefold rotation symmetry around the z axis, and neglecting the cubic and higher order of the  $\mathbf{k}$  terms, the effective Hamiltonian was obtained in the basis of  $|P1_z^+,\uparrow\rangle, |P2_z^+,\uparrow\rangle, |P1_z^+,\downarrow\rangle$  and  $|P2_z^-,\downarrow\rangle$ :

$$H(\mathbf{k}) = \epsilon_0(\mathbf{k})\mathbf{I}_{4\times 4} + \begin{pmatrix} \mathcal{M}(\mathbf{k}) & A_1k_z & 0 & A_2k_- \\ A_1k_z & -\mathcal{M}(\mathbf{k}) & A_2k_- & 0 \\ 0 & A_2k_+ & \mathcal{M}(\mathbf{k}) & -A_1k_z \\ A_2k_+ & 0 & -A_1k_z & -\mathcal{M}(\mathbf{k}) \end{pmatrix},$$
(1.9)

with  $k_{\pm} = k_x \pm i k_y$ ,  $\epsilon_0(\mathbf{k}) = C + D_1 k_z^2 + D_2 k_\perp^2$  and  $\mathcal{M}(\mathbf{k}) = M - B_1 k_z^2 - B_2 k_\perp^2$ . The parameters in the Hamiltonian can be determined by fitting the energy spectrum to the ab initio calculations. In spite of the  $\epsilon_0(\mathbf{k})$ , this Hamiltonian is very similar to the 3D Dirac model with uniaxial anisotropy along the z direction. Moreover, the bulk insulating gap expressed by the Dirac mass M is around 0.3 eV, which indicates the existence of topological states up to room temperature.

The topological surface states can be directly recognized on the map of local density of states (LDOS) obtained by the ab initio calculations. As shown in Fig. 1.4, for  $Sb_2Te_3$ ,  $Bi_2Se_3$ , and  $Bi_2Te_3$  the topological surface states form a single Dirac cone at the  $\Gamma$  point inside the bulk gap. However, no surface state can be found in  $Sb_2Se_3$ , indicating a topologically trivial insulator. Therefore, the

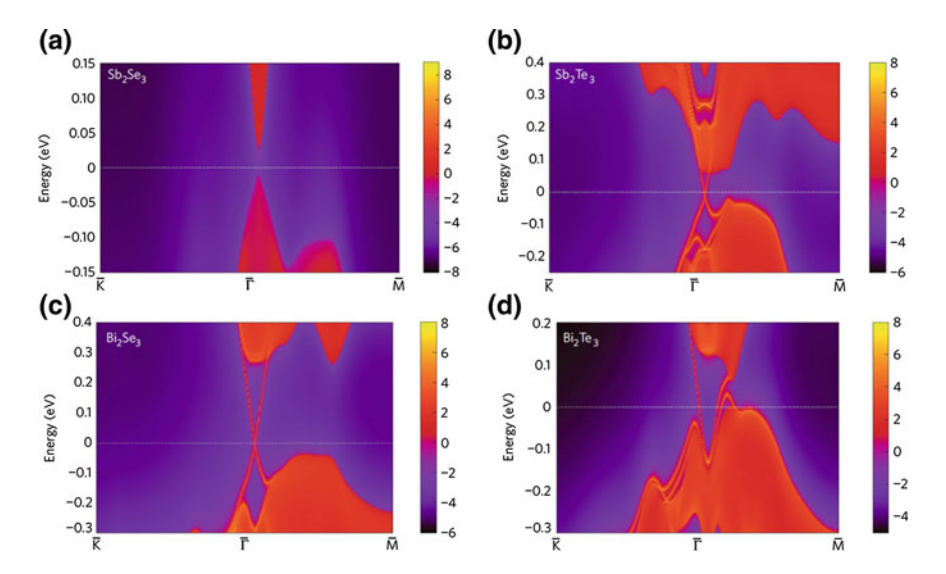


**Fig. 1.4** The LDOS on the [79] surface for  $Sb_2Se_3$  (a),  $Sb_2Te_3$  (b),  $Bi_2Se_3$  (c) and  $Bi_2Te_3$  (d) as a function of energy and momentum. Here, the *warmer colors* correspond to higher LDOS. The bulk energy bands are indicated by *red regions*. The surface states can be clearly seen around the Γ point (*red lines*) in the bulk gap for  $Sb_2Te_3$ ,  $Bi_2Se_3$ , and  $Bi_2Te_3$ . No surface state exists for  $Sb_2Se_3$ . Reprinted by permission from Macmillan Publishers Ltd: Ref. [14], copyright 2009

surface-state calculation agrees well with the bulk parity analysis, and confirms conclusively the nontrivial topology of these three materials.

On the other hand, topological surface states can also be derived from the effective model expressed in Eq. (1.9). For instance, on the half infinite space (z > 0), the surface effective model can be obtained by projecting the bulk Hamiltonian onto the surface states. To the leading order of  $k_x$ ,  $k_y$ , the effective surface Hamiltonian  $H_{\text{surf}}$  can be expressed as [14]:

$$H_{\text{surf}} = A_2 (\sigma^x k_y - \sigma^y k_x). \tag{1.10}$$

For  $A_2 = 4.1 \text{ eV} \cdot \text{Å}$ , the Fermi velocity of the surface electrons is  $v_F = A_2/\hbar \approx 6.2 \times 10^5 \text{ m/s}$ , which agrees reasonably well with ab initio result of Bi<sub>2</sub>Se<sub>3</sub> (Fig. 1.4c)  $v_F \approx 5.0 \times 10^5 \text{ m/s}$ .

#### 1.4.2 Experimental Results

ARPES measurement is an ideal method for probing the topological character of the surface states (see details in Sect. 2.6). For  $Bi_2Se_3$ , the experimental results (Fig. 1.5) show a simple surface-state spectrum in the form of a single Dirac cone located at the  $\Gamma$  point and a large bulk band gap, in accordance with the theoretical predictions. However, the Fermi level for stoichiometric  $Bi_2Se_3$  always lies in the conduction band due to the intrinsic doping effect (mostly from Se vacancies).

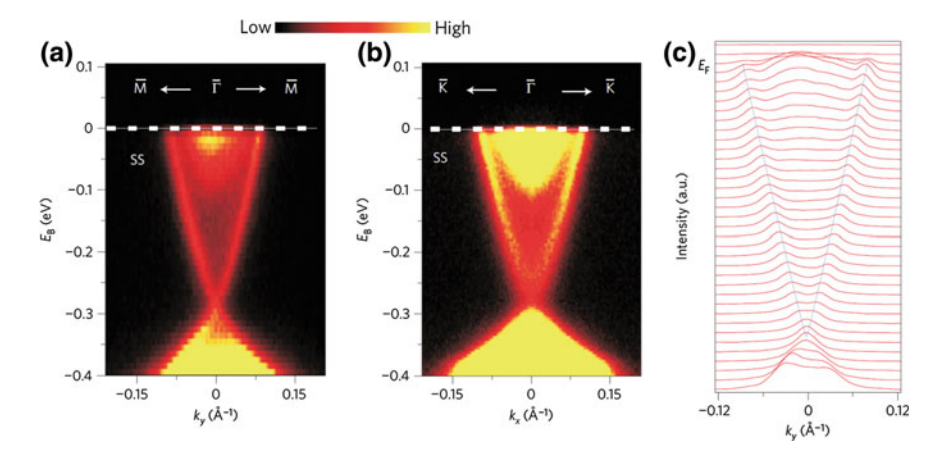


**Fig. 1.5** High-resolution ARPES measurements of surface band dispersion on Bi<sub>2</sub>Se<sub>3</sub>(111) near the  $\Gamma$  point along the **a**  $\Gamma$ -M and **b**  $\Gamma$ -K directions in the surface Brillioun zone. **c** The momentum distribution curves corresponding to (**a**) suggest that two surface bands converge into a single Dirac point at  $\Gamma$  point. The *V*-shaped surface state is nearly isotropic in the momentum plane, forming a Dirac cone in the energy–momentum space. Reprinted by permission from Macmillan Publishers Ltd: Ref. [15], copyright 2009

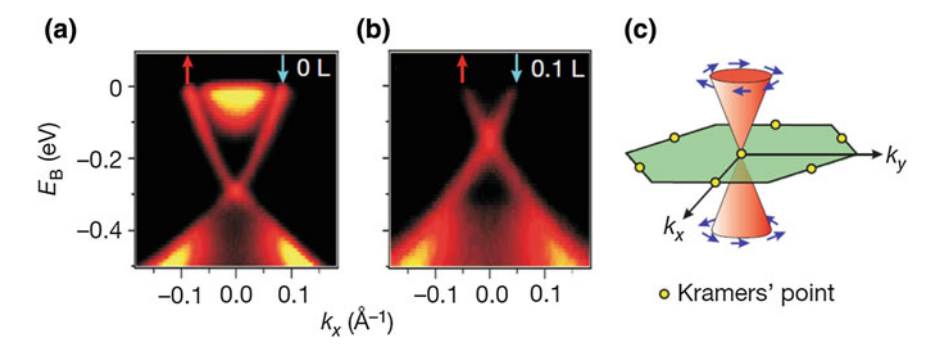


**Fig. 1.6** High resolution ARPES surface band dispersions through  $\Gamma$  point after an NO<sub>2</sub> dosage (*L*) are shown in **a** for 0 L and **b** for 0.1 L. The *arrows* denote the topological spin polarization directions. **c** Schematic of the helical Dirac fermion ground state of Bi<sub>2</sub>Se<sub>3</sub>, which exhibits a spin-polarized Dirac cone that intersects at a Kramers' point. Reprinted by permission from Macmillan Publishers Ltd: Ref. [64], copyright 2009

Thus, the sample is a fairly good metal rather than an insulator. In order to achieve a truly insulating state with the Fermi level lying in the bulk band gap, delicate chemical doping [16, 64] and alloying [52, 53] are required. In the ARPES measurements, surface deposition of NO<sub>2</sub> or alkali atom is used to change the surface chemical potential as shown in Fig. 1.6. By increasing the NO<sub>2</sub> adsorption, more hole-like carriers are introduced into the surface, and the binding energy of the surface Dirac point rises monotonically towards the Fermi level. Because the surface states are expected to be protected by TRS, the existence of Dirac cone spectrum cannot by eliminated by nonmagnetic surface disorders (such as adsorbed NO<sub>2</sub>), although the photoemission intensity is reduced. Moreover, the spin-resolved ARPES reveals that the surface Fermi surface exhibits a left-hand spin texture when the Fermi level is above the Dirac point, across which the spin chirality changes to right-hand.

When the thickness of a TI is reduced to a critical value, it is expected that the top and bottom surface states start to hybridize with each other, leading a gap opening at the Dirac point. Molecular beam epitaxy (MBE) is one of the most unique and powerful methods in growing high-quality crystalline thin films with precise control of thickness, composition, and morphology (see details in Sect. 0). Figure 1.7 shows the ARPES results of  $Bi_2Se_3$  films grown by MBE with different thicknesses (d), which reveal a gap opening process from a vanishing gap (d = 6 QL) to a gradually increasing hybridization gap (d < 6 QL) as the thickness is reduced.

Besides the ARPES characterization of the topological surface states, scanning tunneling microscopy/spectroscopy (STM/STS) is another surface-sensitive technique for measuring the surface topography and electron density of states. As shown in Fig. 1.8a, the atomically flat topography and Te-terminated hexagonal lattice structure are clearly observed on the Bi<sub>2</sub>Te<sub>3</sub> (111) surface. It is worth mentioning that the high-quality Bi<sub>2</sub>Te<sub>3</sub> film is grown by the MBE method.

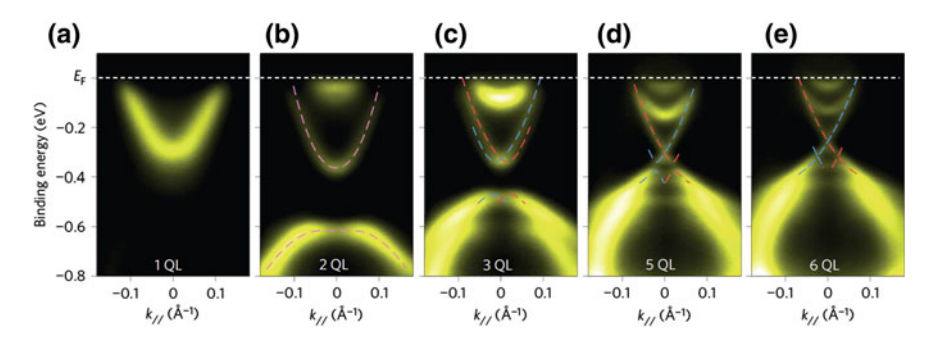


**Fig. 1.7** ARPES data for Bi<sub>2</sub>Se<sub>3</sub> thin films of thickness **a** 1 QL, **b** 2 QL, **c** 3 QL, **d** 5 QL, and **e** 6 QL, measured at room temperature. Reprinted by permission from Macmillan Publishers Ltd: Ref. [65], copyright 2010

Meanwhile, STS can detect the differential tunneling conductance dI/dV at a series of sample bias, which gives an indication of LDOS at the corresponding electron energies. This technique can provide further information about the topological surface states by detecting the interference patterns around impurities or step edges [5, 6]. When the impurities are evaporated on the surface of TIs, the surface states will be scattered and produce interference-induced standing waves around these impurities. To quantify the standing waves and obtain the scattering wave vectors, one can perform fast Fourier transformation of the interference patterns into momentum space. For instance, Fig. 1.8b shows the interference pattern in momentum space for Bi<sub>2</sub>Te<sub>3</sub> at sample bias 50 mV. In principle, all the scattering events indicated by the wave vectors  $\mathbf{q}_1$  ( $\Gamma$ -K direction),  $\mathbf{q}_2$  ( $\Gamma$ -M direction), and  $\mathbf{q}_3$ (both in  $\Gamma$ -K and  $\Gamma$ -M direction) should be possible for the Fermi surface shown in Fig. 1.8c. However, the scattering intensity along the  $\Gamma$ -K direction is strongly suppressed (Fig. 1.8b), indicating an extinction of scattering wave vector  $\mathbf{q}_1$ (and  $q_3$ ), which means the backscattering between **k** and  $-\mathbf{k}$  is prohibited. This experimental observation is consistent with theoretical predictions in TR invariant topological surface states. Furthermore, the linear dispersion of surface states can be obtained by extracting **k** from  $\mathbf{q}_2$  at a series of energies (see Fig. 1.8d). The slope of the linear fitting provides a measurement of the Dirac fermion velocity  $v_{\rm F} \approx 4.8 \times 10^5$  m/s, which is in agreement with the results from ab initial calculations (Fig. 1.4d) and ARPES experiments [16].

In addition to the absence of backscattering, STM/STS measurements provide another important result of the topological nature of surface states. That is the Landau quantization of surface states in the presence of perpendicular magnetic fields [66, 67]. As shown in Fig. 1.9, the differential tunneling spectra display a series of peaks inside the bulk band gap, which indicates the appearance of surface-state LLs. Most remarkably, the energy of zero-mode LL (n = 0) is independent of the magnetic fields and always coincides with the Dirac point. As predicted by the TFT, the existence of such mode is crucial for the topological magnetoelectric effects [8, 40]. Furthermore, the energy of LLs is linearly

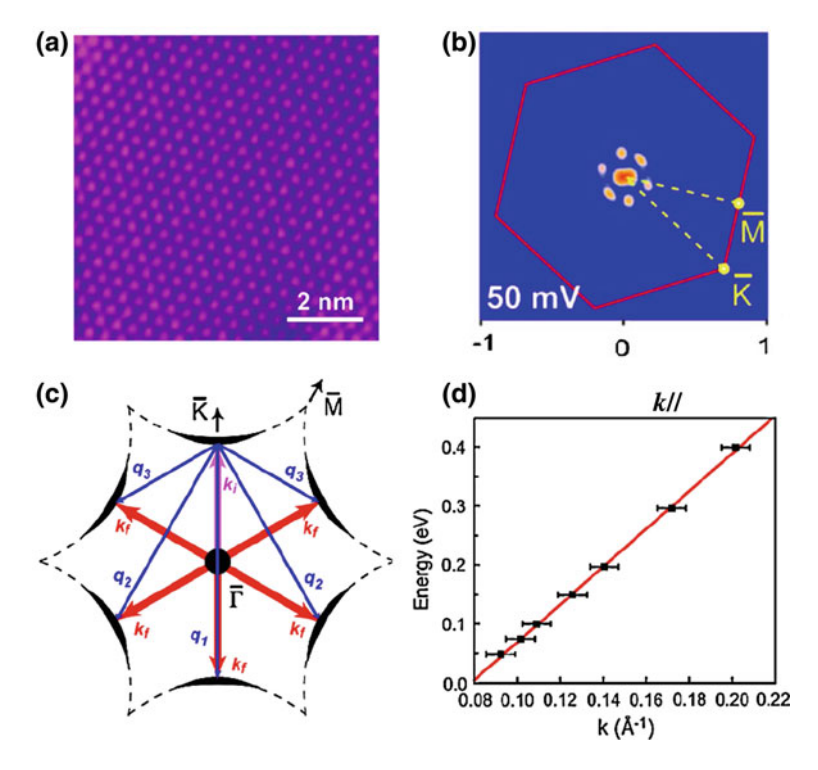


**Fig. 1.8** a The STM topography of the  $Bi_2Te_3$  (111) film with atomic-resolution. The tellurium atom spacing is about 4.3 Å. b Fast Fourier transformation power spectra of the interference pattern on  $Bi_2Te_3$  surface. The Γ-M and Γ-K directions (*yellow dashed lines*) are indicated in the Brillouin zone (*red lines*). c The possible scattering wave vectors for  $Bi_2Te_3$  are indicated by  $\mathbf{q}_{1,2,3}$  (*blue arrows*).  $k_i$  and  $k_f$  denote the wave vectors of incident and scattered states. d Linear Energy dispersion as a function of k in the Γ-K direction. Reprinted with permission from Ref. [5]. Copyright (2009) by American Physical Society

dependent on  $\sqrt{nB}$ , where n is the LL index. In contrast to normally linear-B dependence, this unusual behavior provides another evidence for the massless characteristic of the Dirac fermions.

Unlike the above surface-sensitive techniques, transport measurements are more essential and necessary for future device applications of the topological surface states. However, duo to the existence of impurities and defects, the as-grown TIs are not truly insulating but always have a finite bulk carrier concentration (see Figs. 1.5 and 1.7). The bulk contribution to transport prevents the unambiguous observation of exotic quantum effects produced by the topological surface states. Therefore, extensive efforts have been devoted to remove this obstacle. One of the most effective approaches is chemical substitution by elements with different valences [68] or alloying within the same group [52–54]. Even in the case when ARPES measurements show a Fermi level cutting through the surface states [16], transport experiments can still detect a finite bulk carrier density [53, 69, 70] in the order of

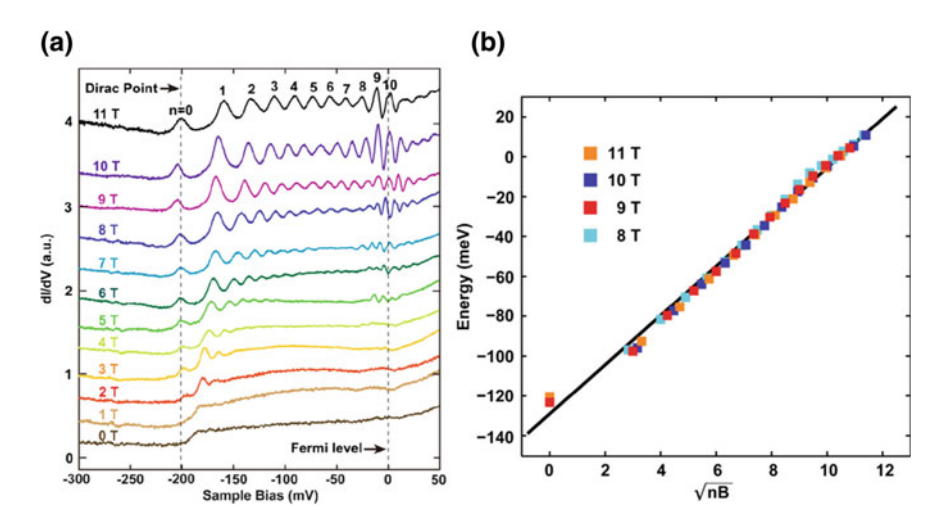


**Fig. 1.9 a** The differential tunneling spectra reveals Landau quantization of the topological surface states for 50 QL Bi<sub>2</sub>Se<sub>3</sub> with magnetic fields perpendicular to the surface. **b** Linear fitting of the LL energies to the square root of magnetic fields and LL indexes. Reprinted with permission from Ref [66]. Copyright (2010) by American Physical Society

 $10^{16} \, \mathrm{cm}^{-3}$ . This discrepancy probably arises from the formation of impurity band inside bulk band gap or band bending induced by n-type doping from air contamination.

Despite the existence of bulk carriers, the Shubnikov-de Haas (SdH) oscillations of 2D surface states have been reported in strong magnetic fields under a series of tilt angles [52, 69]. Moreover, due to the  $\pi$ -Berry phase of massless Dirac fermions [71], the linear fitting in the LL fan diagram is expected to have a 1/2 intercept as  $1/B \rightarrow 0$ . As shown in Fig. 1.10, the traces of surface-state SdH oscillations in  $\text{Bi}_2\text{Te}_2\text{Se}$  are clearly observed by the method of ionic liquid gating, which is a useful technique to introduce electrons or holes into the sample surfaces. Through extrapolating the linear fitting of index n and  $1/B_n$ , the 1/2 intercept is confirmed, reflecting the Dirac-fermion dominated electrical transport.

Another approach to eliminate the bulk conduction is to reduce the sample size down to nanoscale so that the transport contribution from surface states is comparable to or even larger than that from bulk states [73–76]. Moreover, in this approach the charge carriers can be systematically tuned by electric gating, which is unavailable in bulk materials due to the formation of depletion layer. Since most of the topological quantum effects are sensitive to the position of Fermi level, the electric gate tuning provides a valuable method for investigating exotic physical phenomena and device applications. Generally speaking, there are two kinds of gate methods, namely dielectric solid gate and ionic liquid gate. The former is usually used in thin-film and nanoscale materials, where the native oxide (silicon dioxide)

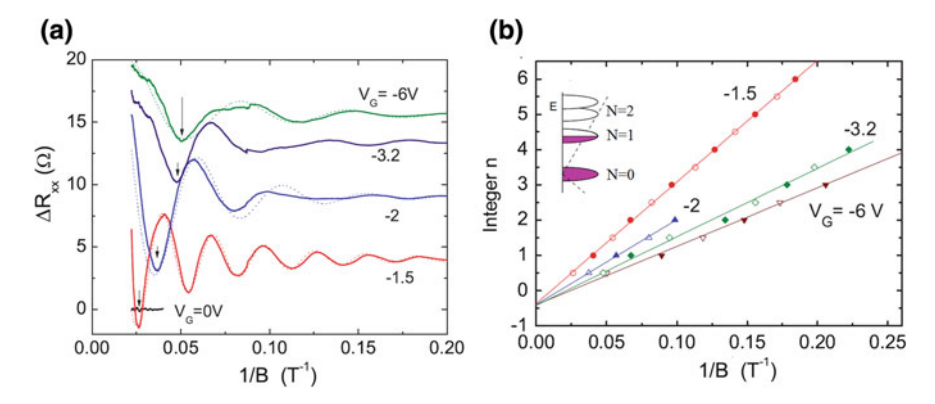
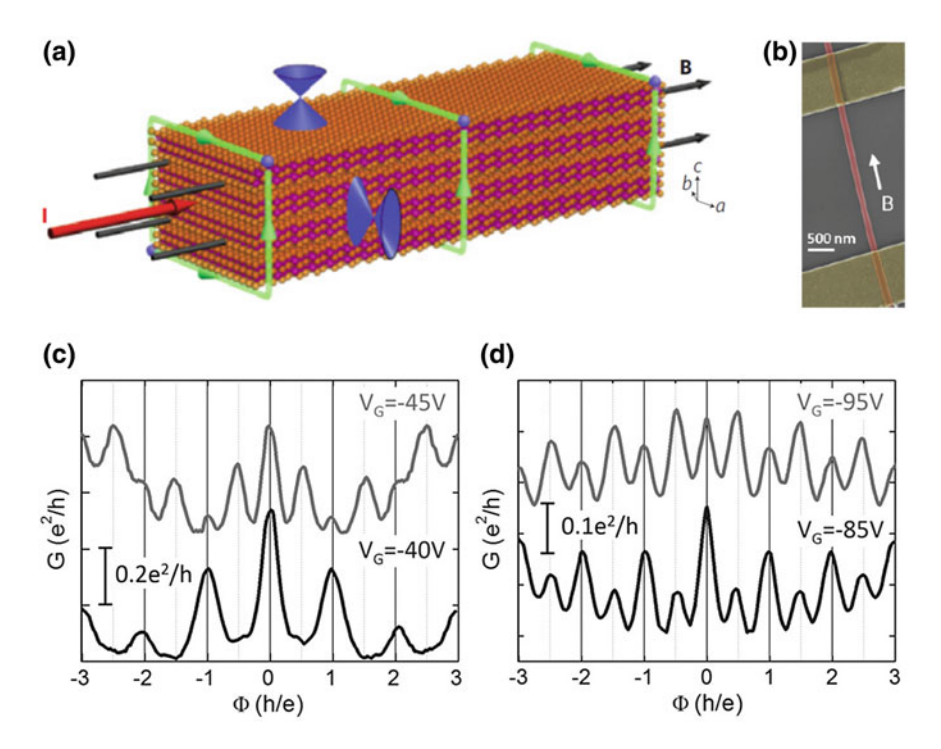


Fig. 1.10 a Traces of SdH oscillations in resistance  $\Delta R_{xx}$  after subtracting a smooth background is plotted as a function of 1/B. The oscillation amplitude and period change systematically with gate voltages  $V_G$ . The data are acquired at 1.6 K with B up to 45 T. Arrows indicate case that  $E_F$  lies in the center of broadened N=1 LL (n=1/2). b Index plots of the integer n versus  $1/B_n$  at selected  $V_G$ . In the limit  $1/B \rightarrow 0$ , the best-fit lines have a intercept at -0.45, consistent with the characteristic of Dirac fermions. The schematic structure of LLs is shown in the inset panel. Reprinted with permission from Ref [72]. Copyright (2013) by American Physical Society

or the substrate itself (SrTiO<sub>3</sub>) serves as the dielectrics. As shown in Fig. 1.11, a Bi<sub>2</sub>Se<sub>3</sub> nanoribbon coated with Se shell is synthesized on the SiO<sub>2</sub>/Si substrate. At low back-gate voltage ( $V_G = -40$  V), the conductance exhibits a quantum oscillation with period  $\Phi_0 = h/e$ , which is recognized as the Aharonov-Bohm (AB) oscillations of the surface states when a magnetic flux is enclosed [73]. However, theoretical investigations explain that this conductance oscillation with period of  $\Phi_0$  and maximum at zero flux can only be observed away from the Dirac point and in the presence of weak disorder [77, 78]. For diffusive transport, the conductance should oscillate with a period of  $\Phi_0/2$  with a maximum conductance at the conductance should oscillate with a period of  $\Phi_0/2$  with a maximum conductance at zero flux due to the interference between two time reversal paths around the nanoribbon surface. As shown in Fig. 1.11c and d, when the Fermi level is approaching the Dirac point (from  $V_G = -45$  to -95 V) the  $\Phi_0/2$  oscillation is clearly observed. These experimental results demonstrate the robustness of surface states and greatly-reduced bulk carrier density.

All these experimental studies discussed above have unambiguously proved the existence of topological surface states and found some unique properties hosted by these states. Among all the TIs, the Bi<sub>2</sub>Se<sub>3</sub> family compounds have established themselves as the most promising 3D topological materials due to the stoichiometric chemical composition, single Dirac cone and large bulk band gap. To investigate and utilize the topological nature of surface states, thin films are ideal structures in reducing the bulk carrier contributions. Among all sample growth methods, MBE is the one with the most accurate control of chemical composition and film thickness. Considering these reasons, the transport study of Bi<sub>2</sub>Se<sub>3</sub> family thin films grown by means of MBE is chosen as the primary project in this thesis.



**Fig. 1.11 a** Schematic diagram of  $Bi_2Se_3$  nanoribbon grown by vapor-liquid-solid method. Reprinted with permission from Ref. [73]. Copyright (2009) by American Physical Society. **b** SEM image of a nanoribbon, coated with an amorphous Se shell. **c**, **d** Quantum interferences of  $Bi_2Se_3$  nanoribbon in a parallel magnetic field at different back-gate voltages. A clear modulation of the conductance with the period of h/e and h/2e is observed. Reprinted with the permission from Ref. [74]. Copyright (2014) American Chemical Society

#### 1.5 Organization

In Chap. 2, we will describe the experimental setup as well as the measurement methods of electrical and thermoelectric transport properties in TI films. Chapter 3 presents the band structure engineering in  $(Bi_{1-x}Sb_x)_2Te_3$  films, which leads to ideal TIs with truly insulating bulk and tunable surface states. Chapter 4 will reveal relationship between topology and magnetism in Cr-dope  $Bi_2(Se_xTe_{1-x})_3$  films. The combination of experimental measurements and theoretical calculations demonstrates a topology-driven magnetic quantum phase transition with varied Se content. Chapter 5 will show the experimental observation of quantum anomalous Hall effect in Cr-dope  $(Bi, Sb)_2Te_3$  films. Chapter 6 will display the thermoelectric measurements in  $(Bi_{1-x}Sb_x)_2Te_3$  films, which uncovers a sign anomaly between the Hall effect and thermoelectric effect. Finally, we summarize our results in Chap. 7.

References 19

#### References

- 1. Moore JE. The birth of topological insulators. Nature. 2010;464:194-8.
- 2. Hasan MZ, Kane CL. Colloquium: topological insulators. Rev Mod Phys. 2010;82:3045-67.
- 3. Qi X-L, Zhang S-C. The quantum spin Hall effect and topological insulators. Phys Today. 2010;63:33-8.
- 4. Qi X-L, Zhang S-C. Topological insulators and superconductors. Rev Mod Phys. 2011;83:1057–110.
- 5. Zhang T, Cheng P, Chen X, et al. Experimental demonstration of topological surface states protected by time-reversal symmetry. Phys Rev Lett. 2009;103:266803.
- Alpichshev Z, Analytis JG, Chu JH, et al. STM imaging of electronic waves on the surface of Bi<sub>2</sub>Te<sub>3</sub>: topologically protected surface states and hexagonal warping effects. Phys Rev Lett. 2010;104:016401.
- Fu L, Kane CL. Superconducting proximity effect and Majorana fermions at the surface of a topological insulator. Phys Rev Lett. 2008;100:096407.
- 8. Qi XL, Li R, Zang J, et al. Inducing a magnetic monopole with topological surface states. Science. 2009;323:1184–7.
- 9. Yu R, Zhang W, Zhang HJ, et al. Quantized anomalous Hall effect in magnetic topological insulators. Science. 2010;329:61–4.
- 10. Bernevig BA, Hughes TL, Zhang S-C. Quantum spin Hall effect and topological phase transition in HgTe quantum wells. Science. 2006;314:1757–61.
- 11. König M, Wiedmann S, Brüne C, et al. Quantum spin Hall insulator state in HgTe quantum wells. Science. 2007;318:766–70.
- 12. Fu L, Kane CL. Topological insulators with inversion symmetry. Phys Rev B. 2007;76:045302.
- 13. Hsieh D, Qian D, Wray L, et al. A topological Dirac insulator in a quantum spin Hall phase. Nature. 2008;452:970–4.
- 14. Zhang H, Liu C-X, Qi X-L, et al. Topological insulators in  $Bi_2Se_3$ ,  $Bi_2Te_3$  and  $Sb_2Te_3$  with a single Dirac cone on the surface. Nat Phys. 2009;5:438–42.
- 15. Xia Y, Qian D, Hsieh D, et al. Observation of a large-gap topological-insulator class with a single Dirac cone on the surface. Nat Phys. 2009;5:398–402.
- 16. Chen YL, Analytis JG, Chu J-H, et al. Experimental realization of a three-dimensional topological insulator, Bi<sub>2</sub>Te<sub>3</sub>. Science. 2009;325:178–81.
- 17. Hsieh D, Xia Y, Qian D, et al. Observation of time-reversal-protected single-Dirac-cone topological-insulator states in Bi<sub>2</sub>Te<sub>3</sub> and Sb<sub>2</sub>Te<sub>3</sub>. Phys Rev Lett. 2009;103:146401.
- Anderson PW. Basic notions of condensed matter physics. Boulder, CO: Westview Press; 1997.
- 19. Landau LD, Lifshitz EM. Statistical physics. Oxford: Pergamon Press; 1980.
- 20. Klitzing K, Dorda G, Pepper M. New method for high-accuracy determination of the fine-structure constant based on quantized Hall resistance. Phys Rev Lett. 1980;45:494–7.
- 21. Thouless DJ, Kohmoto M, Nightingale MP, et al. Quantized Hall conductance in a two-dimensional periodic potential. Phys Rev Lett. 1982;49:405–8.
- 22. Berry MV. Quantal phase-factors accompanying adiabatic changes. P Roy Soc Lond A Mat. 1984;392:45–57.
- 23. Haldane FDM. Model for a quantum Hall effect without Landau levels: condensed-matter realization of the "parity anomaly". Phys Rev Lett. 1988;61:2015–8.
- 24. Volovik GE. Quantized Hall-effect in superfluid He-3 Film. Phys Lett A. 1988;128:277-9.
- Wolf SA, Awschalom DD, Buhrman RA, et al. Spintronics: a spin-based electronics vision for the future. Science. 2001;294:1488–95.
- 26. Nagaosa N, Sinova J, Onoda S, et al. Anomalous Hall effect. Rev Mod Phys. 2010;82:1539–92.
- 27. Murakami S, Nagaosa N, Zhang S-C. Dissipationless quantum spin current at room temperature. Science. 2003;301:1348–51.

28. Sinova J, Culcer D, Niu Q, et al. Universal intrinsic spin Hall effect. Phys Rev Lett. 2004;92:126603.

- 29. Murakami S, Nagaosa N, Zhang S-C. Spin-Hall insulator. Phys Rev Lett. 2004;93:156804.
- 30. Kane CL, Mele EJ. Quantum spin Hall effect in graphene. Phys Rev Lett. 2005;95:226801.
- 31. Bernevig BA, Zhang S-C. Quantum spin Hall effect. Phys Rev Lett. 2006;96:106802.
- 32. Min H, Hill JE, Sinitsyn NA, et al. Intrinsic and Rashba spin-orbit interactions in graphene sheets. Phys Rev B. 2006;74:165310.
- 33. Yao Y, Ye F, Qi X-L, et al. Spin-orbit gap of graphene: first-principles calculations. Phys Rev B. 2007;75:041401.
- 34. Roth A, Brüne C, Buhmann H, et al. Nonlocal transport in the quantum spin Hall state. Science. 2009;325:294–7.
- 35. Kane CL, Mele EJ.  $\mathbb{Z}_2$  topological order and the quantum spin Hall effect. Phys Rev Lett. 2005;95:146802.
- Fu L, Kane CL, Mele EJ. Topological insulators in three dimensions. Phys Rev Lett. 2007;98:106803.
- Moore JE, Balents L. Topological invariants of time-reversal-invariant band structures. Phys Rev B. 2007;75:121306.
- 38. Roy R.  $Z_2$  classification of quantum spin Hall systems: an approach using time-reversal invariance. Phys Rev B. 2009;79:195321.
- 39. Fu L, Kane CL. Time reversal polarization and a  $Z_2$  adiabatic spin pump. Phys Rev B. 2006;74:195312.
- Qi X-L, Hughes TL, Zhang S-C. Topological field theory of time-reversal invariant insulators. Phys Rev B. 2008;78:195424.
- 41. Wu C, Bernevig BA, Zhang S-C. Helical liquid and the edge of quantum spin Hall systems. Phys Rev Lett. 2006;96:106401.
- 42. Xu C, Moore JE. Stability of the quantum spin Hall effect: effects of interactions, disorder, and Z<sub>2</sub> topology. Phys Rev B. 2006;73:045322.
- 43. Nomura K, Koshino M, Ryu S. Topological delocalization of two-dimensional massless Dirac fermions. Phys Rev Lett. 2007;99:146806.
- 44. Sheng DN, Weng ZY, Sheng L, et al. Quantum spin-Hall effect and topologically invariant Chern numbers. Phys Rev Lett. 2006;97:036808.
- 45. Fukui T, Hatsugai Y. Topological aspects of the quantum spin-Hall effect in graphene: Z<sub>2</sub> topological order and spin Chern number. Phys Rev B. 2007;75:121403.
- 46. Prodan E. Robustness of the spin-Chern number. Phys Rev B. 2009;80:125327.
- 47. Zhang SC. The Chern-Simons-Landau-Ginzburg theory of the fractional quantum Hall-effect. Int J Mod Phys B. 1992;6:25–58.
- 48. Zhang S-C, Hu J. A four-dimensional generalization of the quantum Hall effect. Science. 2001;294:823–8.
- 49. Knez I, Du R-R, Sullivan G. Evidence for helical edge modes in inverted InAs/GaSb quantum wells. Phys Rev Lett. 2011;107:136603.
- 50. Hsieh D, Xia Y, Wray L, et al. Observation of unconventional quantum spin textures in topological insulators. Science. 2009;323:919–22.
- Yang F, Miao L, Wang ZF, et al. Spatial and energy distribution of topological Edge states in single Bi(111) Bilayer. Phys Rev Lett. 2012;109:016801.
- 52. Ren Z, Taskin AA, Sasaki S, et al. Large bulk resistivity and surface quantum oscillations in the topological insulator Bi<sub>2</sub>Te<sub>2</sub>Se. Phys Rev B. 2010;82:241306.
- 53. Ren Z, Taskin AA, Sasaki S, et al. Optimizing  $Bi_{2-x}Sb_xTe_{3-y}Se_y$  solid solutions to approach the intrinsic topological insulator regime. Phys Rev B. 2011;84:165311.
- 54. Ji H, Allred JM, Fuccillo MK, et al. Bi<sub>2</sub>Te<sub>1.6</sub>S<sub>1.4</sub>: a topological insulator in the tetradymite family. Phys Rev B. 2012;85:201103.
- 55. Taskin AA, Ren Z, Sasaki S, et al. Observation of Dirac holes and electrons in a topological insulator. Phys Rev Lett. 2011;107:016801.
- 56. Sato T, Segawa K, Guo H, et al. Direct evidence for the Dirac-cone topological surface states in the ternary chalcogenide T<sub>1</sub>BiSe<sub>2</sub>. Phys Rev Lett. 2010;105:136802.

References 21

57. Chen YL, Liu ZK, Analytis JG, et al. Single Dirac cone topological surface state and unusual thermoelectric property of compounds from a new topological insulator family. Phys Rev Lett. 2010;105:266401.

- 58. Xu S-Y, Xia Y, Wray LA, et al. Topological phase transition and texture inversion in a tunable topological insulator. Science. 2011;332:560–4.
- Souma S, Eto K, Nomura M, et al. Topological surface states in lead-based ternary telluride Pb (Bi<sub>1-x</sub>Sb<sub>x</sub>)<sub>2</sub>Te<sub>4</sub>. Phys Rev Lett. 2012;108:116801.
- 60. Okamoto K, Kuroda K, Miyahara H, et al. Observation of a highly spin-polarized topological surface state in GeBi<sub>2</sub>Te<sub>4</sub>. Phys Rev B. 2012;86:195304.
- 61. Eremeev SV, Landolt G, Menshchikova TV, et al. Atom-specific spin mapping and buried topological states in a homologous series of topological insulators. Nat Commun. 2012;3:635.
- 62. Valla T, Ji H, Schoop LM, et al. Topological semimetal in a Bi-Bi<sub>2</sub>Se<sub>3</sub> infinitely adaptive superlattice phase. Phys Rev B. 2012;86:241101.
- 63. Nakayama K, Eto K, Tanaka Y, et al. Manipulation of topological states and the bulk band gap using natural heterostructures of a topological insulator. Phys Rev Lett. 2012;109:236804.
- 64. Hsieh D, Xia Y, Qian D, et al. A tunable topological insulator in the spin helical Dirac transport regime. Nature. 2009;460:1101–5.
- 65. Zhang Y, He K, Chang C-Z, et al. Crossover of the three-dimensional topological insulator Bi<sub>2</sub>Se<sub>3</sub> to the two-dimensional limit. Nat Phys. 2010;6:584–8.
- Cheng P, Song C, Zhang T, et al. Landau quantization of topological surface states in Bi<sub>2</sub>Se<sub>3</sub>. Phys Rev Lett. 2010;105:076801.
- 67. Hanaguri T, Igarashi K, Kawamura M, et al. Momentum-resolved Landau-level spectroscopy of Dirac surface state in Bi<sub>2</sub>Se<sub>3</sub>. Phys Rev B. 2010;82:081305.
- 68. Checkelsky JG, Hor YS, Liu MH, et al. Quantum interference in macroscopic crystals of nonmetallic Bi<sub>2</sub>Se<sub>3</sub>. Phys Rev Lett. 2009;103:246601.
- 69. Analytis JG, McDonald RD, Riggs SC, et al. Two-dimensional surface state in the quantum limit of a topological insulator. Nat Phys. 2010;6:960–4.
- 70. Xiong J, Petersen AC, Qu D, et al. Quantum oscillations in a topological insulator  $Bi_2Te_2Se$  with large bulk resistivity (6  $\Omega$  cm). Physica E. 2012;44:917–20.
- 71. Zhang Y, Tan Y-W, Stormer HL, et al. Experimental observation of the quantum Hall effect and Berry's phase in graphene. Nature. 2005;438:201–4.
- 72. Xiong J, Khoo Y, Jia S, et al. Tuning the quantum oscillations of surface Dirac electrons in the topological insulator Bi<sub>2</sub>Te<sub>2</sub>Se by liquid gating. Phys Rev B. 2013;88:035128.
- 73. Peng H, Lai K, Kong D, et al. Aharonov-Bohm interference in topological insulator nanoribbons. Nat Mater. 2010;9:225–9.
- 74. Hong SS, Zhang Y, Cha JJ, et al. One-dimensional helical transport in topological insulator nanowire interferometers. Nano Lett. 2014;14:2815–21.
- 75. Chen J, Qin HJ, Yang F, et al. Gate-voltage control of chemical potential and weak antilocalization in  $Bi_2Se_3$ . Phys Rev Lett. 2010;105:176602.
- Checkelsky JG, Hor YS, Cava RJ, et al. Bulk band gap and surface state conduction observed in voltage-tuned crystals of the topological insulator Bi<sub>2</sub>Se<sub>3</sub>. Phys Rev Lett. 2011;106:196801.
- Bardarson JH, Brouwer PW, Moore JE. Aharonov-Bohm oscillations in disordered topological insulator nanowires. Phys Rev Lett. 2010;105:156803.
- Zhang Y, Vishwanath A. Anomalous Aharonov-Bohm conductance oscillations from topological insulator surface states. Phys Rev Lett. 2010;105:206601.
- 79. Checkelsky JG, Ye J, Onose Y, et al. Dirac-fermion-mediated ferromagnetism in a topological insulator. Nat Phys. 2012;8:729–33.

## **Chapter 2 Experimental Setup and Methods**

In this chapter, the experimental details including the instrumentation and methods for transport measurements are presented. Meanwhile, the MBE method and ARPES technique are also briefly introduced since they are indispensable and complementary to transport studies of TIs. Most of the transport measurements were carried out in the transport laboratory in the physics department of Tsinghua University, while the ultralow-temperature measurements were done in the Daniel Chee Tsui lab at Institute of Physics, Chinese Academy of Science.

#### 2.1 Helium-4 Refrigerator and Superconducting Magnet

The transport measurements are mainly performed at low temperature down to 1.5 K and strong magnetic field up to 15 T in a cryostat system made by Oxford Instruments. This cryostat system consists of a low-loss helium-4 (He-4) Dewar, a superconducting magnet and a variable temperature insert.

As shown in Fig. 2.1, the main framework of the He-4 refrigerator is supported by the low-loss He-4 Dewar. The inner liquid He-4 bath is carefully designed so that the thermal conduction from the room temperature environment is almost utterly insulated. The first insulating layer is high vacuum. In between the outmost stainless steel wall and liquid He-4 bath, the outer vacuum jacket is pumped to a pressure less than 10<sup>-6</sup> mbar when the cryostat is warm. After He-4 liquid is transferred into the bath, the vacuum would become much better because the residual gas molecules are absorbed on the surfaces of the vacuum jacket. Thus, the thermal conduction through the outer vacuum jacket by ways of conduction and convection is significantly suppressed. It is worth to mention that the entire cryostat is made of stainless steel, which is a bad thermal conductor and resistive to corrosion. The second insulating layer is liquid nitrogen. Inside the outer vacuum space, a liquid nitrogen jacket is placed around (not connected to) the outside of He-4 bath. Here, liquid nitrogen serves as both a precooler and an absorber of

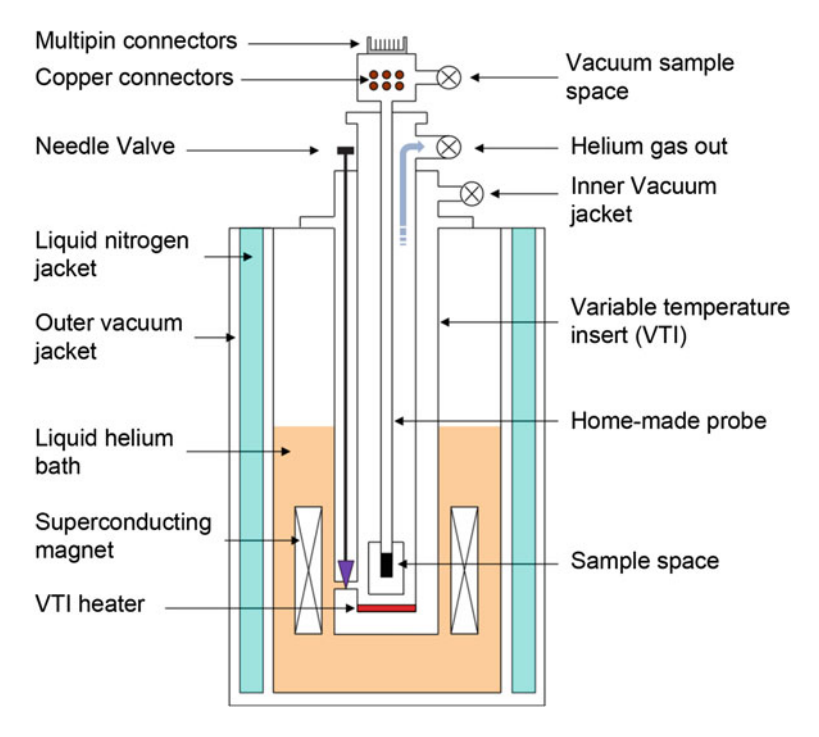


Fig. 2.1 Schematic diagram of the He-4 refrigerator and superconducting magnet with home-made transport probe inside the variable temperature insert

infrared radiation from the room temperature environment. The third insulating layer is high-reflectivity Mylar sheets. These sheets are aluminized and wrapped around the liquid nitrogen jacket as well as the bottom side of the cryostat. In this geometry, the infrared radiation at room temperature would be shielded and reflected back, protecting the inner He-4 bath from being boiled up. These three insulating layers ensure a very low loss rate of liquid helium (less than 6 L per day).

The superconducting magnet is submerged in the liquid helium bath and firmly assembled in the bottom of the cryostat. The superconducting Nb<sub>3</sub>Sn wires in the solenoids are well arranged to keep stable in case of quenching. Powered by Oxford IPS-120 current source, the magnet is capable of generating a uniform magnetic field up to 15 T either upward or downward. By pumping liquid helium to the superfluid state, the highest magnetic field can reached to 17 T.

The variable temperature insert is actually a double-layered vacuum can, which is assembled inside the bore of the magnetic coil and immersed in the He-4 liquid. The inner vacuum jacket of VTI is usually pumped to high vacuum to thermally isolate the liquid helium bath and the inner sample space. The main capability of VTI is to provide an environment with temperature continually variable from 1.5 to 300 K. The operating principle can be briefly described as follows. Through a narrow capillary, the helium liquid is siphoned into the inner space with the flow

velocity carefully controlled by a needle valve. Meanwhile, the gaseous helium is pumped out through a mechanical pump connected to the outlet of the inner space. Thus, the cooling power is generated by the evaporation process of liquid helium and cold gas flowing through the inner space. Actually, there are two working modes for VTI, that is, one-shot mode and continuous-flow mode. In one-shot mode, the needle valve is fully opened for a while, and a large amount of liquid helium is transferred into the inner space. Then, the needle valve is totally closed and no liquid comes in. Through sustained pumping, the base temperature could be achieved with a typical value of 1.3 K, which depends on the heat load and pumping speed. In continuous-flow mode, the needle valve is kept open at a delicate position and the liquid helium flows into VTI continuously. As the gaseous helium is pumped out, a wide range of temperature can be stabilized by the cooperation of an auxiliary heater on the bottom of VTI.

The experimental setup of our cryostat system is shown in Fig. 2.2. The He-4 low-loss Dewar and the supporting component form the main framework of the



Fig. 2.2 The experimental setup of cryostat system, including a He-4 low-loss Dewar, magnet and support, VTI, and dilution refrigerator. Images are adapted from <a href="http://www.oxford-instruments.com">http://www.oxford-instruments.com</a>

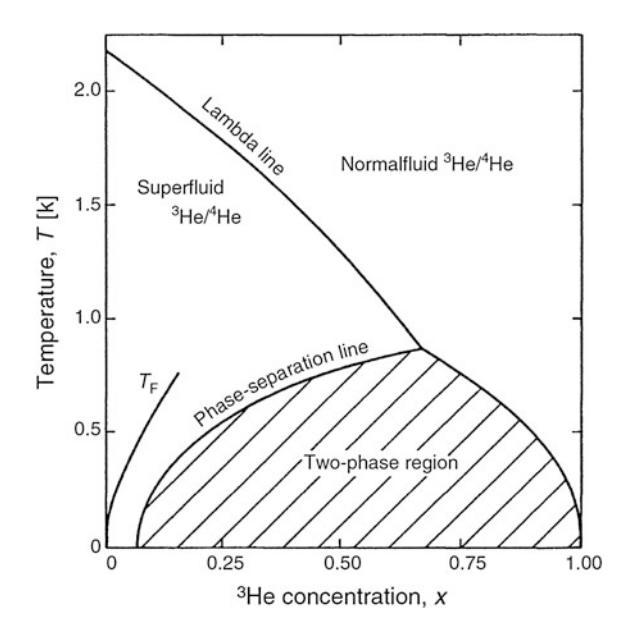
refrigerator. The VTI and dilution refrigerator (see the next section) can be inserted into the supporting component with their tails in the bore of the superconducting magnet coil.

#### 2.2 Dilution Refrigerator

A dilution refrigerator is a fantastic machine: Starting from 4.2 K, it provides continuous cooling to temperatures as low as 2 mK without moving parts in the low-temperature region [1]. The cooling power is generated by the mixing of the helium-3 (He-3) and helium-4 (He-4) isotopes. It is the only continuous refrigeration method for reaching temperatures below 0.3 K [2]. In addition, magnetic fields, often needed in low-temperature experiments, have negligible effects on its performance. Today, it is the most important refrigeration technology for the temperature range between about 5 mK and 1 K, and it is the base from which lower temperatures can be reached.

The principle of "dilution refrigerator," as its name suggests, is to use a technique called "³helium (³He)–⁴helium (⁴He) dilution." This process relies on certain thermodynamic characteristics of ³He–⁴He mixture. As shown in the phase diagram (Fig. 2.3), when cooled below the triple point ( $\sim$ 870 mK), the mixture will separate into two liquid phases, divided by a phase boundary (two-phase region). One is called the ³He-rich phase (concentrated phase), because it is essentially pure ³He at very low temperatures. This corresponds to a point on the lower right side of the diagram, below the triple point and above the phase separation line. The second

**Fig. 2.3** Phase diagram of liquid  ${}^{3}\text{He}{}_{-}^{4}\text{He}$  mixtures at saturated vapor pressure. The diagram shows the lambda line for the superfluid transition of  ${}^{4}\text{He}$ , the phase separation line of the mixtures below which they separate into a  ${}^{4}\text{He}$ -rich and a  ${}^{3}\text{He}$ -rich phase, and the line of the Fermi temperatures  $T_{\rm F}$  of the  ${}^{3}\text{He}$  component. Reprinted from Ref. [2], with a kind permission from Springer



phase is called the <sup>4</sup>He-rich phase (dilute phase), because it is mostly composed of <sup>4</sup>He, but contains at least 6 % <sup>3</sup>He at any temperature. This corresponds to a point on the lower left side of the diagram, below the triple point and above the phase separation line. A good example of these two phases would be what happens when oil and water are mixed. At a high temperature, they will stay mixed. However, when the temperature is lowered, the oil would separate from the water and float to the top (this effect can be seen at room temperature), giving two different phases in the liquid mixture. Not only that, the separated phase of oil would contain a small amount of water and vice versa.

The main components of a working dilution refrigerator and a flow diagram for its liquids are depicted in Fig. 2.4. Here, we will present a brief review of the working principles of each component, which have been described in Ref. [2]. The <sup>3</sup>He gas coming from the exit of a pump at room temperature will first be precooled by liquid nitrogen bath at 77 K and a <sup>4</sup>He bath at 4.2 K. Next, the <sup>3</sup>He enters a vacuum chamber where it is liquefied by a second <sup>4</sup>He bath at about 1.5 K (1 K pot), which is obtained by using a continuously operating He-4 refrigerator (previous section). This <sup>4</sup>He refrigerator is also used as a heat sink at which all tubes and leads going to colder parts of the refrigerator should be thermally anchored. After leaving the 1 K pot, the <sup>3</sup>He enters the main impedance, a capillary with a large flow resistance. It is further cooled by the still (described below) to a temperature 500–700 mK. Subsequently, the <sup>3</sup>He flows through a secondary impedance, followed by a series of counterflow heat exchangers where it is cooled by a cold flow of <sup>3</sup>He. Finally, the pure <sup>3</sup>He enters the upper, concentrated phase in mixing chamber, the coldest area of the dilution refrigerator.

In the mixing chamber, two phases of the <sup>3</sup>He-<sup>4</sup>He mixture, concentrated phase and dilute phase, are in equilibrium and separated by a phase boundary. Through

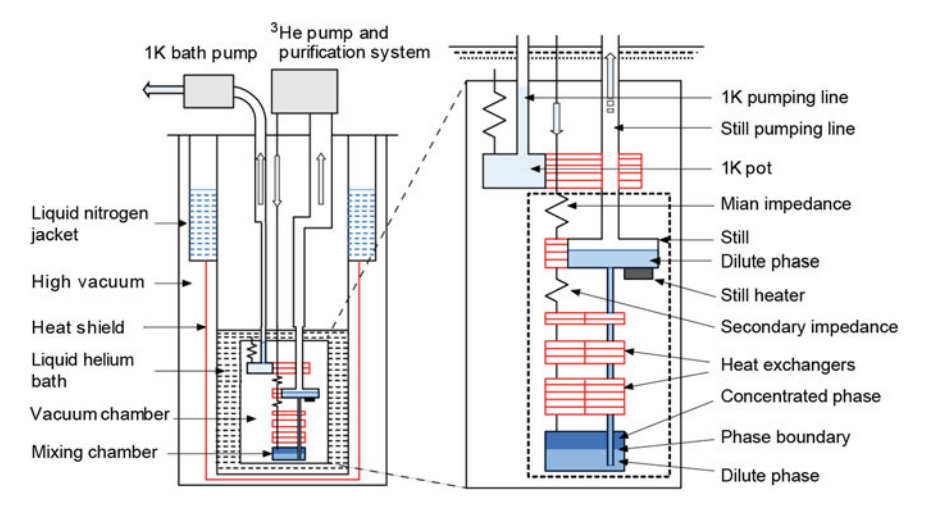
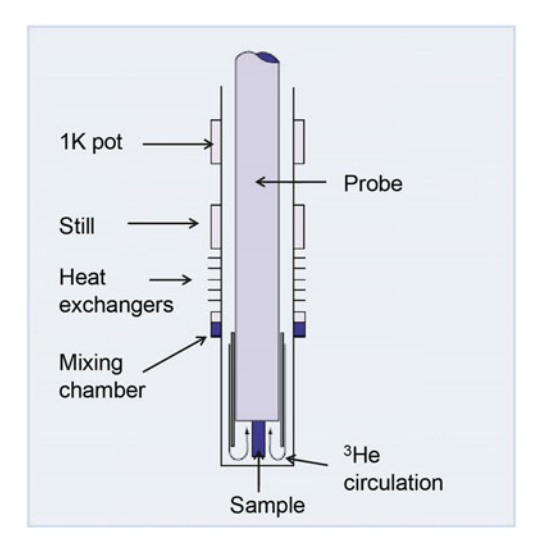


**Fig. 2.4** Schematic of  ${}^{3}\text{He}{}^{-4}\text{He}$  dilution refrigerator with enlarged low-temperature part. Adapted from Ref. [3] with the courtesy of A.T.A.M. de Waele

pumping on the dilute phase, most of <sup>3</sup>He atoms in this phase will be removed, resulting in a destruction of the equilibrium. To restore equilibrium, <sup>3</sup>He will have to flow from the concentrated phase through the phase boundary into the dilute phase. However, such a process is endothermic and removes heat from the mixing chamber environment, providing useful cooling power of the refrigerator. As <sup>3</sup>He is moving up from the mixing chamber in the dilute phase, it cools the downward flowing <sup>3</sup>He via the heat exchangers. Then, it enters the still, where <sup>3</sup>He evaporates through superfluid <sup>4</sup>He surface. Since <sup>3</sup>He has a much higher partial pressure than <sup>4</sup>He at 500–700 mK, the vapor in the still is practically pure <sup>3</sup>He. The mechanical pump at room temperature collects <sup>3</sup>He gas and creates an osmotic pressure difference, which drives more <sup>3</sup>He from the concentrated to dilute phases in the mixing chamber and then up from the mixing chamber to the still. The <sup>3</sup>He gas is further compressed by the pump and fed back into the cryostat, completing the cycle.

The appearance of dilution refrigerators differs a lot according to the designed purposes. But, their essential working principle is the same as described above. As depicted in Fig. 2.2, the top-loading dilution refrigerator (Kelvinox TLM 400) has been developed for simple and rapid sample changing for mK experiments without the need to warm up the main cryostat. A common approach (Fig. 2.5) is to have a top-loading probe which is lowered into the cryostat through a room temperature vacuum lock arrangement. The cryostat is then kept at a temperature of 4.2 K (or below) during this loading procedure, and the sample is mounted on the end of the probe. Using this technique, the sample can be loaded directly into the <sup>3</sup>He–<sup>4</sup>He mixture inside the mixing chamber. The mixing chamber tail is formed from concentric non-metallic tubes, with the outer tube forming the mixing chamber vessel. The inner tube promotes the flow of <sup>3</sup>He mixture around the sample region, eliminating temperature gradients. The refrigerator is fitted with a continuous heat exchanger and a stack of sintered-silver heat exchangers for optimum base

Fig. 2.5 A schematic of top-loading dilution refrigerator. Images are adapted from http://www.oxford-instruments.com



temperature performance. The non-metallic tail construction allows the whole mixing chamber assembly to be inserted into the bore of a high field magnet. Typically, field sweeps of up to 2 T/min leave the temperature of the mixture unaffected.

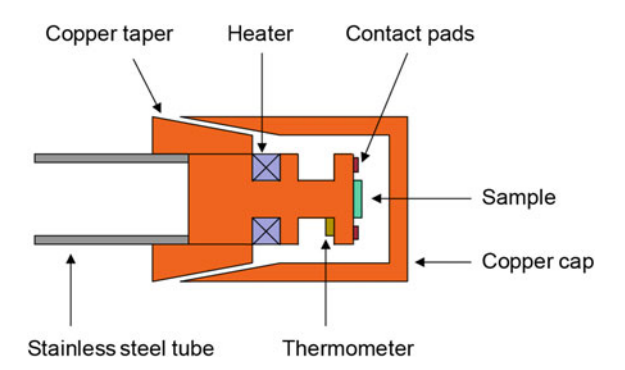
The advantages of top-loading dilution refrigerators can be described as follows. Direct submergence of the sample into the <sup>3</sup>He-<sup>4</sup>He mixture ensures good sample thermalization, high stability of the thermal environment, and guarantee of operation in high magnetic field. The sample probes can be designed into a variety of shapes for different kinds of experimental purposes, such as angle rotation or high-frequency measurements. The sample change is easy and quick, which gives quicker experiment turnaround times and reducing the risk of leaks.

#### 2.3 Probe Design and Temperature Control

In addition to commercial probes such as rotation probe for VTI and top-loading probe for dilution refrigerator, home-made probes are carefully designed and assembled to achieve high-quality measurement and versatility. As shown in Fig. 2.1, a home-made probe is inserted into the VTI with the sample space in the center of the uniform magnetic field. In this section, two home-made probes for the electrical and thermoelectric measurements will be, respectively, introduced, together with temperature control method.

In the electrical measurement probe, the sample is mounted on a copper cold finger as shown in Fig. 2.6. The sample vacuum space is achieved by a mating copper taper seal and cap, which also serves as a massive heat bath as well as the cold finger. To guarantee the sealing effect, a thin layer of Dow Corning high-vacuum grease is applied to the conical shaped surface. Furthermore, a Cernox thermometer with high sensitivity below liquid nitrogen temperature is thermally bonded on the cold finger and close to the sample. To introduce the heating power, a pair of twisted Manganin wire with resistance around 25  $\Omega$  is glued to the cold finger. The heater is further wrapped and covered by Omegabond 200 epoxy to

**Fig. 2.6** Schematic illustration of the cold end for electrical measurement probe (side view)

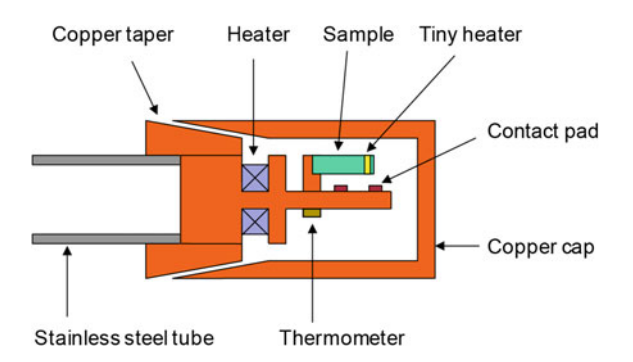


ensure good thermal conduction. A Lakeshore 340 temperature controller monitors the temperature of the heat bath through the Cernox thermometer and outputs the heating power to the Manganin heater with a built-in PID feedback controller. The cooling power is controlled by the VTI either through the one-shot mode or through the continuous-flow mode. As a result of variable cooling power, massive bath, sensitive thermometry, and carefully controlled heating power, we are able to control the temperature in the range from 1.5 to 400 K with the stability in the range of several mK.

Because of the low thermal conductivity, twisted phosphor bronze wires are used for the electrical signal conduction from the top of the probe to the cold finger. The twisted configuration is essential for canceling out electromagnetic interference from other sources, thus reducing the noise level. The terminals of these wires are soldered to the BeO contact pads on the cold finger, working as electric transition points. The sample is thermally attached on the cold finger by Omegatherm 201 compound or VGE varnish and electrically connected to contact pads by gold wires. The body of the probe is made of thin-walled 304 stainless steel tube, along which additional baffle plates are placed to reflect the thermal radiation. The top of the probe has a multipin connector, which allows connection to measurement equipment. The probe can be pumped to high vacuum with a turbomolecular pump connected to the vacuum port.

For the thermoelectric measurement probe, the design of the cold finger is slightly different. As shown in Fig. 2.7, only one end of the sample is thermally connected to the cold finger, leaving the other end attached with a tiny heater. The detailed measurement procedure will be discussed in the next section. In the thermoelectric probe, three pairs of phosphor bronze wires are replaced by pure copper wires. This is because the thermal electromotive force commonly occurs at solder points and joints between dissimilar metals, which will induce extra noise in the DC voltage measurements. Therefore, copper wires are used to connect the contact pads all the way up to the instruments, where the wire connections are made by mechanical clamping or alligator clips also made of copper. To further reduce the DC noise, all the copper wires connecting the instruments and the probe are fully shielded by aluminum foils. Generally, in order to go down to the base temperature of 1.5 K, helium gas is added to the sample space. However, this

Fig. 2.7 Schematic illustration of the cold end for thermoelectric measurement probe (side view)



would be problematic for thermal transport measurements as the helium gas presents an alternate path for heat current. Thus, the probe has to be pumped down to  $10^{-6}$  mbar with a turbomolecular pump before loading in the cryostat.

#### 2.4 Experimental Details of Transport Measurements

In this section, the electrical and thermoelectric transport measurements of TI thin films are described in details. The sample mounting, operation methods, data acquisition, and analysis will also be presented. In general, to avoid possible contamination of the TI films, an amorphous Te capping layer (10–20 nm) is deposited on top of the films before we take them out of the MBE growth chamber for transport measurements.

#### 2.4.1 Electrical Transport Measurements

The TI thin films in this thesis are grown on insulating substrates (sapphire or SrTiO<sub>3</sub>) by means of MBE. As shown in Fig. 2.8, the films are manually carved into a standard six-terminal Hall bar geometry by a sharp needle under optical microscope. Next, indium electrodes are mechanically pressed onto the sample terminals, forming a transport device for the electrical measurements. To vary the density of electrons in the films grown on SrTiO<sub>3</sub> (STO) substrates, a layer of silver paste (SPI or Dupont) is painted on the bottom of the substrates, serving as a back gate.

Before the film is mounted on the cold finger, another insulting sample holder (sapphire) is attached on the bottom of substrates. This is absolutely necessary for preventing the short between the back gate and ground. After this procedure, gold wires (California Fine Wire) are connected to the indium electrodes and contact pads to measure electric potentials  $V_{x,y}$  and inject electric current  $I_x$ . The electrical connections are guaranteed by applying a tiny amount of silver paste to the contact areas.

The electrical properties of TI thin films are measured using standard AC lock-in method with the current flowing in the film plane and the magnetic field applied perpendicularly. For the measurements at temperature >1.5 K, Stanford Research 830 lock-in amplifiers are used to monitor the AC voltages. To measure the Hall effect and magnetoresistance simultaneously, two lock-in amplifiers are connected to the sample with one triggered by the other. The AC current is generated by introducing a load resistance to the oscillator output of a lock-in amplifier. The AC current behaves like constant current source, because the load resistance ( $\sim 5 \text{ M}\Omega$ ) is much larger than the two-terminal resistance of the films (<50 K $\Omega$ ). The typical excitation current is 1 $\mu$ A, and the frequency is kept at less than 20 Hz. For the ultralow-temperature measurements, LI5640 lock-in amplifiers are used to get higher signal quality. Moreover, the load resistance is increased to about 100 M $\Omega$  in order to obtain a smaller current value (0.1 nA) and further eliminate self-heating

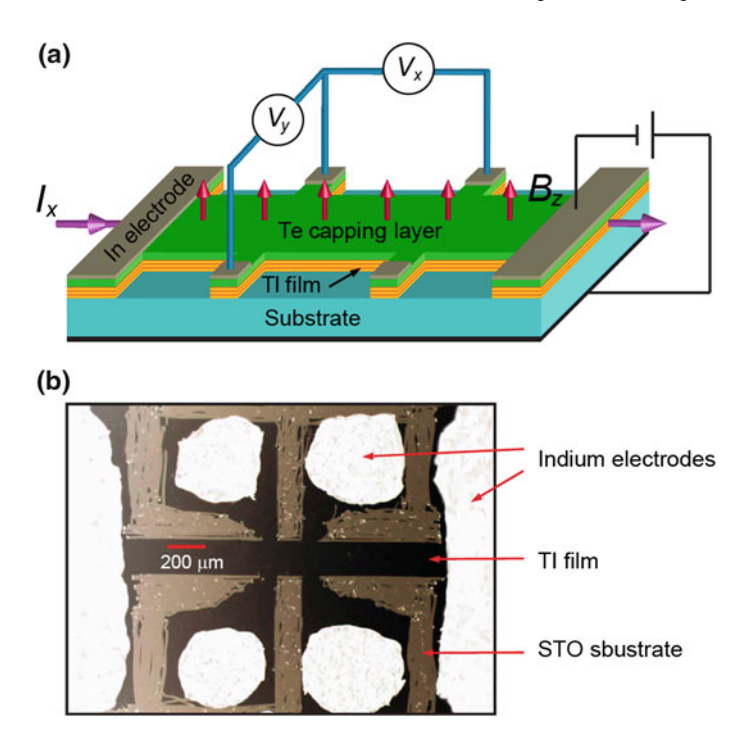


**Fig. 2.8 a** Schematic of the electrical transport measurements for TI thin film. The thickness in the figure is not to scale. **b** The photograph of the real sample prepared for transport experiments. From Ref. [4, 5], reprinted with the permission from AAAS

effect. Meanwhile, a slow field sweeping rate of 0.025 T/min is used during the low-field measurements so as to reduce the heating effect from eddy current. Because the sample resistance is greatly increased at such a low temperature, the measuring frequency has to be lowered to about 5 Hz to remove the capacitance coupling. Another alternative way for the electrical measurements is to interface Keithley 6221 current source with Keithley 2182A nanovoltmeter by averaging the positive and negative DC excitations (Delta mode). Both methods described above can eliminate the effects of thermal drift and DC offsets, producing highly accurate transport measurements.

The data acquisition is realized by LabVIEW software installed in the computer. The signal communication is accomplished by a GPIB data acquisition card assembled in the computer and GPIB cables connected on the instruments. GPIB is a specification for short-range digital communications bus. Because of its simple hardware interface and easy connection of multiple devices to a single host, it is widely used for data transfer in modern laboratory electronics.

In the electrical transport measurements using the Hall bar geometry, the unavoidable misalignment of the Hall contacts always leads to the pickup of the longitudinal signal and vice versa. A standard practice to remove this artifact is to use the signal that is antisymmetric (for  $\rho_{yx}$ ) and symmetric (for  $\rho_{xx}$ ) to the magnetic

field. For the non-magnetic samples, the Hall resistivity  $\rho_{yx}$  and longitudinal resistivity  $\rho_{xx}$  can be obtained through the following expressions:

$$\rho_{yx}(H) = \left[\tilde{\rho}_{yx}(H) - \tilde{\rho}_{yx}(-H)\right]/2, 
\rho_{xx}(H) = \left[\tilde{\rho}_{xx}(H) + \tilde{\rho}_{xx}(-H)\right]/2.$$
(2.1)

Here,  $\tilde{\rho}$  represents the as-measured raw data after considering the geometric effect. In magnetic samples, because of the existence of hysteresis, the magnetic fields have to be swept in both directions (upward/downward). Therefore,

$$\rho_{yx}(H, \text{up}) = \left[\tilde{\rho}_{yx}(H, \text{up}) - \tilde{\rho}_{yx}(-H, \text{down})\right]/2, 
\rho_{xx}(H, \text{up}) = \left[\tilde{\rho}_{xx}(H, \text{up}) + \tilde{\rho}_{xx}(-H, \text{down})\right]/2,$$
(2.2)

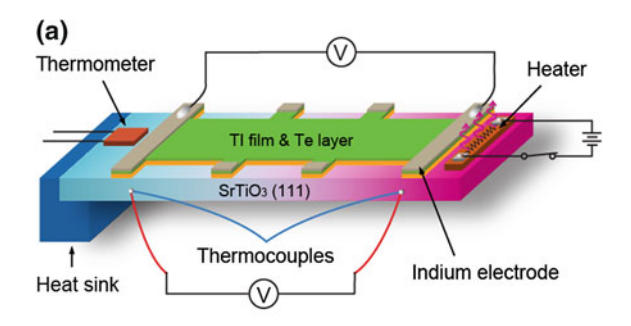
where up(down) stands for the field sweeping direction from negative (positive) to positive (negative). Then,  $\rho_{yx}(H, \text{down}) = -\rho_{yx}(-H, \text{up})$ ,  $\rho_{xx}(H, \text{down}) = \rho_{xx}(-H, \text{up})$ . All the  $\rho_{yx}$  and  $\rho_{xx}$  data presented in the thesis are antisymmetrized and symmetrized by performing the above procedures.

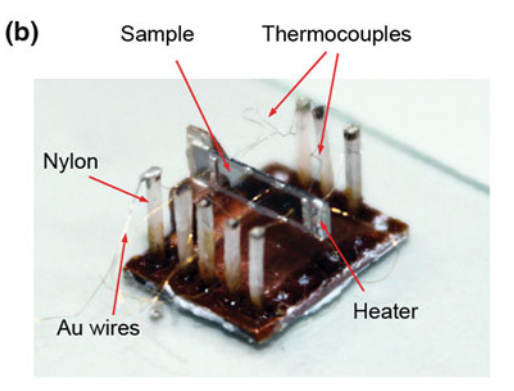
#### 2.4.2 Thermoelectric Transport Measurements

The thermoelectric measurements are carried out on TI films grown on STO substrates, which have much lower thermal conductivity than sapphire. The schematic setup and real device are shown in Fig. 2.9 with a typical sample size of 2 mm  $\times$  8 mm. One end of the sample is glued with silver paste onto a copper heat sink, which is thermally attached on the cold finger using Omegatherm 201 compound. Considering the measurement efficiency, we reuse the heat sink for different samples, which is the reason why we choose silver paste rather than silver epoxy. In order to monitor the temperature accurately, a miniature Cernox thermometer (bare chip) is mounted on the bottom end of the sample. On the other end, two thin-film heaters are attached to generate the necessary temperature gradient. The resistance of each heater is around 1 k $\Omega$ , and it remains constant in a board range of temperature. By applying a DC current (Keithley 2400 source meter) in the range of 0.5–1 mA to the heaters, a sizable temperature gradient (0.1–0.2 K/mm) is obtained along the sample.

The temperature difference between current electrodes is detected by a pair of fine gauge type E thermocouples (Chromega–Constantan) which have high sensitivity in the temperature range between 4.2 and 300 K. The joints of the thermocouples are placed at the edge or backside of the substrate aligned with the current electrodes. Furthermore, a tiny amount of thermal joint compound (Omegatherm 201) is applied to the joints to guarantee good thermal contacts. The negative legs of the two thermocouples are electrically connected, and the positive legs are connected to the copper wires in the probe. Fine gold wires (0.001 in.) are used as electric leads that contact the current electrodes and copper wires on the cold finger. For the other electric leads, it is better to use fine phosphor bronze wires (0.001 in.)

Fig. 2.9 a Schematic device for thermoelectric transport measurements of TI thin film. The thickness in the figure is not to scale. b The real sample structure prepared for thermoelectric experiments. Reprinted with the permission from Ref. [6]. Copyright 2015 by American Physical Society





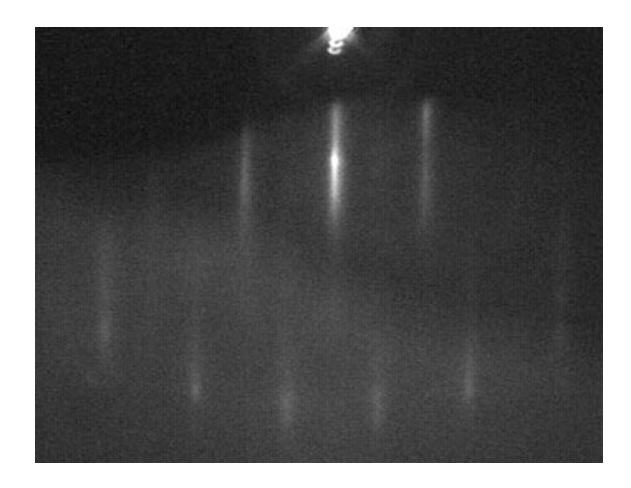
to reduce the unintentional heat flow along the wires. To maintain the stability during measurements, every wire connected to the sample is supported by thin nylon pillar. The principle behind this design is to force the heat generated by Joule heating to flow down the sample to the heat sink.

The DC voltages produced by the thermoelectric effect are measured by Keithley 2002 digital multimeters with Keithley 1801 preamplifiers. Effect of DC drift is minimized by using all copper wires and copper clamp connections with solder-free joints, which is particularly important for DC measurements at low temperatures. With these precautions, a DC noise level of 10 nV can be achieved. By alternately switching the tiny heater on and off, the Seebeck coefficient can be obtained as  $S_{xx} = (V_{S,on} - V_{S,off})/(V_{TC,on} - V_{TC,off}) \times S_{TC} + S_{Au}$ . Here,  $V_S$  and  $V_{TC}$  are the DC voltages on the sample and thermocouples recorded by the multimeters, and  $S_{TC}$  and  $S_{Au}$  are the Seebeck coefficients of the thermocouples and gold wire.

#### 2.5 Sample Growth by Molecular Beam Epitaxy

Molecular beam epitaxy (MBE) is an advanced sample growth method capable of depositing very thin films with near-perfect surface morphology and near-perfect control of layer thicknesses, compositions, and doping levels. In this thesis, the TI

Fig. 2.10 The  $1 \times 1$  RHEED (reflection high-energy electron diffraction) pattern measured in situ on the 5 QL (Bi<sub>0.12</sub>Sb<sub>0.88</sub>)<sub>2</sub>Te<sub>3</sub> film grown by MBE. The sharpness of the pattern indicates the high quality of the sample



thin films including  $(Bi_{1-x}Sb_x)_2Te_3$  ternary alloys, Cr-doped  $Bi_2(Se_xTe_{1-x})_3$ , and Cr-doped  $(Bi_{1-x}Sb_x)_2Te_3$  compounds are grown by our collaborative group in State Key Laboratory for Surface Physics in the Institute of Physics, Chinese Academy of Science.

The MBE growth is carried out in an ultrahigh vacuum (UHV) MBE-ARPES-STM combined system (Omicron) with the base pressure  $\sim 8 \times 10^{-11}$  mbar. High-purity Bi, Sb, Cr, Te, and Se are evaporated from standard Knudsen cells. Prior to sample growth, the substrate [sapphire (0001) or SrTiO<sub>3</sub> (111)] should be degassed to remove the contaminants on the surface. In order to reduce Te/Se vacancies, the growth is kept in Te/Se-rich condition. The substrate is held at around 180 °C during the growth. As shown in Fig. 2.10, a real-time RHEED (reflection high-energy electron diffraction) intensity oscillation measured on the (00) diffraction is used to calibrate the growth rate, which is controlled at a typical value of  $\sim 0.125$  QL/min.

The flux of Bi or Sb at a given source temperature can be accurately calibrated by the growth rate of pure  $Bi_2Te_3$  or  $Sb_2Te_3$  films measured by RHEED oscillation and quantum well states revealed by ARPES [7–9]. The flux of Cr is calibrated by the concentration in Cr-doped TI films. The thicknesses of the films are determined by growth time and the flux of Cr, Bi, and Sb sources and further checked by atomic force microscope (AFM).

The chemical compositions of TI films are determined through two independent methods. The first method is to calculate it through the flux ratio (Bi/Sb or Te/Se) during the sample growth. For example, in the MBE-grown (Bi<sub>1-x</sub>Sb<sub>x</sub>)<sub>2</sub>Te<sub>3</sub> films, x can be determined by the calibrated flux ratio between Bi and Sb. To vary the x value in the (Bi<sub>1-x</sub>Sb<sub>x</sub>)<sub>2</sub>Te<sub>3</sub> films, we control the source temperatures of Bi and Sb. Recall that in MBE growth, the flux (J) and the source temperature (T) are related by  $T \propto P/\sqrt{T}$ , where T is the vapor pressure at the source temperature T [10]. By choosing different source temperatures of Bi and Sb, hence the flux ratio between them, we can systematically tune the T value of the film.

In the second method, the compositions of the TI films are directly measured by inductively coupled plasma atomic emission spectroscopy (ICP-AES). For ICP-AES measurements, thicker films (above 50 nm) are needed to give sufficient accuracy. Growth of such thick films is rather time-consuming with the current growth rate of our MBE system. Therefore, we did not perform the ICP-AES measurement on every sample. The difference between the x value determined by ICP-AES and that estimated from the flux ratio is around 5 % in two typical  $(\text{Bi}_{1-x}\text{Sb}_x)_2\text{Te}_3$  samples. The reasonably good agreement indicates that the x value estimated from the Bi/Sb flux ratio is quite reliable. However, in the Cr-doped  $\text{Bi}_2(\text{Se}_x\text{Te}_{1-x})_3$  films, the estimation of x value from flux ratio of Te/Se may have a relatively large error compared to the ICP-AES method because of the presence of Te-rich condition. This problem can be alleviated by setting the crucial sample as a reference whose x value has been carefully measured by ICP-AES. The x values of other samples are calibrated relative to the flux ratio of the reference sample.

#### 2.6 Angle-Resolved Photoemission Spectroscopy

The angle-resolved photoemission spectroscopy (ARPES) uses a photon to eject an electron from a sample and then determines the surface or bulk electronic structure from an analysis of the momentum and energy of the emitted electrons. ARPES measurements in this thesis are carried out in situ at room temperature or 120 K by using a Scienta SES 2002 electron energy analyzer. A helium discharge lamp with a photon energy of hv = 21.218 eV is used as the photon source. The energy resolution of the electron energy analyzer is set at 15 meV. All the spectra are taken along the K- $\Gamma$ -K direction. To avoid sample charging during ARPES measurements due to the insulating sapphire substrate, a 300-nm-thick titanium (Ti) film is deposited at both ends of the substrate which is connected to the sample holder. The sample is grounded through these contacts once a continuous film is formed. The sample setup for the ARPES measurements is illustrated schematically in Fig. 2.11.

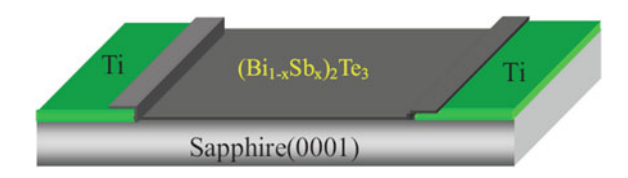


**Fig. 2.11** Sketch of the sample setup for in situ ARPES measurement. To avoid sample charging during ARPES measurements due to the insulating sapphire substrate, a 300-nm-thick titanium (Ti) film is deposited at both ends of the substrate which is connected to the sample holder. The sample is grounded through these contacts once a continuous film is formed

References 37

#### References

 Lounasmaa OV. Experimental principles and methods below 1 K. London: London Academic; 1974.

- 2. Pobell F. Matter and methods at low temperatures. Berlin: Springer; 2007.
- 3. Zhang Y, He K, Chang C-Z, et al. Crossover of the three-dimensional topological insulator Bi<sub>2</sub>Se<sub>3</sub> to the two-dimensional limit. Nat Phys. 2010;6:584–8.
- 4. Li Y-Y, Wang G, Zhu X-G, et al. intrinsic topological insulator Bi<sub>2</sub>Te<sub>3</sub> thin films on Si and their thickness limit. Adv Mater. 2010;22:4002–7.
- Wang G, Zhu X, Wen J, et al. Atomically smooth ultrathin films of topological insulator Sb<sub>2</sub>Te<sub>3</sub>. Nano Res. 2010;3:874–80.
- 6. Reif F. Fundamentals of statistical and thermal physics. New York: McGraw-Hill; 1965.
- 7. de Waele A. Introduction to dilution refrigeration. 2009.
- 8. Zhang J, Chang C-Z, Tang P, et al. Topology-driven magnetic quantum phase transition in topological insulators. Science. 2013;339:1582–6.
- 9. Chang C-Z, Zhang J, Feng X, et al. Experimental observation of the quantum anomalous hall effect in a magnetic topological insulator. Science. 2013;340:167–70.
- 10. Zhang J, Feng X, Xu Y, et al. Disentangling the magnetoelectric and thermoelectric transport in topological insulator thin films. Phys Rev B. 2015;91:075431.

# **Chapter 3 Band Structure Engineering in TIs**

The most challenging problem the current TI materials facing is the existence of significant bulk conduction. In this chapter, we show the band structure engineering in TIs by fabricating  $(Bi_{1-x}Sb_x)_2Te_3$  ternary compounds using MBE method. Transport and ARPES measurements show that the topological surface states exist over the entire composition range of  $(Bi_{1-x}Sb_x)_2Te_3$ , indicating the robustness of bulk  $Z_2$  topology. Most remarkably, the band engineering leads to ideal TIs with truly insulating bulk and tunable surface states across the Dirac point (DP) that behave like one quarter of graphene. These results demonstrate a new route to achieving intrinsic quantum transport of the topological surface states and designing conceptually new TI devices with well-established semiconductor technology. The main conclusions in this chapter are published in Ref. [1] with the reuse permission of full article from Macmillan Publishers Ltd., copyright 2011.

### 3.1 Band Structure Engineering in Traditional Semiconductors

Band structure engineering is a powerful technique for controlling or altering the band structure of a material by controlling the composition of certain semiconductor alloys. It is also possible to construct layered materials (superlattice or heterostructure) with alternating compositions by the MBE technique. In this approach, the transport and optical properties of these artificially structured semiconductors can be changed or tailored at will. This method is widely exploited in the design of new-generation devices with unique capabilities, such as high-electron-mobility transistor, laser diodes, and solar cells.

Figure 3.1 shows the band gaps of various binary semiconductors and their alloys as a function of lattice constant. For direct gap semiconductors, the size of the band gap is crucial in the optoelectronic applications. However, for most of the

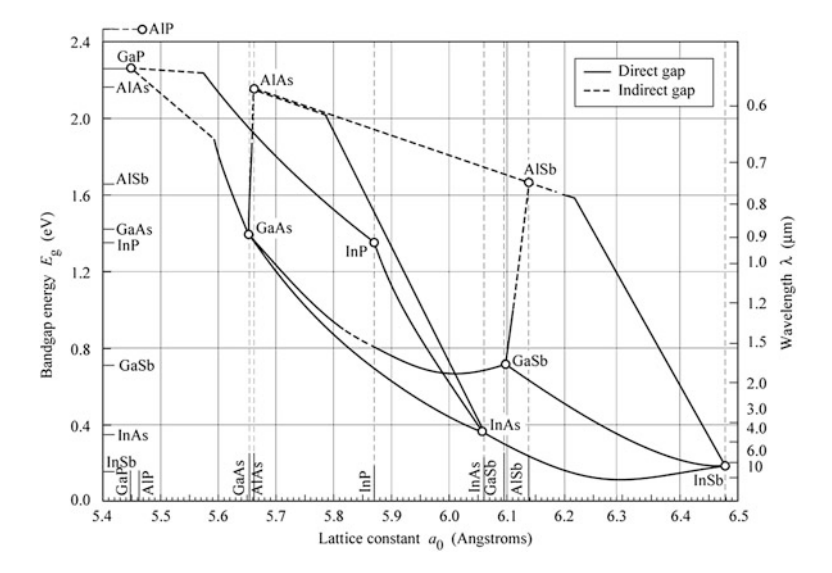
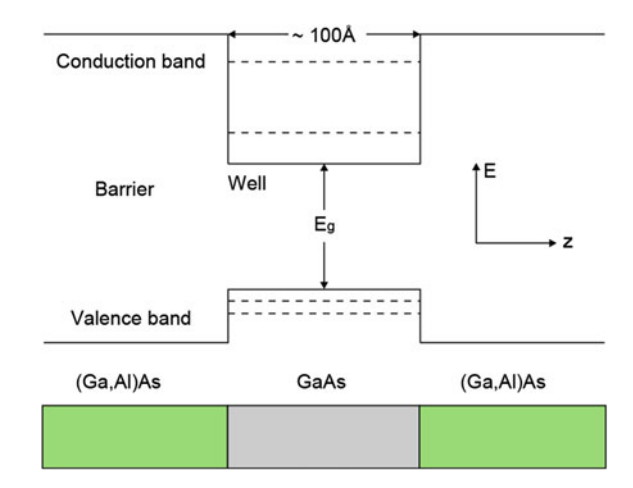


**Fig. 3.1** Band gap versus lattice parameter for common semiconductors. The *solid curves* (direct gaps) and *dashed* (indirect gaps) *curves* represent the commonly used alloys such as (Ga,Al)As, (Ga,In)As. Reprinted from Ref. [2] with the permission from Cambridge University Press

binary semiconductors, the band gaps are not optimized for particular applications. Therefore, the band structure engineering method is generally used to fabricate a variety of alloying compounds with desired band gap structure. A notable example is the isostructural isovalent alloy of the III–V semiconductors  $Al_xGa_{1-x}As$ , where a solid solution over the entire composition range  $(0 \le x \le 1)$  can be formed with very little variation of lattice mismatch, enabling the fabrication of high-quality multilayer structures.

Another important application of band structure engineering is the fabrication of artificial heterostructures, which involves the quantum wells, superlattice, and heterojunctions. For the quantum wells, the simplest structure is composed of a thin layer of a narrower gap material (such as GaAs) sandwiched by two thick layers of wider gap materials (such as  $Al_xGa_{1-x}As$ ). As shown in Fig. 3.2, due to the confinement of the electrons and holes in z direction, bond states (sub-bands) are formed in the narrower gap material with discontinuous energy levels. However, in the x-y plane, the motion is unrestricted, resulting in a 2D electron system in the quantum well. For the optical properties of quantum wells, the interband optical absorption or emission will be caused by creation and recombination of electronhole pairs in the sub-bands. Most remarkably, the energy levels of the sub-bands can be varied by changing the well width, which allows the energy of the fundamental optical transition to be continuously adjustable. Furthermore, the transitions in quantum wells are excitonic, which have sharp features at well-defined energies even at room temperatures. More than that, the excited electrons and holes are kept in close proximity, which can improve the recombination efficiency. All the above

**Fig. 3.2** The diagram of a (Ga,Al)As quantum well. The energies of the sub-band edges within the well are shown schematically



features make quantum wells one of the best candidates in optoelectronic applications.

In addition, the modulation-doped heterojunction is of great importance both in synthesizing high-mobility transistors and in scientific researches. A heterojunction is the interface that occurs between two layers of dissimilar crystalline semiconductors with unequal band gaps. A typical example is the GaAs–(Ga,Al)As heterojunction, where a layer of 2D electron gas system is formed in the interface potential well. Since the ionized donors in (Ga,Al)As layers are separated from the electron gas, the scattering rate is dramatically reduced, resulting in a greatly enhanced electron mobility ( $\sim 10^7 \text{ cm}^2 \text{V}^{-1} \text{s}^{-1}$ ). At ultralow temperature and high magnetic field, such high-mobility electrons exhibit a new quantum state, the fractional quantum Hall effect [3].

#### 3.2 Motivation and Experimental Design

The experimental realization of the proposed exotic topological quantum effects [4–6] and device applications requires fabrication of versatile devices based on bulk-insulating TIs with tunable surface states. However, the currently available TI materials exemplified by Bi<sub>2</sub>Se<sub>3</sub> and Bi<sub>2</sub>Te<sub>3</sub> [7] always show conductive bulk states due to the defect-induced charge carriers. Tuning the band structure of the TIs to eliminate the bulk states is one of the most urgent tasks in the field, but the problem remains unsolved despite extensive efforts involving nanostructuring [8], chemical doping [9–14], and electric gating [15–18].

Inspired by the idea of energy band engineering [19], we conceive a new route for engineering the band structure of TIs by fabricating alloys of Bi<sub>2</sub>Te<sub>3</sub> and

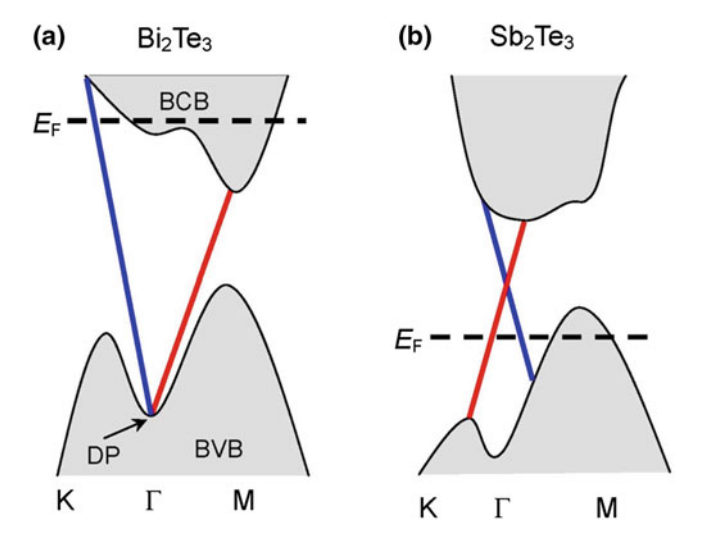


Fig. 3.3 The schematic electronic band structure of pure  $Bi_2Te_3$  (a) and pure  $Sb_2Te_3$  (b) based on theoretical calculations [7] and ARPES experiments [9, 20]

Sb<sub>2</sub>Te<sub>3</sub>. Both TIs are V–VI compounds with the same crystal structure and close lattice constants [7], making it ideal to form  $(Bi_{1-x}Sb_x)_2Te_3$  ternary compounds with arbitrary mixing ratio and negligible strain (Fig. 1.2). The potential advantages of mixing the two TIs can be anticipated from their complementary electronic properties. Figure 3.3a illustrates the band structure of pure  $Bi_2Te_3$  [7, 9, 20], which reveals two major drawbacks of the surface Dirac band. First, the DP is buried in the bulk valence band (BVB), hence cannot be accessed by transport experiment and, more seriously, the Fermi level ( $E_F$ ) lies in the bulk conduction band (BCB) due to the electron-type bulk carriers induced by Te vacancies. The band structure of pure  $Sb_2Te_3$  [7, 20], on the other hand, is drastically different. As shown schematically in Fig. 3.3b, here the DP lies within the bulk gap and the Fermi level ( $E_F$ ) lies in the BVB due to the hole-type bulk carriers induced by Sb–Te antisite defects. Intuitively, by mixing the two compounds one can simultaneously achieve charge compensation and tune the position of the DP, which may lead eventually to an ideal TI with exposed DP and insulating bulk.

#### 3.3 Experimental Results

This section reports the experimental results of 5 QL  $(Bi_{1-x}Sb_x)_2Te_3$  ternary alloys, which involves the sample characterization, electron band structure, and transport properties.

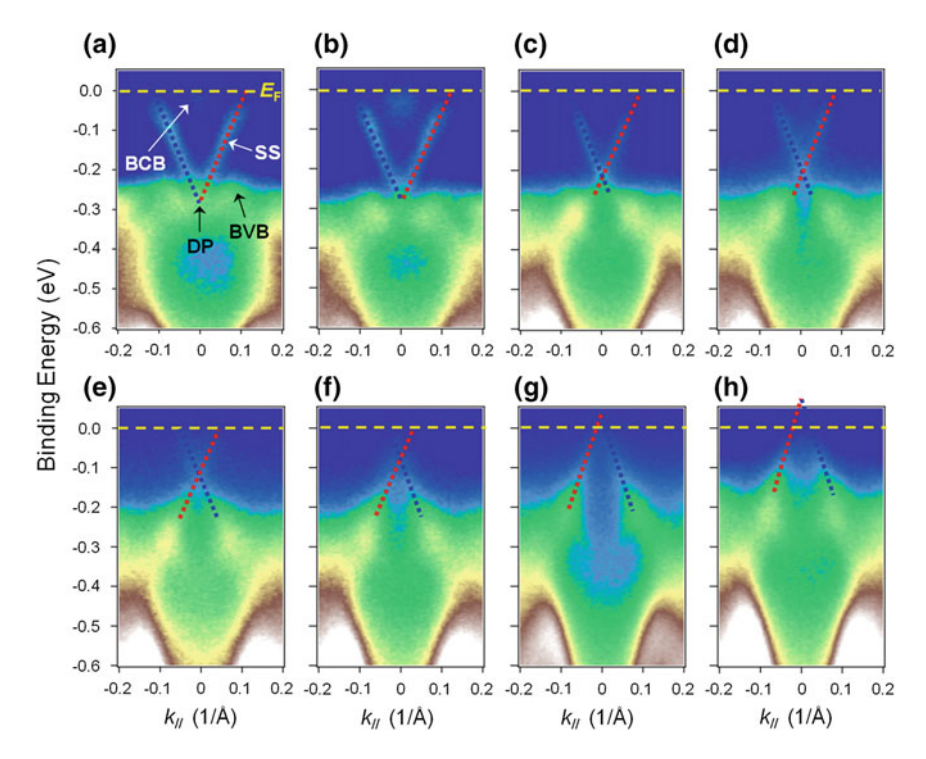
#### 3.3.1 Sample Characterization

Figure 2.10 shows a typical  $1 \times 1$  RHEED pattern taken on a  $(Bi_{1-x}Sb_x)_2Te_3$  film with five quintuple-layer (QL) thickness. The sharpness of the feature provides a clear evidence for the high quality of the sample.

All the data shown in the main text were taken on  $(Bi_{1-x}Sb_x)_2Te_3$  films with thickness d = 5 QL. There are two main considerations for choosing this particular film thickness. The first requirement is that the TI film must be thick enough so that there is no coupling between the top and bottom surfaces. For the  $(Bi_{1-x}Sb_x)_2Te_3$ compounds, the coupling between the two surfaces vanishes for  $d \ge 4$  QL. The 5 QL films used here have completely decoupled surface states, as seen by the absence of energy gap at the DP measured by ARPES. Our collaborators also performed scanning tunneling spectroscopy, which have much better energy resolution than ARPES, on similar films and confirmed this conclusion [21]. The second requirement concerning the film thickness is that it should be thin enough so that the bulk conduction can be safely ignored. Although we can tune the Fermi level into the bulk energy gap by using the band engineering technique, there is always unavoidable bulk conduction via variable range hopping through the defects. With increasing film thickness, this contribution becomes more pronounced. Bi<sub>2</sub>Te<sub>2</sub>Se TI single crystal is taken as an example. Even though the Fermi level lies in the bulk energy gap and the bulk defect density is very low, the bulk states still account for  $\sim 94$  % of the total conduction [22]. A major advantage of the MBE technique is that we can grow ultrathin films of TIs with large surface to volume ratio. In the 5 QL films, the bulk conduction is negligible so that the transport is dominated by surface states. Therefore, the 5 QL thickness is chosen because it is the optimal thickness where the coupling of the surfaces vanishes and the bulk conduction can be safely ignored. The ability to reach the ultrathin regime of TIs in a controlled manner is actually an important advantage of the MBE growth technique.

#### 3.3.2 Electronic Structure

The electronic structures of the  $(Bi_{1-x}Sb_x)_2Te_3$  films are measured by ARPES on a sample setup as illustrated in Fig. 2.11. The ARPES band maps of eight  $(Bi_1-xSb_x)_2Te_3$  films with  $0 \le x \le 1$  are shown in Fig. 3.4a–h. The pure  $Bi_2Te_3$  film shows well-defined surface states with massless Dirac-like dispersion (Fig. 3.4a), similar to that of the cleaved  $Bi_2Te_3$  crystal [9]. With the addition of Sb, the Dirac-like topological surface states can be clearly observed in all  $(Bi_{1-x}Sb_x)_2Te_3$  films from x = 0 to 1, while the Dirac cone geometry changes systematically. With increasing x, the slope of the Dirac line shape becomes steeper, indicating an increase of the Dirac fermion velocity  $v_D$  defined by the linear dispersion  $\varepsilon = v_D \cdot \hbar k$  near the DP. Meanwhile, the  $E_F$  moves downward from the BCB, indicating the reduction of the electron-type bulk carriers. Moreover, the DP moves upward



**Fig. 3.4** ARPES results on the 5 QL  $(\mathrm{Bi_{1-x}Sb_x})_2\mathrm{Te_3}$  films measured along the K- $\Gamma$ -K direction. From **a** to **h**, the panels correspond to samples with x=0,0.25,0.62,0.75,0.88,0.94,0.96, and 1.0, respectively. The Dirac-like topological surface states exist in all films. The *yellow dashed line* indicates the position of the Fermi level. The *blue* and *red dashed lines* indicate the Dirac surface states with opposite spin polarities and they intersect at the Dirac point

relative to the BVB due to the increasing weight of the  $\mathrm{Sb_2Te_3}$  band structure. When the Sb content is increased to x=0.88 (Fig. 3.4e), both the DP and the  $E_\mathrm{F}$  lie within the bulk energy gap. The system is now an ideal TI with a truly insulating bulk and a nearly symmetric surface Dirac cone with exposed DP. Notably, when x increases from x=0.94 (Fig. 3.4f) to 0.96 (Fig. 3.4g),  $E_\mathrm{F}$  moves from above the DP to below it, indicating a crossover from electron- to hole-type Dirac fermion gas. The charge neutrality point (CNP) where  $E_\mathrm{F}$  meets DP can thus be identified to be located between x=0.94 and 0.96.

It is quite remarkable that the topological surface states exist in the entire composition range of  $(Bi_{1-x}Sb_x)_2Te_3$ , which implies that the non-trivial  $Z_2$  topology of the bulk band is very robust against alloying. This is in contrast to the  $Bi_{1-x}Sb_x$  alloy, the first discovered 3D TI in which the topological surface states only exist within a narrow composition range near x = 0.10 [23, 24]. Figure 3.5a–c summarizes the characteristics of the surface Dirac band in the  $(Bi_{1-x}Sb_x)_2Te_3$  compounds, which are extracted following the methodology illustrated in the next section. The position of the DP rises continuously from below the top of BVB near the  $\Gamma$  point at

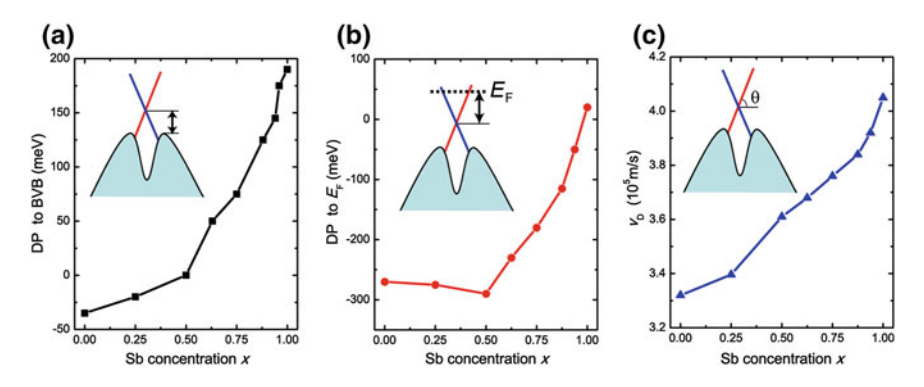


**Fig. 3.5** Evolution of the Dirac-like surface band characteristics with *x* obtained from the ARPES data in the  $(Bi_{1-x}Sb_x)_2Te_3$  films. **a** Relative position (or energy difference) between the DP and the top of BVB near the Γ point. **b** Relative position between the DP and the  $E_F$ . **c** The Dirac fermion velocity  $v_D$  ( $v_D \sim \tan\theta$ ) extracted from the linear dispersion near the DP. All three quantities evolve smoothly from that of pure  $Bi_2Te_3$  (x = 0) to pure  $Sb_2Te_3$  (x = 1)

x = 0 to way above that at x = 1 (Fig. 3.5a). This is accompanied by a drastic change of the relative position of  $E_{\rm F}$  and DP (Fig. 3.5b), which determines the type and density of Dirac fermions. Furthermore,  $v_{\rm D}$  increases from  $3.3 \times 10^5$  m/s at x = 0 to  $4.1 \times 10^5$  m/s at x = 1 (Fig. 3.5c). Since the three defining properties of the Dirac cone are systematically varied between that of pure Bi<sub>2</sub>Te<sub>3</sub> and Sb<sub>2</sub>Te<sub>3</sub>, the (Bi<sub>1-x</sub>Sb<sub>x</sub>)<sub>2</sub>Te<sub>3</sub> ternary compounds are effectively a series of new TIs. The bulk electronic structures, including the geometry of BCB and BVB as well as the energy gap between them, are also expected to change with x. They are of interests in their own rights, but will not be the main focus of the current work.

#### 3.3.3 Analysis of the ARPES Data

In Fig. 3.5, we show the x dependence of the relevant parameters of the surface band structure measured by ARPES. Here, we use the spectrum of the x = 0.88 film as an example to demonstrate the ARPES data analysis procedure.

In order to enhance the visibility of the band structure, the second-order differential ARPES spectrum of the 5 QL  $(Bi_{0.12}Sb_{0.88})_2Te_3$  film is shown in Fig. 3.6a. The surface states with Dirac-like dispersion can be seen clearly and are marked by the dashed lines (the red and blue colors indicate the different spin polarization). The point where the two dashed lines meet is defined as the DP. The energy difference between the DP and  $E_F$  (yellow dashed line at zero binding energy) is the quantity plotted in Fig. 3.5b.

Figure 3.6b shows the corresponding momentum distribution curves (MDC). The peak positions of the Dirac surface states are obtained by fitting the MDCs with Lorentz functions. The velocity of the Dirac fermions,  $v_D = 3.8 \times 10^5$  m/s, is then derived from the linear *E* versus *k* dispersion near the DP. The Fermi wave vector  $k_F$ 

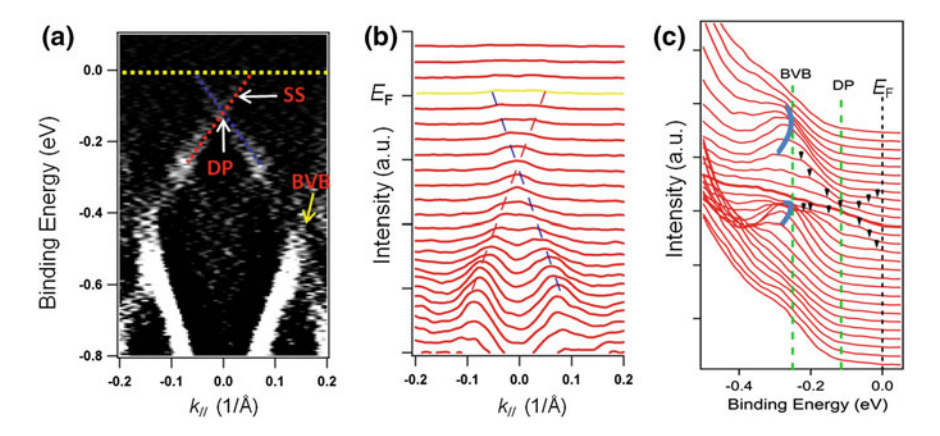


**Fig. 3.6** Analysis of the ARPES results. **a** Second-order differential ARPES spectrum of the 5 QL  $(Bi_{0.12}Sb_{0.88})_2Te_3$  film along the K- $\Gamma$ -K direction. The surface states (SS), Dirac point (DP), and bulk valence band (BVB) are marked. **b** The momentum distribution curve (MDC) measured on the same sample. The  $E_F$  is indicated by *solid yellow line*. **c** The energy distribution curve (EDC) of the same sample. The BVB, the DP, and the  $E_F$  are marked, respectively

of the surface states can be read from the k value of the crossing point between the surface states and the  $E_{\rm F}$  (yellow line) and is found to be  $k_{\rm F}=0.057~{\rm \AA}^{-1}$  for the x=0.88 sample. The  $v_{\rm D}$  and  $k_{\rm F}$  values are plotted in Fig. 3.5c and 3.9b (in the next section).

Figure 3.6c shows the energy distribution curves (EDC) of the 5 QL  $(Bi_{0.12}Sb_{0.88})_2Te_3$  film. The peaks indicated with black arrows are the Dirac surface states. The prominent and broad features at around  $E_B = -245$  meV (indicated with thick blue lines) result from the hybridization between surface states and bulk band [20, 25]. So the features can be regarded as the top of BVB near  $\Gamma$  point. In this sample, the positions of DP and the top of BVB near  $\Gamma$  point are about -115 and -245 meV, respectively. So the distance from DP to BVB is 130 meV, as plotted in Fig. 3.5a.

#### 3.3.4 Transport Properties

The systematic Dirac band evolution also manifests itself in the transport properties. Figure 3.7 displays the variation of two-dimensional (2D) sheet resistance ( $R_{\square}$ ) with temperature (T) for eight 5 QL ( $Bi_{1-x}Sb_x$ )<sub>2</sub> $Te_3$  films with  $0 \le x \le 1$ . In pure  $Bi_2Te_3$ , the resistance shows metallic behavior at high T and becomes weakly insulating at very low T. With increasing x, the  $R_{\square}$  value keeps rising and the insulating tendency becomes stronger, reflecting the depletion of electron-type bulk carriers and surface Dirac fermions. At x = 0.94, when  $E_F$  lies just above DP, the resistance reaches the maximum value and shows insulating behavior over the whole T range. With the further increase of Sb content from x = 0.96 to 1, the resistance decreases

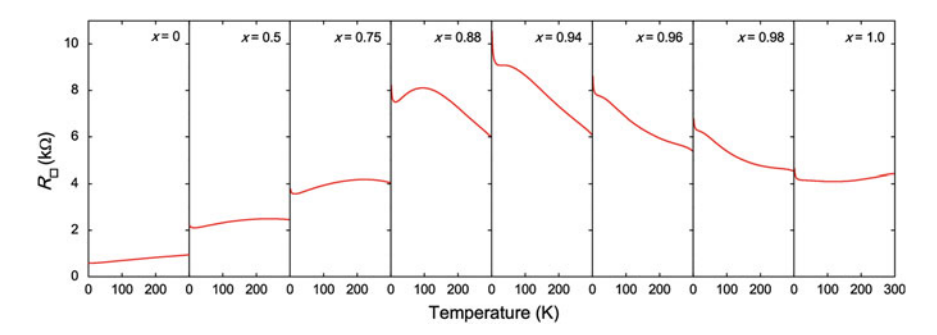


**Fig. 3.7** Two-dimensional (2D) sheet resistance  $(R_{\square})$  versus temperature (T) for eight 5 QL  $(\text{Bi}_{1-x}\text{Sb}_x)_2\text{Te}_3$  films.  $R_{\square}$  value keeps rising and the insulating tendency becomes stronger with increasing Sb content from x=0 to 0.94 due to the reduction of electron-type carriers. From x=0.96 to 1, the trend is reversed, i.e.,  $R_{\square}$  value decreases and the insulating tendency becomes weaker with increasing Sb content due to the increasing density of hole-type carriers

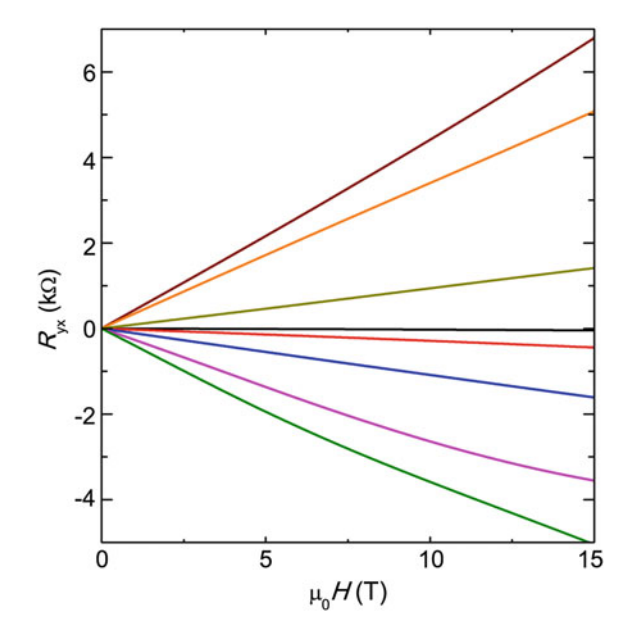
systematically because now  $E_{\rm F}$  passes DP and more hole-type carriers start to populate the surface Dirac band. The high T metallic behavior is recovered in pure  ${\rm Sb_2Te_3}$  when the hole-type carrier density becomes sufficiently high.

Figure 3.8 displays the variation of the Hall resistance  $(R_{yx})$  with magnetic field (H) measured on the 5 QL  $(Bi_{1-x}Sb_x)_2Te_3$  films at T=1.5 K. For films with  $x \le 0.94$ , the  $R_{yx}$  value is always negative, indicating the existence of electron-type carriers. The weak-field slope of the Hall curves, or the Hall coefficient  $R_H$ , increases systematically with x in this regime. Since the 2D carrier density  $n_{2D}$  can be derived from  $R_H$  as  $n_{2D} = 1/eR_H$  (e is the elementary charge), this trend confirms the decrease of electron-type carrier density with Sb doping. As x increases slightly from 0.94 to 0.96, the Hall curve suddenly jumps to the positive side with a very large slope, which indicates the reversal to hole-type Dirac fermions with a small carrier density. At even higher x, the slope of the positive curves decreases systematically due to the increase of hole-type carrier density.

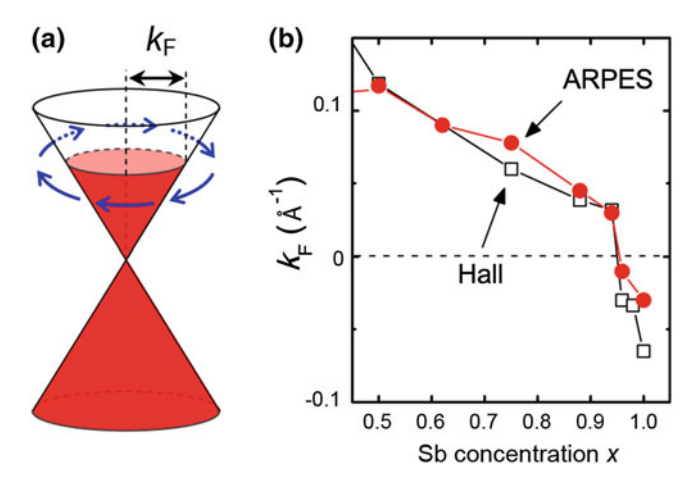
The evolution of the Hall effect is totally consistent with the surface band structure revealed by ARPES in Fig. 3.4. To make a more quantitative comparison between the two experiments, we use the  $n_{\rm 2D}$  derived from the Hall effect to estimate the Fermi wave vector  $k_{\rm F}$  of the surface Dirac band. By assuming zero bulk contribution and an isotropic circular Dirac cone structure (Fig. 3.9a),  $k_{\rm F}$  can be expressed as follows:

$$\frac{D \cdot k_F^2}{4\pi} = |n_{SS}|,\tag{3.1}$$

Here, D is the degeneracy of the Dirac fermion and  $|n_{SS}| = 1/2|n_{2D}|$  is the carrier density per surface if we assume that the top and bottom surfaces are equivalent. Figure 3.9b shows that when we choose D = 1, the  $k_F$  values derived from the Hall effect match very well with that directly measured by ARPES. This

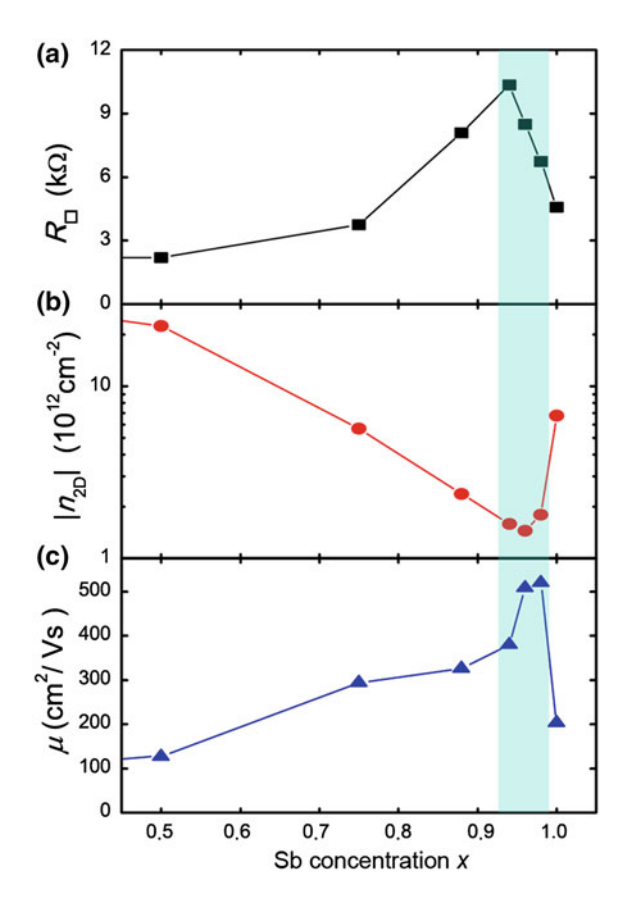


**Fig. 3.8** The field dependence of the Hall resistance  $R_{yx}$  for the eight  $(Bi_{1-x}Sb_x)_2Te_3$  films measured at T = 1.5 K. From *top* to *bottom*, the curves correspond to x = 0.96, 0.98, 1.0, 0, 0.50, 0.75, 0.88, and 0.94, respectively. The evolution of the Hall effect reveals the depletion of electron-type carriers (from x = 0 to 0.94), the reversal of carrier type (from x = 0.94 to 0.96), and the increase of hole-type carrier density (from x = 0.96 to 1.0)



**Fig. 3.9** a Schematic sketch of an isotropic circular Dirac cone where the Fermi wave vector  $k_{\rm F}$  is marked. The *blue arrows* indicate the helical spin texture. **b** The  $k_{\rm F}$  of the Dirac cone derived from the Hall effect (*black open squares*) agrees well with that directly measured by ARPES (*red solid circles*) if we assume a single spin-polarized Dirac cone on each surface. The  $k_{\rm F}$  is defined to be negative for hole-type Dirac fermions

Fig. 3.10 At T = 1.5 K, the sheet resistance  $R_{\square}$  (a), the carrier density  $|n_{2D}|$  (b), and the mobility  $\mu$  of the Dirac fermions (c) measured all show "V"-shaped x dependence near the charge neutrality point (CNP)



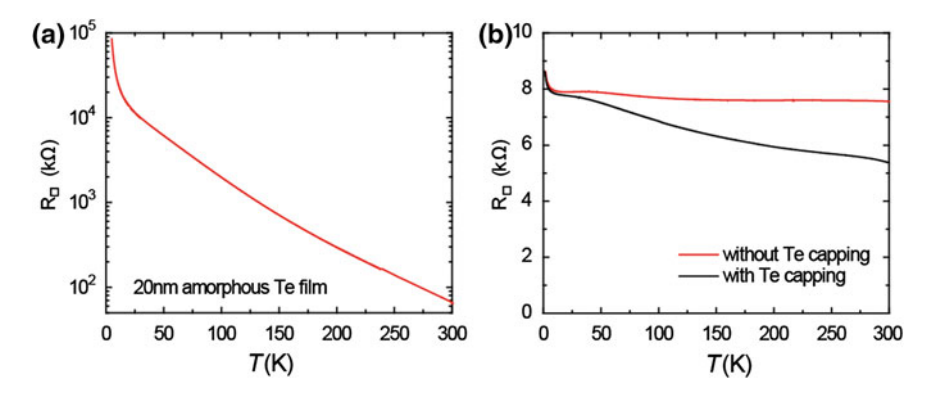
remarkable agreement suggests that the transport properties of the TI surfaces are consistent with that of a single spin-polarized Dirac cone, or a quarter of graphene, as expected by theory.

Figure 3.10a–c summarizes the evolution of the low T transport properties with Sb content x. The resistance value shows a maximum at x=0.94 with  $R_{\square}>10$  k $\Omega$  and decreases systematically on both sides. Correspondingly, the carrier density  $|n_{\rm 2D}|$  reaches a minimum at x=0.96 with  $|n_{\rm 2D}|=1.4\times10^{12}/{\rm cm}^2$  and increases on both sides. Using the measured  $R_{\square}$  and  $|n_{\rm 2D}|$ , the mobility  $\mu$  of the Dirac fermions can be estimated by using the Drude formula  $\sigma_{\rm 2D}=|n_{\rm 2D}|e\mu$ , where  $\sigma_{\rm 2D}=1/R_{\square}$ . As a function of x, the mobility also peaks near the CNP and decreases rapidly on both sides. The "V"-shaped dependence of the transport properties on the Sb content x clearly demonstrate the systematic tuning of the surface band structure across the CNP.

#### 3.3.5 Effect of the Te Capping Layer

For the device structure that we are using, the total measured conductance consists of three terms. In addition to that from the TI film, the conductance of the substrate and the capping layer is also picked up in the measurements. The sapphire substrate is an excellent electrical insulator and its contribution to electrical conduction is negligible. The amorphous Te capping material is a semiconductor with energy gap larger than 300 meV. With a thickness of 20 nm, the Te capping layer should have very small contribution to the transport results. To justify this point, we have measured the resistance of a 20-nm-amorphous Te film grown on sapphire and contacted by Indium electrodes. Figure 3.11a displays the temperature evolution of the sheet resistance of the Te film  $(R_{Te})$ , which shows an insulating behavior over the whole temperature range. The  $R_{\text{Te}}$  value at room temperature is around 70 k $\Omega$ , more than 10 times larger than the total resistance of the most resistive  $(Bi_{1-x}Sb_x)_2Te_3$  film. Therefore, at room temperature the error in the sample resistance value induced by the parallel conduction of the Te capping layer is less than 10 %. The  $R_{\rm Te}$  value increases rapidly with lowering T. It reaches 1 M $\Omega$  at T = 120 K and at the base temperature T = 1.5 K, it is close to 100 M $\Omega$ , which is about four orders of magnitude larger than that in the most resistive x = 0.94 film. Therefore, the contribution of the Te film to the measured transport properties can be safely ignored, especially at the most interesting low T regime where the Hall effect is taken.

Another concern about the Te capping layer is whether it will cause any significant change of the surface electronic structure of the TI films. To clarify this issue, we have measured the transport properties of a 5 QL (Bi<sub>0.04</sub>Sb<sub>0.96</sub>)<sub>2</sub>Te<sub>3</sub> film without Te capping. During the sample mounting process, particular care was taken to minimize the exposure of the film to ambient air. As shown in Fig. 3.11b, at low T the resistance value and the diverging insulating behavior of the uncapped film is highly consistent with that of the Te-capped x = 0.96 film shown in the main text. At high T, there are substantial deviations between the two curves, where the uncapped film shows a larger resistance and weaker T dependence than the capped film. The difference is too large to be explained merely by the parallel conduction from the 20-nm-amorphous Te layer in the capped film. We believe that the larger resistance and weaker T dependence in the uncapped film is mainly due to the surface adsorbates that tends to degrade the quality of the surface and lower the mobility of the surface state Dirac fermions. Nevertheless, the qualitative behavior of the two films is very similar, suggesting that the Te capping layer does not significantly alter the electronic structure and transport properties of the  $(Bi_{1-x}Sb_x)_2Te_3$  films.



**Fig. 3.11** Transport studies on the effect of the amorphous Te capping layer. **a** The temperature evolution of the sheet resistance of the 20-nm-amorphous Te film grown on sapphire substrate showing an insulating behavior. The resistance values are much larger than that of the TI films. **b** The temperature-dependent resistance of the 5 QL (Bi<sub>0.04</sub>Sb<sub>0.96</sub>)<sub>2</sub>Te<sub>3</sub> film covered with Te capping layer (*black*) compared with the one without Te capping (*red*). The transport properties of the films are qualitatively the same

#### 3.4 Discussion and Conclusion

The good agreement with ARPES suggests that the transport results are consistent with the properties of the surface Dirac fermions without bulk contribution. Moreover, the alloying allows us to approach the close vicinity of the CNP, which gives a very low  $|n_{2D}|$  in the order of  $1 \times 10^{12}$  cm<sup>-2</sup>. The  $(Bi_{1-x}Sb_x)_2Te_3$  compounds thus represent an ideal TI system to reach the extreme quantum regime because now a strong magnetic field can squeeze the Dirac fermions to the lowest few Landau levels. Indeed, the Hall resistance of the x = 0.96 film shown in Fig. 3.8 is close to 7 k $\Omega$  at 15 T, which is a significant fraction of the quantum resistance. Future transport measurements on  $(Bi_{1-x}Sb_x)_2Te_3$  films with higher mobility to even stronger magnetic field hold great promises for uncovering the unconventional quantum Hall effect of the topological surface states [26, 27].

The band structure engineering offers many enticing opportunities for designing conceptually new experimental or device schemes based on the TIs. For example, we can apply the idea of compositionally graded doping (CGD) in conventional semiconductor devices [19] to the TIs to achieve spatially variable Dirac cone structures. Figure 3.12a illustrates the schematic of vertical CGD TIs, in which the top and bottom surfaces have opposite types of Dirac fermions and can be used for studying the proposed topological exciton condensation [28]. The spatial asymmetry of the surface Dirac bands can also be used to realize the electrical control of spin current by using the spin-momentum locking in the topological surfaces for

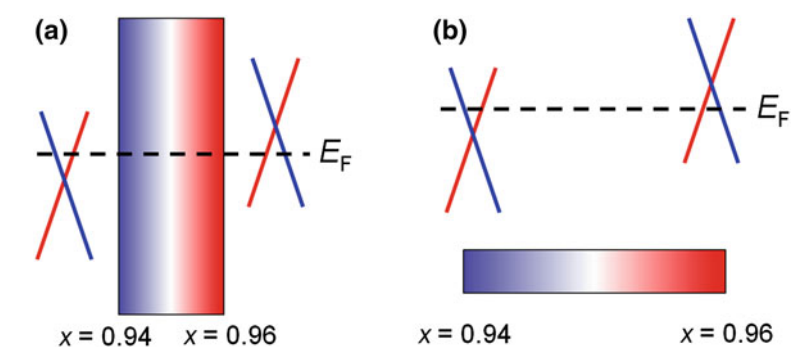


**Fig. 3.12** Schematic device structures of spatially variable Dirac bands grown by compositionally graded doping (CGD) of  $(Bi_{1-x}Sb_x)_2Te_3$  films. Vertical CGD TIs (a) is an ideal system for studying the topological exciton condensation and electrical control of spin current. Horizontal CGD TIs (b) can be used to fabricate a topological p-n junction

spintronic applications [29]. Figure 3.12b illustrates the schematic of horizontal CGD TIs, by which a topological p–n junction between hole- and electron-type TIs can be fabricated.

#### References

- Zhang J, Chang C-Z, Zhang Z, et al. Band structure engineering in (Bi<sub>1-x</sub>Sb<sub>x</sub>)<sub>2</sub>Te<sub>3</sub> ternary topological insulators. Nat Commun. 2011;2:574.
- 2. Schubert EF. Light-emiting diodes. 2nd ed. New York: Cambridge University Press; 2006.
- Stormer HL, Tsui DC, Gossard AC. The fractional quantum Hall effect. Rev Mod Phys. 1999;71:S298–305.
- Fu L, Kane CL. Superconducting proximity effect and Majorana fermions at the surface of a topological insulator. Phys Rev Lett. 2008;100:096407.
- Qi XL, Li R, Zang J, et al. Inducing a magnetic monopole with topological surface states. Science. 2009;323:1184–7.
- Yu R, Zhang W, Zhang HJ, et al. Quantized anomalous hall effect in magnetic topological insulators. Science. 2010;329:61–4.
- 7. Zhang H, Liu C-X, Qi X-L, et al. Topological insulators in Bi<sub>2</sub>Se<sub>3</sub>, Bi<sub>2</sub>Te<sub>3</sub> and Sb<sub>2</sub>Te<sub>3</sub> with a single Dirac cone on the surface. Nat Phys. 2009;5:438–42.
- 8. Peng H, Lai K, Kong D, et al. Aharonov-Bohm interference in topological insulator nanoribbons. Nat Mater. 2010;9:225–9.
- 9. Chen YL, Analytis JG, Chu J-H, et al. Experimental realization of a three-dimensional topological insulator, Bi<sub>2</sub>Te<sub>3</sub>. Science. 2009;325:178–81.
- 10. Taskin AA, Ren Z, Sasaki S, et al. Observation of Dirac holes and electrons in a topological insulator. Phys Rev Lett. 2011;107:016801.
- 11. Hsieh D, Xia Y, Qian D, et al. A tunable topological insulator in the spin helical Dirac transport regime. Nature. 2009;460:1101–5.
- 12. Checkelsky JG, Hor YS, Liu MH, et al. Quantum interference in macroscopic crystals of nonmetallic Bi<sub>2</sub>Se<sub>3</sub>. Phys Rev Lett. 2009;103:246601.

References 53

13. Analytis JG, McDonald RD, Riggs SC, et al. Two-dimensional surface state in the quantum limit of a topological insulator. Nat Phys. 2010;6:960–4.

- 14. Hor YS, Richardella A, Roushan P, et al. p-type Bi<sub>2</sub>Se<sub>3</sub> for topological insulator and low-temperature thermoelectric applications. Phys Rev B. 2009;79:195208.
- 15. Chen J, Qin HJ, Yang F, et al. Gate-voltage control of chemical potential and weak antilocalization in Bi<sub>2</sub>Se<sub>3</sub>. Phys Rev Lett. 2010;105:176602.
- 16. Checkelsky JG, Hor YS, Cava RJ, et al. Bulk band gap and surface state conduction observed in voltage-tuned crystals of the topological insulator Bi<sub>2</sub>Se<sub>3</sub>. Phys Rev Lett. 2011;106:196801.
- 17. Kong D, Dang W, Cha JJ, et al. Few-layer nanoplates of Bi<sub>2</sub>Se<sub>3</sub> and Bi<sub>2</sub>Te<sub>3</sub> with highly tunable chemical potential. Nano Lett. 2010;10:2245–50.
- 18. Steinberg H, Gardner DR, Lee YS, et al. Surface state transport and ambipolar electric field effect in Bi<sub>2</sub>Se<sub>3</sub> nanodevices. Nano Lett. 2010;10:5032–6.
- 19. Capasso F. Band-gap engineering: from physics and materials to new semiconductor-devices. Science. 1987;235:172–6.
- 20. Hsieh D, Xia Y, Qian D, et al. Observation of time-reversal-protected single-dirac-cone topological-insulator states in Bi<sub>2</sub>Te<sub>3</sub> and Sb<sub>2</sub>Te<sub>3</sub>. Phys Rev Lett. 2009;103:146401.
- 21. Jiang Y, Wang Y, Chen M, et al. Landau quantization and the thickness limit of topological insulator thin films of Sb<sub>2</sub>Te<sub>3</sub>. Phys Rev Lett. 2012;108:016401.
- 22. Ren Z, Taskin AA, Sasaki S, et al. Large bulk resistivity and surface quantum oscillations in the topological insulator Bi<sub>2</sub>Te<sub>2</sub>Se. Phys Rev B. 2010;82:241306.
- Fu L, Kane CL. Topological insulators with inversion symmetry. Phys Rev B. 2007;76:045302.
- 24. Hsieh D, Qian D, Wray L, et al. A topological Dirac insulator in a quantum spin Hall phase. Nature. 2008;452:970–4.
- Wang G, Zhu X, Wen J, et al. Atomically smooth ultrathin films of topological insulator Sb<sub>2</sub>Te<sub>3</sub>. Nano Res. 2010;3:874–80.
- Qi X-L, Hughes TL, Zhang S-C. Topological field theory of time-reversal invariant insulators. Phys Rev B. 2008;78:195424.
- 27. Brüne C, Liu CX, Novik EG, et al. Quantum hall effect from the topological surface states of strained bulk HgTe. Phys Rev Lett. 2011;106:126803.
- 28. Seradjeh B, Moore JE, Franz M. Exciton condensation and charge fractionalization in a topological insulator film. Phys Rev Lett. 2009;103:066402.
- Yazyev OV, Moore JE, Louie SG. Spin polarization and transport of surface states in the topological insulators Bi<sub>2</sub>Se<sub>3</sub> and Bi<sub>2</sub>Te<sub>3</sub> from first principles. Phys Rev Lett. 2010;105:266806.

# **Chapter 4 Topology-Driven Magnetic Quantum Phase Transition**

The interplay between the topological insulator and broken time-reversal symmetry (TRS) may create novel quantum effects. In this chapter, we show a magnetic quantum phase transition (QPT) accompanied by the sign reversal of the anomalous Hall effect in Cr-doped  $Bi_2(Se_xTe_{1-x})_3$  topological insulator films grown by MBE. Across the critical point, a topological QPT is revealed by both ARPES measurements and density functional theory (DFT) calculations. We show that the bulk band topology is the fundamental driving force for the magnetic QPT, where the ferromagnetic order is strongly promoted by non-trivial  $Z_2$  topology. The tunable topological and magnetic properties in this system provide an ideal platform for realizing the exotic topological quantum phenomena in magnetic topological insulators. The main findings and conclusions in this chapter have been published in Ref. [1], reprinted with the permission of full text and figures from AAAS.

#### 4.1 Introduction to Magnetic Topological Insulator

The massless Dirac fermions in the topological surface states are protected by the TRS [2–4], which is broken by magnetically doped topological insulator, especially in the presence of long-range ferromagnetic order. Although breaking the TRS is generally detrimental to the topological surface states, it may also lead to some exotic topological quantum effects unique to the TIs. For example, a magnetic film deposited on the surface of a TI is proposed to induce the image magnetic monopoles [5]. An ultrathin film of magnetically ordered TI is expected to exhibit the quantized anomalous Hall effect in zero magnetic field [6, 7] (Chap. 5). Giant magneto-optical effects may be created when a TI is weakly exchange coupled to a ferromagnet [8], and a dissipationless inverse spin-galvanic effect may be induced when a monolayer insulating ferromagnet is deposited on the surface of a TI [9]. A key step for realizing and investigating these novel quantum states of matter is to

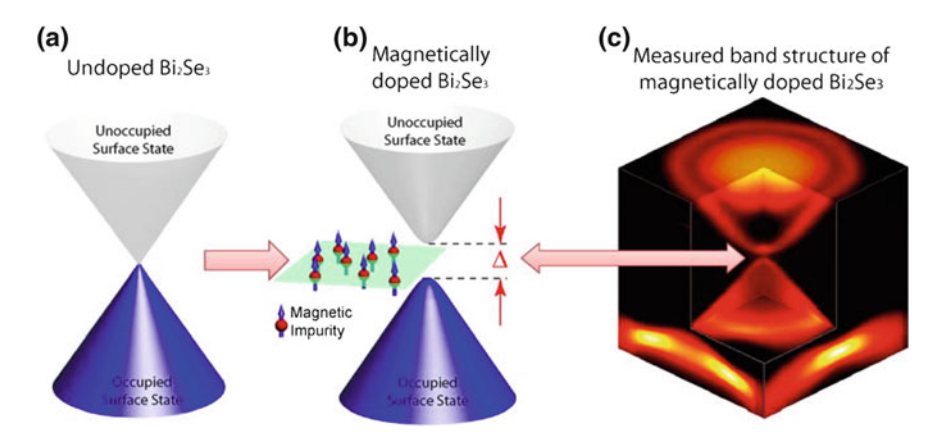


**Fig. 4.1 a** Illustration of the topological surface states with a gapless Dirac cone structure in undoped Bi<sub>2</sub>Se<sub>3</sub>. **b** A gap is opened at the Dirac point by introducing the magnetic impurities with ferromagnetic order. **c** ARPES measurements of the electronic band structure of a Fe-doped Bi<sub>2</sub>Se<sub>3</sub> sample show that the upper and lower Dirac cones are separated by a Dirac gap. Figures are adapted from http://www-ssrl.slac.stanford.edu/ by the courtesy of Y.L. Chen

tune the magnetic ordering in TIs in a controlled manner and recognize the underlying topological connections.

With their relatively large bulk gap and single surface Dirac cone, the prototypical 3D TIs  $Bi_2Se_3$  and  $Bi_2Te_3$  [10–12] are widely used as hosts for TRS-breaking perturbations. As shown in Fig. 4.1, on the cleaved surface of Fe-doped  $Bi_2Se_3$  single crystal, ARPES measurements reveal the opening of an energy gap at the Dirac point [13], which is possibly caused by the ferromagnetic order on the surface induced by Ruderman–Kittel–Kasuya–Yosida (RKKY) interaction [14, 15]. In addition, Fe atoms deposited on the surface of  $Bi_2Se_3$  single crystal are found to create odd multiples of Dirac-like surface states above the original (gaped) Dirac point [16]. Moreover, spin-resolved ARPES reveals that the spin textures of the surface states exhibit a hedgehog-like structure in Mn-doped  $Bi_2Se_3$ , which directly demonstrate the consequence of TR symmetry breaking on the surface [17].

STM/STS measurements on the surface of magnetically Fe-doped  $Bi_2Te_3$  crystals demonstrate that breaking TRS can lead to several new scattering channels along high-symmetry directions in the momentum space [18]. In Mn-doped  $Bi_2Te_3$  and  $Bi_2Se_3$ , when approaching the Dirac point, the dopants result in pronounced nanoscale spatial fluctuations of energy, momentum, and helicity [19].

Comparing to the surface-sensitive techniques (ARPES and STM), the magnetization and transport measurements are the most straightforward methods to probe the underlying magnetic properties. In Mn-doped  $Bi_2Te_3$  single crystals, magnetization measurements demonstrate a bulk ferromagnetic (FM) state with the Curie temperature of around 9–12 K [20] and the easy axis of magnetization is perpendicular to the  $Bi_2Te_3$  basal plane. Furthermore, STM topography analysis shows that the Mn substitutions (on the Bi sites) are randomly distributed, indicating the

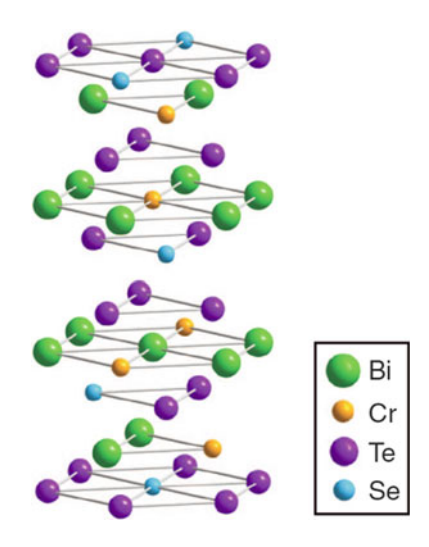
absence of Mn clustering. However, the ferromagnetic hysteresis is not observed in anomalous Hall effect measurements at temperature (5 K) below the Curie temperature of  $Bi_{1.96}Mn_{0.04}Te_3$  ( $T_C \sim 9$  K). Nevertheless, the moment per  $Bi_{2-x}Mn_xTe_3$  formula unit is substantially larger than that observed in the Fe-doped  $Bi_{2}Te_{3}$  crystals [21], where analogous ferromagnetic order is observed in the magnetization measurements. Moreover, a Dirac fermion-mediated ferromagnetism was reported by the transport measurements in Mn-doped  $Bi_{2}(Se,Te)_{3}$  thin flakes [22]. In this system, the Fermi level was tuned into the bulk band gap by both solid dielectric gating and ionic liquid gating. Therefore, the ferromagnetic order can only be supported by surface electrons.

In magnetically doped  $Bi_2Se_3$ , the intrinsic ferromagnetic order is seldom reported. For instance, in  $Bi_{1.96}Fe_{0.04}Se_3$ , the ferromagnetic order is not observed from room temperature down to 2 K [21]. Similarly, the bulk paramagnetic state is also reported in  $Bi_{1.98}Gd_{0.02}Se_3$  and  $Bi_{1.98}Cr_{0.02}Se_3$  single crystals [23]. Although some groups have reported an in-plane ferromagnetism in Mn-doped  $Bi_2Se_3$  thin films [24] and  $Fe_7Se_8/Bi_2Se_3$  intergrowth crystals [25], it is not an intrinsic behavior due to the segregation of the magnetic atoms or phase separation during the sample growth. In Cr-doped  $Bi_2Se_3$  epitaxial thin films, the in-plane ferromagnetism is revealed for Cr content x = 5.2 % [26]. However, when x is increased to 9.9 %, the ferromagnetism nearly vanishes, which probably results from the poor sample quality at higher Cr concentration as acknowledged by the authors. Thus, this ferromagnetism in Cr-doped  $Bi_2Se_3$  is possibly an extrinsic effect.

#### 4.2 Motivation and Experimental Design

Most of these previous studies focus on the effect of magnetism on the topological surface states, and little is known about the other side of the story, i.e., how the magnetic ordering is affected by the topological property. Since the  $Z_2$  bulk topology is the most fundamental identity of a TI, we anticipate that it must also play a crucial role in determining the phases and phase transitions in magnetically doped TIs. To test this conjecture, we fabricate Cr-doped  $Bi_2(Se_xTe_{1-x})_3$  TI films using MBE method. By varying the mixing ratio of Bi<sub>2</sub>Se<sub>3</sub> to Bi<sub>2</sub>Te<sub>3</sub>, we can actively modify the strength of spin-orbit coupling (SOC), which is essential for the band inversion of TIs. Figure 4.2 depicts the schematic structure of Bi<sub>2-v</sub>Cr<sub>v</sub>(Se<sub>x</sub>Te<sub>1</sub>  $_{-x}$ )<sub>3</sub>, where the Cr dopants substitute the Bi sites and Se/Te atoms are randomly mixed. All the films studied here have the same thickness d = 8 QL so that they are in the 3D regime with decoupled surfaces [27]. The Cr content is fixed at y = 0.22because at this doping level the density of local moments is high enough to sustain long-range magnetic order, and the SOC strength is reduced to the verge of a topological phase transition [28]. The schematic device for the magnetotransport measurements on the TI films is displayed in Fig. 2.8a, where the external magnetic field (H) is perpendicular to the film plane.

Fig. 4.2 The schematic crystal structure of Bi<sub>2</sub>  $_{-y}$ Cr<sub>y</sub>(Se<sub>x</sub>Te<sub>1-x</sub>)<sub>3</sub> (two QLs are shown). The Cr dopants substitute the Bi sites, and Se/Te atoms are randomly mixed



#### 4.3 Sample Characterization

The MBE-grown films are characterized by RHEED during growth, in suit STM topography, and ex suit X-ray diffraction (XRD) measurements. Sharp  $1 \times 1$  RHEED patterns can always be observed on the 8 QL  $Bi_{1.78}Cr_{0.22}(Se_xTe_{1-x})_3$  samples.

Figure 4.3 shows the XRD pattern of 45 QL pure  $Bi_2Se_3$  film and the  $Bi_{1.78}Cr_{0.22}Se_3$  film. The (006), (009), (0012), (0015), (0018), and (0021) XRD peaks are very clear. The inset shows that the full width at half maximum (FWHM) of the (006) peak of the  $Bi_{1.78}Cr_{0.22}Se_3$  film is around 0.2°, which indicates the high quality of the sample.

The typical STM topographic images of the surface of Bi<sub>1.87</sub>Cr<sub>0.13</sub>Te<sub>3</sub> are presented in Fig. 4.4. The centers of dark triangles are identified as the Cr substitutions on Bi sites, which are covered by topmost Te layer. Segregated nanoscale clusters do not exist even in the large-scale topography.

#### **4.4 Transport Measurements**

This section reports the transport results of 8 QL Bi<sub>1.78</sub>Cr<sub>0.22</sub> (Se<sub>x</sub>Te<sub>1-x</sub>)<sub>3</sub> films with  $0 \le x \le 1$ . The field dependence of Hall effect and magnetoresistance (MR) are measured at a temperature range from 1.5 to 100 K. To reveal the magnetic anisotropy and confirm the paramagnetism, MR measurements are performed under different magnetic field orientations.

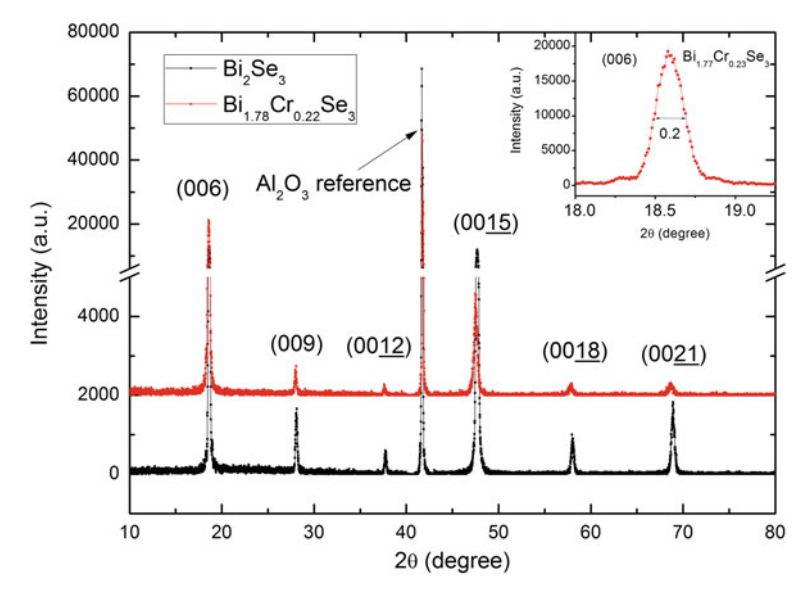


Fig. 4.3 XRD patterns of the  $Bi_{1.78}Cr_{0.22}Se_3$  film. The *sharp peaks* indicate high quality of the sample. The *inset panel* is an enlarged view on (006) peak

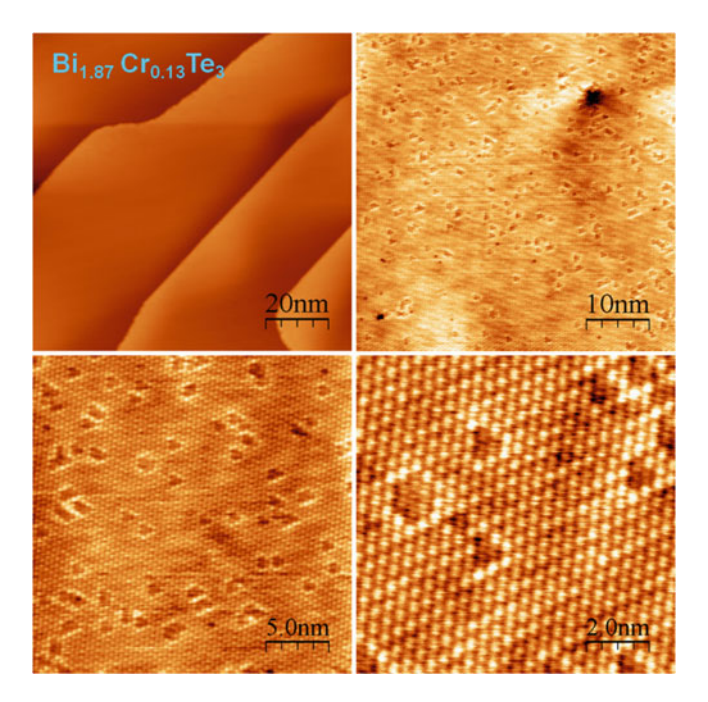


Fig. 4.4 STM topography of  $\mathrm{Bi_{1.87}Cr_{0.13}Te_3}$  film reveals the absence of Cr clusters even in the large-scale topographic image

## 4.4.1 Magnetic Quantum Phase Transition in $Bi_{1.78}Cr_{0.22}(Se_xTe_{1-x})_3$

We first discuss the transport properties of Cr-doped Bi<sub>2</sub>Te<sub>3</sub> under a perpendicular magnetic field. Figure 4.5a shows the field-dependent Hall effect curves of the 8 QL Bi<sub>1.78</sub>Cr<sub>0.22</sub>Te<sub>3</sub> film taken at varied temperatures (T). At the base temperature T = 1.5 K, the Hall effect shows a hysteretic loop and a nearly square-shaped positive jump, which are the hallmarks of anomalous Hall effect (AHE) in FM conductors [29]. The total 2D Hall resistivity  $\rho_{yx}$  in this case can be expressed as follows:

$$\rho_{vr} = R_{A}M(T, H) + R_{A}H \tag{4.1}$$

Here, M(T, H) is the magnetization and  $R_{\rm A}$  and  $R_{\rm N}$  are the anomalous and normal Hall coefficients, respectively. Both the anomalous Hall resistivity and the coercive force ( $H_{\rm coer}$ ) decrease as T rises. The Hall traces become fully reversible at T > 20 K, indicating that the Curie temperature  $T_{\rm C}$  of this film is around 20 K. The normal Hall effect at high H has a negative slope for the entire temperature range, indicating the existence of electron-type charge carriers (Fig. 4.12). The magnetoconductivity (MC) curves taken at  $T < T_{\rm C}$  show butterfly-shaped hysteresis at weak H (Fig. 4.5b), as commonly observed in FM metals. MC keeps decreasing at higher H, indicative of the weak localization (WL) of charge carriers instead of the weak antilocalization (WAL) in pristine Bi<sub>2</sub>Te<sub>3</sub> [30].

The Cr-doped  $Bi_2Se_3$ , on the other hand, exhibits a totally different transport behavior. Figure 4.6a shows the Hall effect measured on the  $Bi_{1.78}Cr_{0.22}Se_3$  film. At T = 1.5 K, the Hall trace has a pronounced negative curvature at weak H but shows no observable hysteresis. These features are consistent with the field-induced AHE

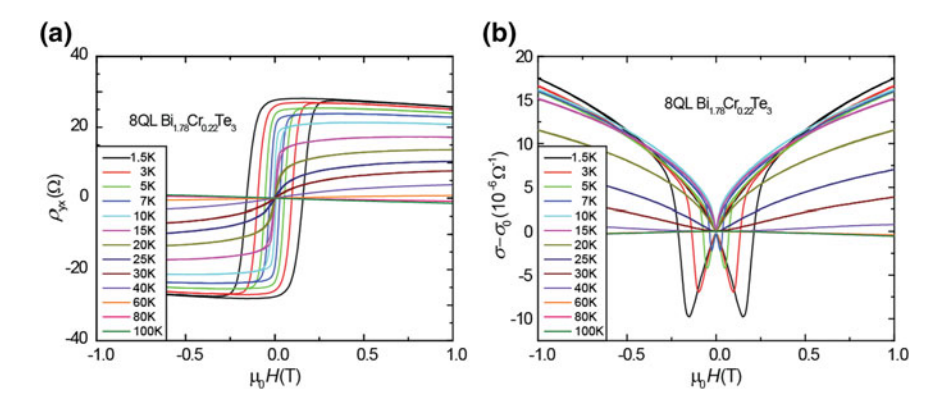


**Fig. 4.5** Transport results on 8 QL  $\rm Bi_{1.78}Cr_{0.22}Te_3$ . **a** The Hall effect of  $\rm Bi_{1.78}Cr_{0.22}Te_3$  film shows hysteretic loops below  $T_{\rm C}=20~\rm K$  with a positive AHE term. **b** The MC curves show a *butterfty-shaped* hysteresis pattern

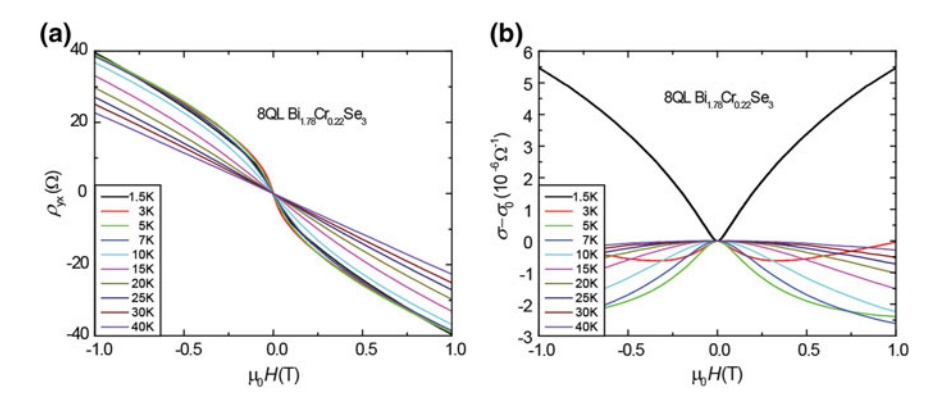


**Fig. 4.6** Transport results on 8 QL  $\mathrm{Bi}_{1.78}\mathrm{Cr}_{0.22}\mathrm{Se}_3$ . **a** The Hall effect shows no hysteresis even at low T, and only a negative curvature is observed. **b** The MC displays a crossover from WL to WAL as temperature increases

in paramagnetic (PM) materials without spontaneous magnetization. Figure 4.6b displays the MC curves measured on the same film, which again shows no sign of hysteresis even at the base temperature. Here, the MC changes from negative at low T to positive at high T, consistent with the WL to WAL crossover reported in 3 QL  $Bi_2Se_3$  with similar Cr content [31]. The possible existence of in-plane ferromagnetism in the  $Bi_{1.78}Cr_{0.22}Se_3$  film is also ruled out by magnetization and magnetotransport measurements with H applied along the film plane (Figs. 4.14b and 4.16).

There are two striking differences between the magnetotransport properties of Cr-doped  $Bi_2Te_2$  and  $Bi_2Se_3$ . The former has a FM ground state with positive AHE, whereas the latter remains PM down to the base temperature and has a negative AHE. To unveil the origin of the sharp contrast between these two phases, we fabricate Cr-doped  $Bi_2(Se_xTe_{1-x})_3$ , which are isostructural isovalent mixtures of  $Bi_2Te_3$  and  $Bi_2Se_3$ . Figure 4.7 displays the Hall traces measured on five  $Bi_{1.78}Cr_{0.22}$ 

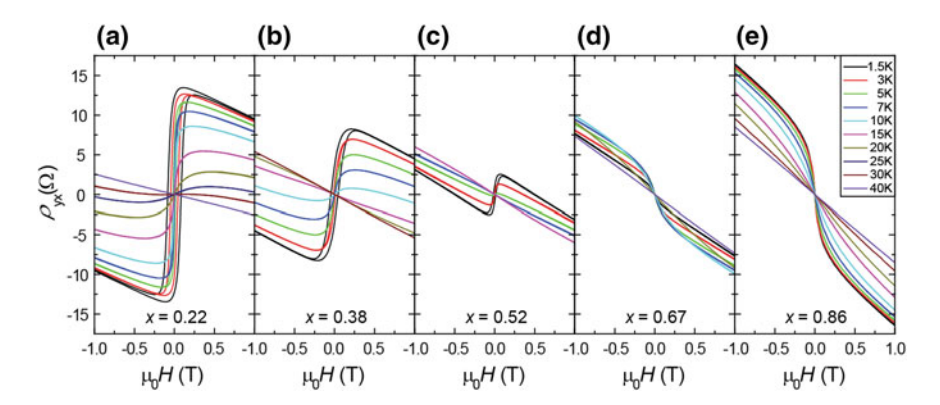


**Fig. 4.7** The field-dependent Hall traces of 8 QL  $Bi_{1.78}Cr_{0.22}(Se_xTe_{1-x})_3$  films with  $0.22 \le x \le 0.86$  measured at varied temperatures

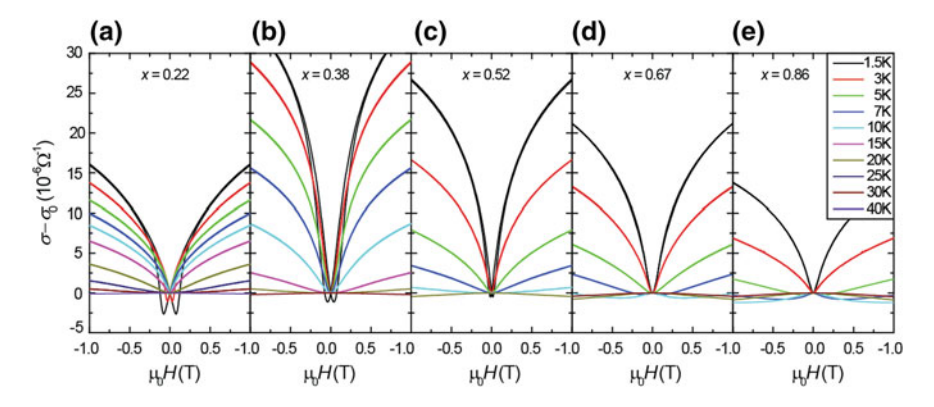


Fig. 4.8 The MC curves for the 8 QL  $Bi_{1.78}Cr_{0.22}(Se_xTe_{1-x})_3$  films with  $0.22 \le x \le 0.86$  at varied T

 $(Se_xTe_{1-x})_3$  films with  $0.22 \le x \le 0.86$ . The three Te-rich samples with  $x \le 0.52$  all show FM ordering at low T as seen by the apparent hysteresis. As the Se content is increased to x = 0.67, however, the hysteresis disappears and the system enters the PM phase. Interestingly, the sign of the AHE term also reverses to negative right at this doping. With the further increase of x to 0.86, the system remains PM and the negative AHE becomes more pronounced.

The FM to PM phase transition can also be seen in the MC curves measured on the same films as shown in Fig. 4.8. The three samples with  $x \le 0.52$  all show a butterfly-shaped hysteresis pattern for T below  $T_{\rm C}$ . Both the low T coercive force  $H_{\rm coer}$  and  $T_{\rm C}$  decrease as Se content x increases from 0.22 to 0.52, indicating weakened FM order. With the further increase of x from 0.67 to 0.86, the hysteresis totally disappears even at the base T, indicating the PM ground state in this regime.

Figure 4.9a summarizes the Hall and MC curves of all the  $Bi_{1.78}Cr_{0.22}(Se_xTe_1 - x)_3$  samples measured at T = 1.5 K. The Hall curves reveal a highly systematic

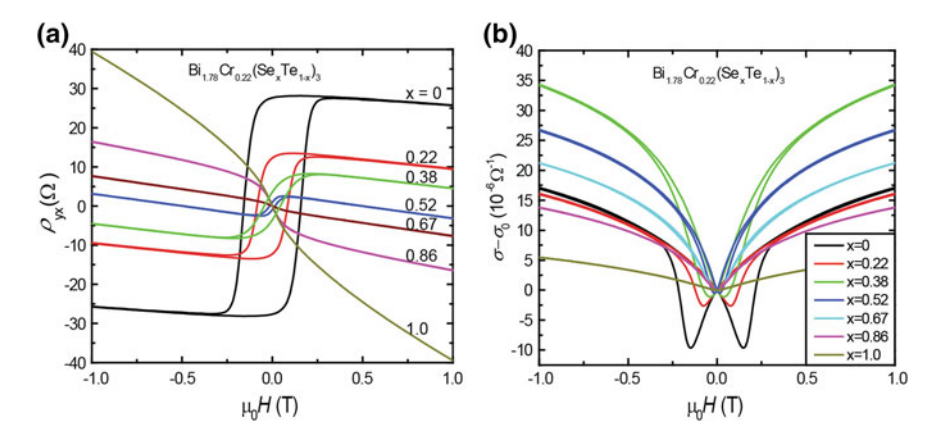
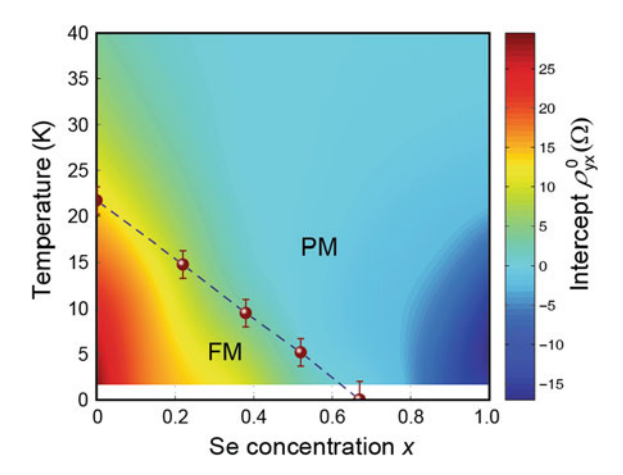


Fig. 4.9 Systematic evolution of the Hall effect (a) and MC (b) of all the samples  $(0 \le x \le 1)$  measured at T = 1.5 K

Fig. 4.10 The magnetic phase diagram of Bi<sub>1.78</sub>Cr<sub>0.22</sub>(Se<sub>x</sub>Te<sub>1-x</sub>)<sub>3</sub> summarizing the intercept  $\rho_{yx}^0$  as a function of Se concentration x and temperature T. The  $T_C$  of the FM phase is indicated by the *solid symbols* 



evolution of  $H_{\text{coer}}$  and the intercept Hall resistivity  $\rho_{yx}^0$  obtained by extrapolating the high H linear Hall curve back to zero field (Fig. 4.11a). For the MC curves, as the Se content x increases from 0 to 0.52, the butterfly-shaped hysteretic loop shrink systematically and disappear altogether when x > 0.67.

Since the magnetism of the system can be characterized by the anomalous Hall effect, we can draw the T versus x magnetic phase diagram by plotting the  $\rho_{yx}^0$  values of each sample using the color scale (Fig. 4.10). At the base temperature T=1.5 K, the phase diagram is separated into two distinct regimes: a FM phase with positive  $\rho_{yx}^0$  and a PM phase with negative  $\rho_{yx}^0$ . Since the transition between the two magnetic phases occurs at the ground state, it is a QPT driven by the change of chemical composition. The quantum critical point (QCP)  $x_c \sim 0.63$  can be estimated from the interpolated x value when  $\rho_{yx}^0$  changes sign (Fig. 4.11b). The pronounced quantum critical fluctuations near the QCP are also clearly illustrated in

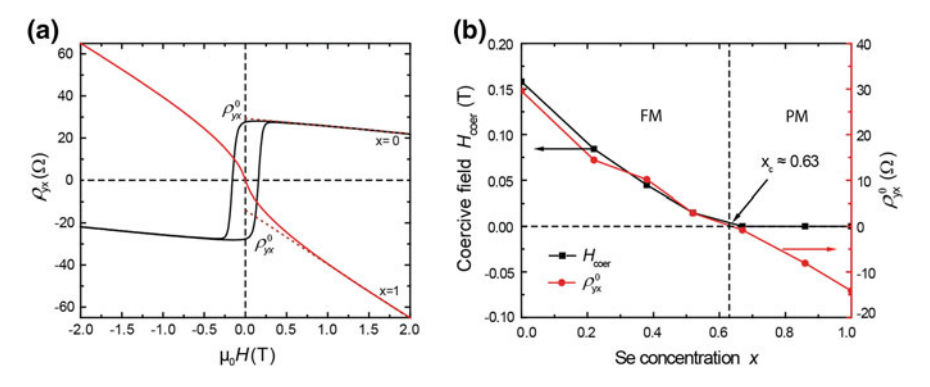


Fig. 4.11 a The *broken lines* demonstrate the linear extrapolation of the Hall curves back to zero field to extract the intercept  $\rho_{vv}^0$  value. b The x dependence of  $H_{coer}$  and  $\rho_{vv}^0$  at T = 1.5 K

the phase diagram. The solid symbols in Fig. 4.10 indicate the  $T_{\rm C}$  of each sample determined by the temperature when  $H_{\rm coer}$  becomes zero.

# 4.4.2 Methods for the Detection of $\rho_{vx}^0$ and $\mathbf{x}_c$

Figure 4.11a shows the Hall effect of 8 QL Bi<sub>1.78</sub>Cr<sub>0.22</sub>Te<sub>3</sub> and Bi<sub>1.78</sub>Cr<sub>0.22</sub>Se<sub>3</sub> films measured at T=1.5 K. The intercept  $\rho_{yx}^0$  plotted in Fig. 4.10 is obtained by extrapolating the linear part of the Hall curve (roughly between 1 and 2 T) back to zero magnetic field. For the PM Bi<sub>1.78</sub>Cr<sub>0.22</sub>Se<sub>3</sub> sample, this renders a negative  $\rho_{yx}^0$  value, and for the FM Bi<sub>1.78</sub>Cr<sub>0.22</sub>Te<sub>3</sub> sample, the  $\rho_{yx}^0$  is positive and the value is close to the residual Hall resistivity at zero field. The  $\rho_{yx}^0$  values of the other samples are determined by the same procedure.

Figure 4.11b summarizes the x dependence of  $H_{\rm coer}$  and the intercept  $\rho_{yx}^0$ . The phase diagram is separated into two distinct regimes: a FM phase with positive  $\rho_{yx}^0$  and a PM phase with negative  $\rho_{yx}^0$ . The QCP  $x_{\rm c} \sim 0.63$  of the QPT can be estimated from the interpolated x value when  $\rho_{yx}^0$  changes sign.

### 4.4.3 The High-Field Hall Effect in Bi<sub>1.78</sub>Cr<sub>0.22</sub>Te<sub>3</sub>

In Fig. 4.5a, the low-field Hall effect of the 8 QL Bi<sub>1.78</sub>Cr<sub>0.22</sub>Te<sub>3</sub> film is displayed. At T = 5 K, the slope of the normal Hall effect at high field is negative, consistent with the electron-type charge carriers as seen by the ARPES measurements (Fig. 4.17a). In the temperature range between 20 K < T < 60 K, however, the low-field slope of the Hall effect seems to be positive. This is not due to the change of carrier type to holelike, but is due to the ferromagnetic fluctuations above the Curie temperature  $T_C = 20$  K. In this regime, a small magnetic field can induce a sizable magnetization, which leads to a positive curvature in the Hall effect, just like the anomalous Hall effect below  $T_{\rm C}$  except for the absence of hysteresis. To demonstrate this point, we extended the Hall effect in this sample to higher temperatures and fields, as shown in Fig. 4.12. At T much higher than  $T_C$  (T = 80 and 100 K), the fluctuation effect is weak and the low-field Hall slope shows a negative slope. Even for T just above  $T_{\rm C}$  when the fluctuation is strong, the slope of the Hall curve becomes negative at sufficiently high magnetic field when the normal Hall effect dominates. Both observations indicate that the charge carriers in Cr-doped Bi<sub>2</sub>Te<sub>3</sub> are always electron type for the entire temperature range.

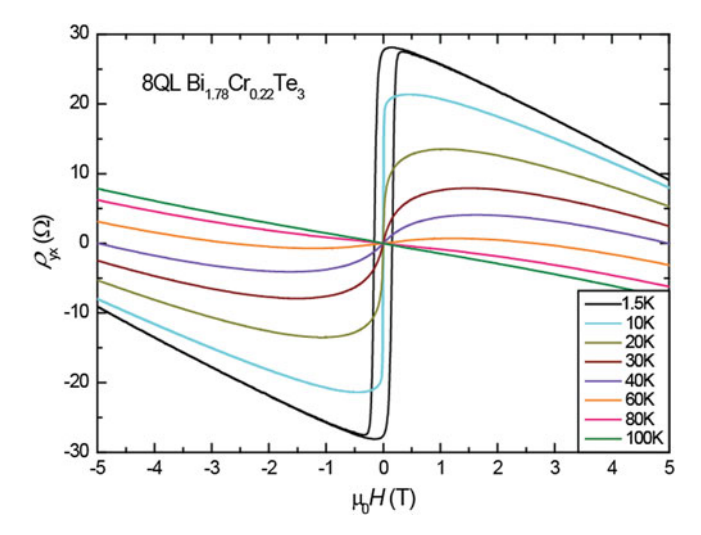


Fig. 4.12 High-field Hall effect of the  $\rm Bi_{1.78}Cr_{0.22}Te_3$  film up to 5 T at varied temperatures from 1.5 to 100 K

## 4.4.4 Magnetic Anisotropy Measurements in Bi<sub>1.78</sub>Cr<sub>0.22</sub>Te<sub>3</sub>

The magnetic anisotropy is another important property of a FM material. To reveal the magnetic anisotropy of the 8 QL Bi<sub>1.78</sub>Cr<sub>0.22</sub>Te<sub>3</sub> film, we performed MR measurements under different magnetic field orientations. Figure 4.13 shows  $\rho_{xx}(B)/\rho_{xx}(0)$ , the normalized magnetoresistance (MR), measured at T=1.5 K with a different polar angle ( $\theta$ ) between the magnetic field and the normal line of the film as indicated by the schematic in the inset of Fig. 4.13b. For  $\theta=0$  (90°), the magnetic field is perpendicular (parallel) to the in-plane electric current direction. With increasing  $\theta$ , the strength of hysteresis decreases continuously and becomes extremely small for an in-plane field ( $\theta=90^{\circ}$ ). This is a very strong indication of an out-of-plane magnetic anisotropy.

Another trend revealed by Fig. 4.13a is the increase of the apparent coercive force with increasing  $\theta$ . This is not due to the increase of coercivity, but instead, it is due to the decrease of the perpendicular component of the field as  $\theta$  increases. In Fig. 4.13b, we plot the normalized MR curves versus the normal component of magnetic field  $H_{\perp} = H_{\text{total}} \cdot \cos\theta$ . It is evident that the coercive force decreases with increasing  $\theta$  and becomes very small for field close to the in-plane orientation, again demonstrating the out-of-plane magnetic anisotropy.

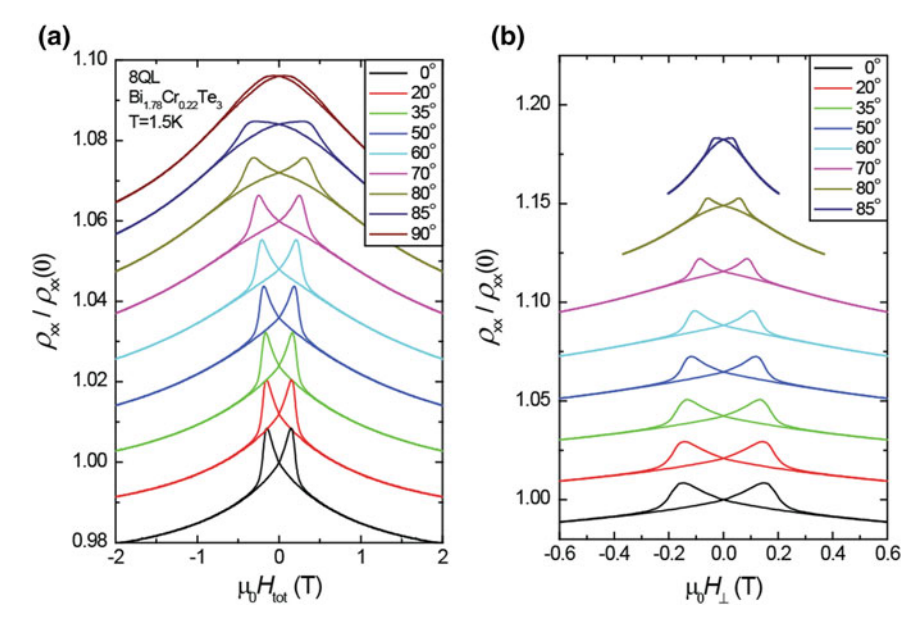


Fig. 4.13 The angle dependence of normalized MR of the 8 QL Bi<sub>1.78</sub>Cr<sub>0.22</sub>Te<sub>3</sub> film as a function of total magnetic field (a) and the normal component of the field (b) at T = 1.5 K

### 4.4.5 Further Proof of Paramagnetism in Bi<sub>1.78</sub>Cr<sub>0.22</sub>Se<sub>3</sub>

In addition to these AHE measurements with perpendicular magnetic field, we also carried out magnetic anisotropy measurements on 8 QL  $\rm Bi_{1.78}Cr_{0.22}Se_3$  films under both out-of-plane and in-plane magnetic fields. And all the experimental results explicitly support that the  $\rm Bi_{1.78}Cr_{0.22}Se_3$  films studied in our work are paramagnetic at any direction.

Figure 4.14a shows the MR measurements on the 8 QL  $\rm Bi_{1.78}Cr_{0.22}Se_3$  film at T=1.5 K with a rotating field from out-of-plane to in-plane, where the weak localization behavior is present and no hysteresis loops are observed. In Fig. 4.14b, the magnetic field is rotated within the in-plane orientation with several different angles between the field and the electric current. The weak localization behavior is present at all angles, but there is no observable hysteresis in any of the curves, which is consistent with the magnetization measurements (Fig. 4.16). Since MR is very sensitive to long-range ferromagnetic ordering, these results provide transport evidence for the absence of ferromagnetic ordering in the  $\rm Cr_{0.22}Bi_{1.78}Se_3$  film at any direction.

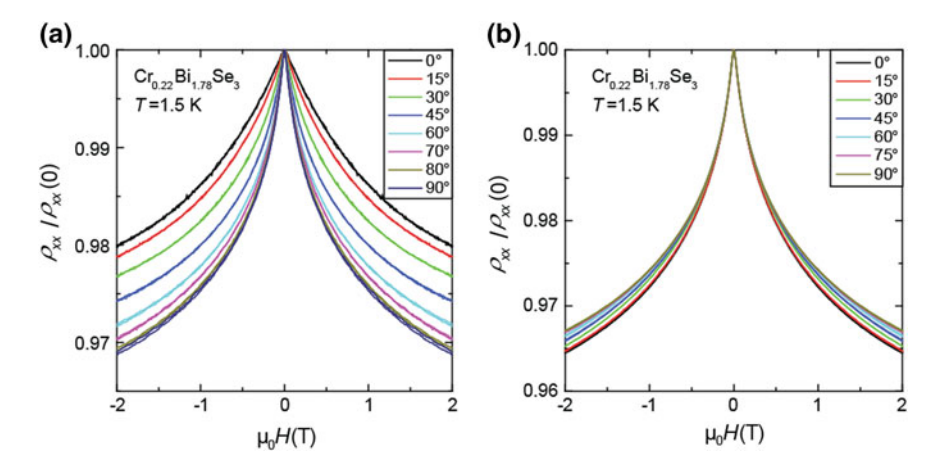


Fig. 4.14 The magnetic anisotropy measurements of 8 QL  $\rm Bi_{1.78}Cr_{0.22}Se_3$  films under both out-of-plane and in-plane magnetic fields at  $T=1.5~\rm K$ 

#### 4.5 SQUID Magnetization Measurements

To clarify whether the ferromagnetism in the samples studied here is a bulk phenomenon or a surface effect, we use a superconducting quantum interference device (SQUID) magnetometer to measure the magnetization of a 50 QL Bi<sub>1.78</sub>Cr<sub>0.22</sub>Te<sub>3</sub> film with area 12 mm<sup>2</sup> grown on sapphire substrate. The 8 QL film studied by transport in the main text is too thin to exhibit sufficiently large magnetic signal. Shown in Fig. 4.15a is the M-H loop measured at T = 2 K on the 50 QL sample. At high field, M is linear to H with a negative slope, which is due to the diamagnetic signal mainly from the substrate. At low field ( $\mu_0 H < 0.2 \text{ T}$ ), a strongly hysteretic M-H loop appears, indicating the FM behavior of the sample. The magnetization of the film can be obtained after the diamagnetic background is subtracted. Next, we estimate the magnetic moment contributed by each Cr dopant. The volume of the 50 QL film is about 12 mm<sup>2</sup> × 51 nm =  $6.12 \times 10^{-7}$  cm<sup>3</sup>, and the saturated magnetic moment per unit volume is about  $2.4 \times 10^{-5}$  emu/ $6.12 \times 10^{-7}$  cm<sup>3</sup> = 39.2 emu/cm<sup>3</sup>. Since the volume of one unit cell of Bi<sub>2</sub>Te<sub>3</sub> is 158 Å<sup>3</sup>, the magnetic moment per unit cell is 39.2 emu/cm<sup>3</sup> × 158 Å<sup>3</sup> =  $6.2 \times 10^{-21}$  emu =  $0.667 \mu_B$ . Therefore, the magnetic moment per Cr dopant can be derived to be 0.667  $\mu_B/0.22 = 3.0 \mu_B$  as shown in Fig. 4.15b. This is very strong evidence that all of the Cr<sup>3+</sup> cations contribute to the magnetization. Therefore, the ferromagnetic ordering is definitely a bulk phenomenon.

The paramagnetism of the  $Bi_{1.78}Cr_{0.22}Se_3$  films is further confirmed by the SQUID magnetization measurements with the in-plane magnetic field. And all the experimental results explicitly support that the  $Bi_{1.78}Cr_{0.22}Se_3$  films studied in our work are paramagnetic both in the out-of-plane and in the in-plane directions. Shown in Fig. 4.16 is the magnetization results measured by SQUID magnetometry

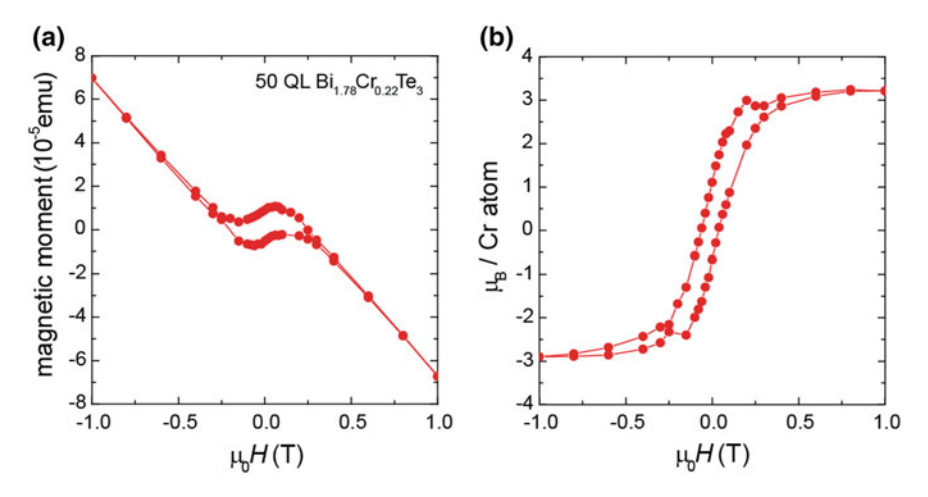
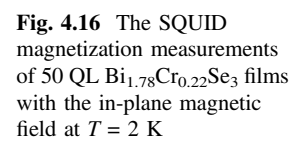
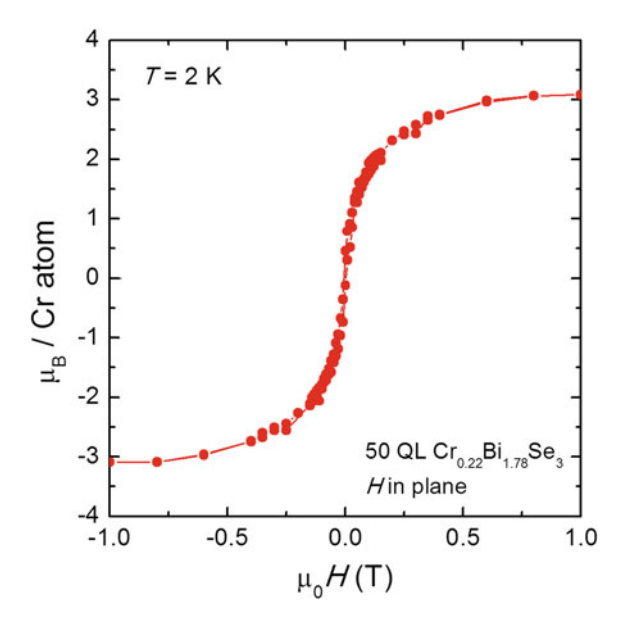


Fig. 4.15 The SQUID magnetization measurements of 50 QL  $Bi_{1.78}Cr_{0.22}Te_3$  film at T = 2 K





on 50 QL Bi<sub>1.78</sub>Cr<sub>0.22</sub>Se<sub>3</sub> film at T=2 K with the magnetic field applied within the plane of the film. The M-H loops of the film have negligible hysteresis, indicating that it has no long-range ferromagnetic ordering. This behavior contrasts strongly with the clear ferromagnetic ordering in Bi<sub>1.78</sub>Cr<sub>0.22</sub>Te<sub>3</sub> with out-of-plane anisotropy, as shown in Fig. 4.15. And the magnetic moment per Cr dopant is also about 3.0  $\mu_{\rm B}$ . This indicates that even the paramagnetism in Bi<sub>1.78</sub>Cr<sub>0.22</sub>Se<sub>3</sub> films is a bulk phenomenon and not dominated by surface states.

#### 4.6 ARPES Band Mapping

This section reports the band structure evolution of  $Bi_{2-y}Cr_y(Se_xTe_{1-x})_3$  films as a function of Se and Cr concentrations. In the ARPES band maps, an explicit topological QPT is revealed in  $Bi_{1.78}Cr_{0.22}(Se_xTe_{1-x})_3$  system as well as a bulk band closing and reopening process in  $Bi_{2-y}Cr_ySe_3$  films. Furthermore, in  $Bi_{2-y}Cr_yTe_3$  system, the surface states are shown to exist with the Cr concentration up to y = 0.23 and vanish for y = 0.38.

# 4.6.1 Topological Quantum Phase Transition in $Bi_{1.78}Cr_{0.22}(Se_xTe_{1-x})_3$

ARPES measurements on the  $Bi_{1.78}Cr_{0.22}(Se_xTe_{1-x})_3$  system uncover a surprising feature. Figure 4.17a-f displays the ARPES band maps taken at T = 120 K when all the samples are in the PM states. The Fermi level  $(E_{\rm F})$  of all the samples lies above the Dirac point, consistent with the electron-type charge carriers revealed by the negative slope of the normal Hall effect. The three samples with  $x \le 0.52$  show well-defined gapless surface states with linear dispersions. The surface state features can be better identified by the dual-peak structures around the  $\Gamma$  point in the momentum distribution curves (MDCs) shown in Fig. 4.17g-l. As x is increased to x = 0.67 (Fig. 4.17d), however, the surface state features cannot be resolved from the band map. The MDCs in Fig. 4.17j also exhibit a single broad peak characteristic of the bulk states. Moreover, a small energy gap starts to appear at the  $\Gamma$ point of the band structure. With further increase of x up to 1, the surface states are always absent, while the gap amplitude keeps increasing. Since the Dirac surface states derive from the non-trivial  $Z_2$  bulk topology, their absence for  $x \ge 0.67$ suggests that the bulk band structure in this regime is topologically trivial. Therefore, the ARPES results reveal a topological QPT, namely a transition from the TI to trivial band insulator, accompanying the magnetic QPT. The overall features of the ARPES results are very similar to those in the BiTl( $S_{1-\delta}Se_{\delta}$ )<sub>2</sub> TIs showing the topological QPT induced by S substitution of Se [32, 33].

# 4.6.2 Similar Topological QPT in $Bi_{2-y}Cr_ySe_3$ and $Bi_{2-y}Cr_yTe_3$

In addition to the band mapping in  $Bi_{1.78}Cr_{0.22}(Se_xTe_{1-x})_3$  system, we have performed a series of ARPES measurements on  $Bi_{2-y}Cr_ySe_3$  films with systematically varied Cr contents. Shown in Fig. 4.18 are ARPES band maps along the  $\Gamma$ -K- $\Gamma$  direction and EDCs of six  $Bi_{2-y}Cr_ySe_3$  films with y from 0 to 0.24 taken at room temperature, where the dashed lines roughly indicate the edges of bulk bands. Due to peak broadening

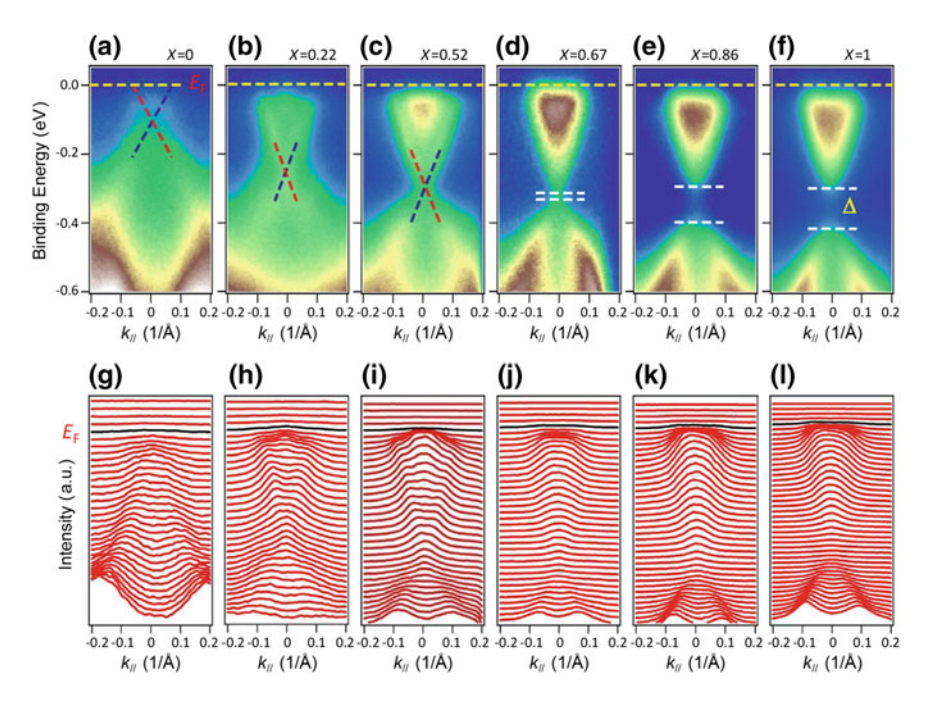


**Fig. 4.17** The ARPES band maps (**a**–**f**) and the momentum distribution curves (**g**–**l**) taken at 120 K along the K-Γ-K direction on the Bi<sub>1.78</sub>Cr<sub>0.22</sub>(Se<sub>x</sub>Te<sub>1-x</sub>)<sub>3</sub> films with Se concentration x = 0, 0.22, 0.52, 0.67, 0.86, and 1.0, respectively. The positions of the Fermi level ( $E_F$ ) are indicated by *yellow dashed lines* (**a**–**f**) and *black solid curves* (**g**–**l**). The *blue* and *red dashed lines* in (**a**–**c**) indicate the Dirac surface states with opposite spin polarities and they intersect at the Dirac point. *White dotted lines* in (**d**) to (**f**) represent the top of the valence band and the bottom of the conduction band, and Δ is the energy gap between them

induced by Cr doping, it is difficult to determine the exact size of bulk gap. Nevertheless, we still can tell that the size of the bulk gap at  $\Gamma$  point decreases with increasing Cr content in the range of  $0 \le y \le 0.13$ . At y = 0.13, the gap reaches a minimum value and it increases with Cr content for  $0.13 \le y \le 0.24$ . Meanwhile, the surface states can be resolved for  $y \le 0.13$  but totally vanish for  $y \ge 0.20$ , indicating the topologically trivial bulk band structure. Therefore, another topological QPT in  $Bi_{2-v}Cr_vSe_3$  films is also revealed through ARPES measurements.

For  $Bi_{2-y}Cr_yTe_3$  films, the ARPES measurements are shown in Fig. 4.19 with  $0 \le y \le 0.38$ . Here, the Fermi level is located in the bulk band so that the bulk conduction band cannot be clearly observed. In pure  $Bi_2Te_3$  (y = 0) film, the well-defined surface states with massless Dirac-like dispersion can be clearly observed, same as that shown in Fig. 3.4a. As the Cr dopants are introduced, the surface states exist for all the doping up to y = 0.23, which is similar to that in Fig. 4.17a. This contrasts strongly to the  $Bi_{2-y}Cr_ySe_3$  case, where the surface states totally vanish for  $y \ge 0.20$ . Remarkably, the DP moves upward relative to the bulk valence band as the Cr content is increased. This is a strong indication that a

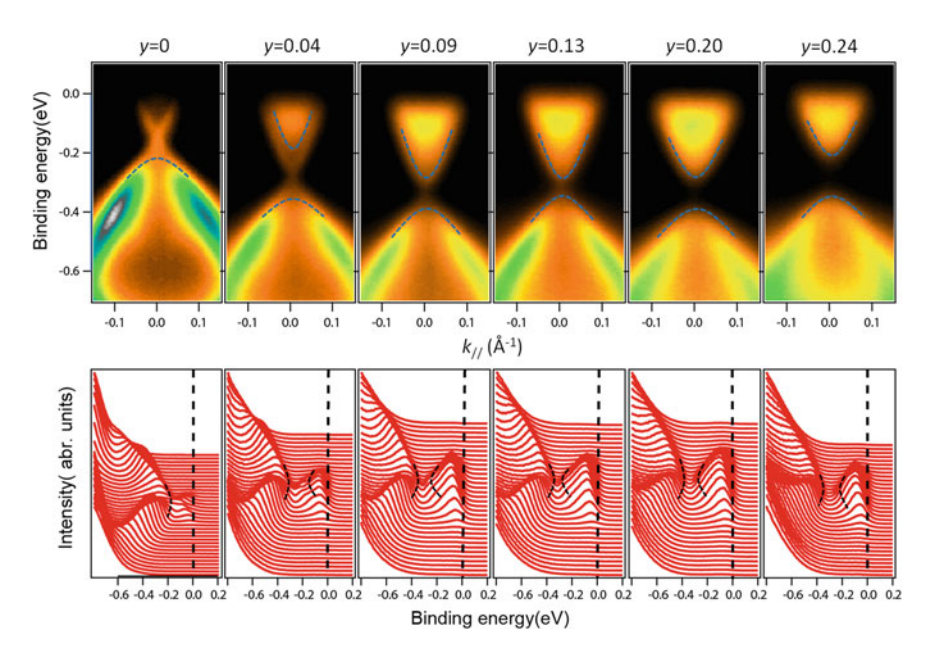


**Fig. 4.18** The ARPES band maps and the energy distribution curves (EDCs) taken at room temperature along the K-Γ-K direction on the  $Bi_{2-y}Cr_ySe_3$  films with Cr concentration y = 0, 0.04, 0.09, 0.13, 0.20, and 0.24, respectively

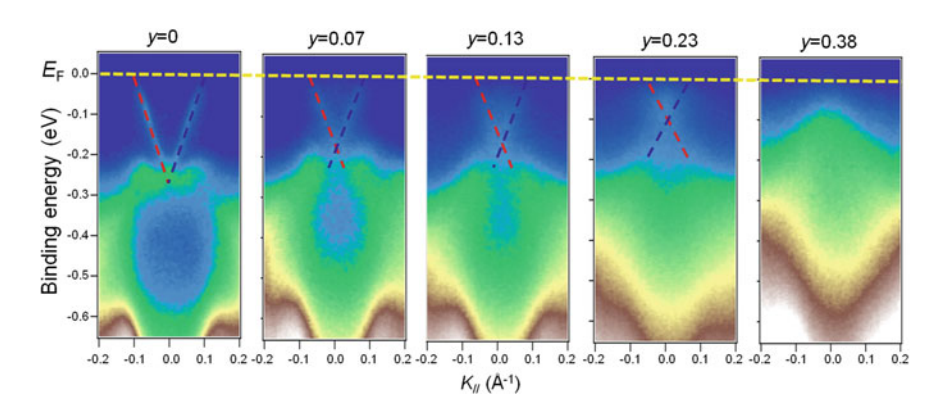


**Fig. 4.19** The ARPES band measurements taken at room temperature along the K-Γ-K direction on the Bi<sub>2-v</sub>Cr<sub>v</sub>Te<sub>3</sub> films with Cr concentration y = 0, 0.07, 0.13, 0.23, and 0.38, respectively

ferromagnetic topological insulator with the Fermi level both in the bulk and in the surface band gaps could be possibly achieved. Moreover, with further increase of y up to 0.38, the surface states totally disappear, which probably reveals the topologically QPT from non-trivial bulk band ( $y \le 0.23$ ) to a trivial insulator (y = 0.38) again.

## 4.7 Density Functional Theory Calculations

Density functional theory (DFT) is a quantum mechanical modeling method for investigating the electronic structure of solid-state systems. In many cases, the results of DFT calculations agree quite satisfactorily with experimental data, which makes it as one of the most popular and versatile calculation methods in condensed matter physics. In this section, the DFT calculations are reported, which firmly corroborate the topological QPT in the  $Bi_{2-\nu}Cr_{\nu}(Se_{\nu}Te_{1-\nu})_3$  films.

#### 4.7.1 Calculation Method

The DFT calculations are performed by using the Perdew–Burke–Ernzerhof (PBE) generalized gradient approximation [34] and the projector-augmented wave potential [35], as implemented in the Vienna ab initio simulation package [36]. The energy cutoff of the plane wave basis is 340 eV. The lattice constants of Cr-doped Bi<sub>2</sub>Se<sub>3</sub> (a[Bi<sub>2-y</sub>Cr<sub>y</sub>Se<sub>3</sub>]) and Bi<sub>2</sub>Te<sub>3</sub> (a[Bi<sub>2-y</sub>Cr<sub>y</sub>Te<sub>3</sub>])) are taken to be equal to the experimental values of pristine Bi<sub>2</sub>Se<sub>3</sub> and Bi<sub>2</sub>Te<sub>3</sub> [37]. The lattice constants of the Se/Te mixed phase (a[Cr<sub>0.25</sub>Bi<sub>1.75</sub>(Se<sub>x</sub>Te<sub>1-x</sub>)<sub>3</sub>]) are estimated by the interpolation: a [Cr<sub>0.25</sub>Bi<sub>1.75</sub>(Se<sub>x</sub>Te<sub>1-x</sub>)<sub>3</sub>] =  $x \cdot a$ [Bi<sub>2</sub>Se<sub>3</sub>] +  $(1 - x) \cdot a$ [Bi<sub>2</sub>Te<sub>3</sub>]. The internal coordinates are fully relaxed till the forces converge to a value of less than 0.01 eV/Å. The spin–orbit coupling (SOC) is included in the following self-consistent calculations of electronic structure [38]. In order to correctly describe the p-d hybridization, an on-site effective Coulomb interaction [39] of 4 eV is added to the 3d orbital of Cr atom [28]. A 2 × 2×1 hexagonal supercell and 9 × 9×1 Monkhorst–Pack k point sampling are used for band structure calculations.

## 4.7.2 Band Structures of Bi<sub>2-v</sub>Cr<sub>v</sub>Se<sub>3</sub> and Bi<sub>2-v</sub>Cr<sub>v</sub>Te<sub>3</sub>

Figure 4.20 displays the DFT-calculated band structures along the high-symmetry K- $\Gamma$  and  $\Gamma$ -M directions for Cr-doped Bi<sub>2</sub>Se<sub>3</sub> with a chemical formula Bi<sub>2-y</sub>Cr<sub>y</sub>Se<sub>3</sub>. The band structures of pure Bi<sub>2</sub>Se<sub>3</sub> agree very well with those reported previously [10]. At the  $\Gamma$  point, there is an inverted energy gap with an amplitude  $\Delta \sim 0.3$  eV. Increasing Cr content to y = 0.083 significantly reduces the gap amplitude because Cr has much smaller SOC strength than Bi. But the conduction and valence bands remain inverted in this sample, indicating a non-trivial bulk topology. At y = 0.167, interestingly, the conduction and valence bands touch each other, leading to a gap closing that indicates a topological phase transition. When Cr content is increased further to y = 0.25, the gap reopens with an amplitude  $\Delta \sim 0.2$  eV, but now the conduction and valence bands are not inverted anymore. A similar topological

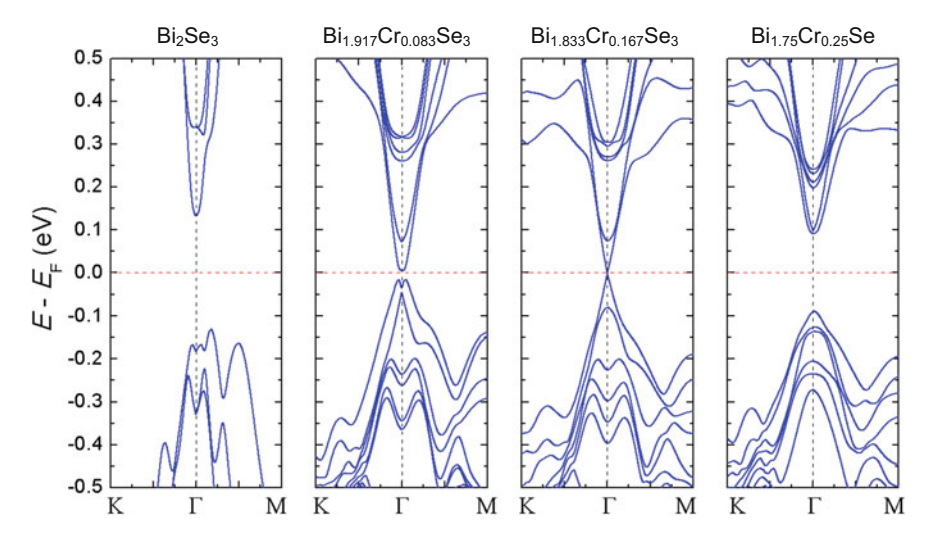


**Fig. 4.20** DFT-calculated bulk band structures of  $Bi_{2-y}Cr_ySe_3$  with different Cr contents. From *left* to *right* y = 0, 0.083, 0.167, and 0.25, respectively. The *red broken line* stands for the Fermi level

phase transition has been reported by altering the SOC strength in 3 QL of Cr- and Fe-doped Bi<sub>2</sub>Se<sub>3</sub> thin films [28].

In Fig. 4.21, we summarize the evolution of the bulk gap size measured by ARPES (Fig. 4.18) as well as the DFT-calculated gap size (Fig. 4.20). The good qualitative agreement between them is very remarkable and provides unambiguous support for the validity of the DFT calculation and the underlying physics of a topological QPT near  $y_c = 0.167$ .

Figure 4.22 shows the DFT-calculated band structures of Cr-doped  $Bi_2Te_3$ , which reveal a more complicated situation than that in Cr-doped  $Bi_2Se_3$ . The band structure of pure  $Bi_2Te_3$  also has an inverted energy gap at the  $\Gamma$  point that agrees well with the previous report [10]. With increasing y, however, the energy gap at the  $\Gamma$  point does not show the simple gap closing and reopening pattern. Instead, the gap is always present and its amplitude shows a rather complex variation with y. Nevertheless, these calculated band structures are still consistent with the ARPES measurements shown in Fig. 4.19. In these calculations, the Cr content can only take several discrete values and cannot vary continuously; therefore, we cannot judge directly if the band structure of  $Bi_{1.75}Cr_{0.25}Te_3$ —that is the most relevant sample to our experiments—is inverted or not.

In order to determine the topological nature of the bulk band in  $\mathrm{Bi}_{1.75}\mathrm{Cr}_{0.25}\mathrm{Te}_3$ , we calculate the band structures of this sample with different inter-QL coupling. By artificially increasing the inter-QL distance from the equilibrium value  $d_0$  (Fig. 4.23b), the coupling between the QLs can be tuned continuously from the real intermediate regime to the hypothetical weak coupling regime. This method provides a natural way to show the band inversion and has been used to identify that

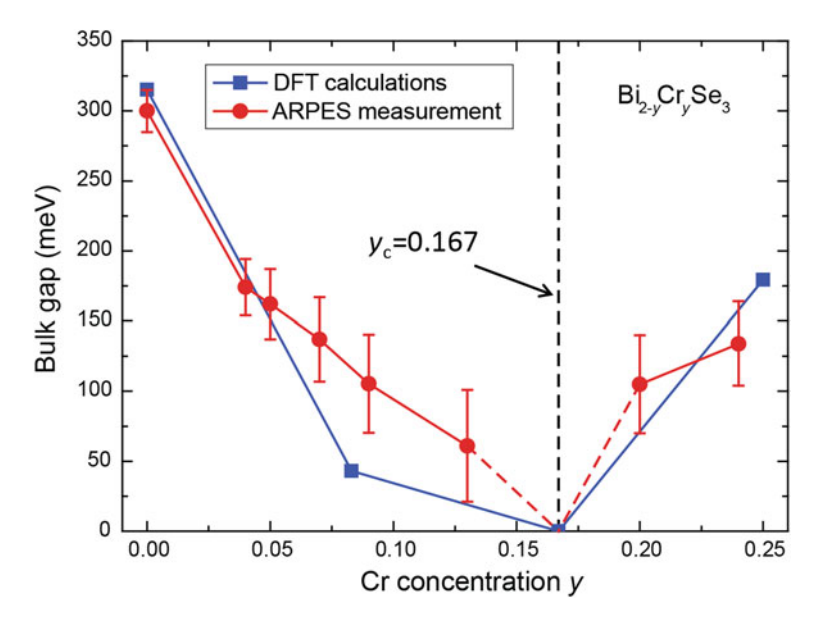


Fig. 4.21 The bulk gap evolution of  $Bi_{2-y}Cr_ySe_3$  obtained from the ARPES measurements and DFT calculations. The *red dash lines* represent the imaginary tendency of bulk gap, not real data

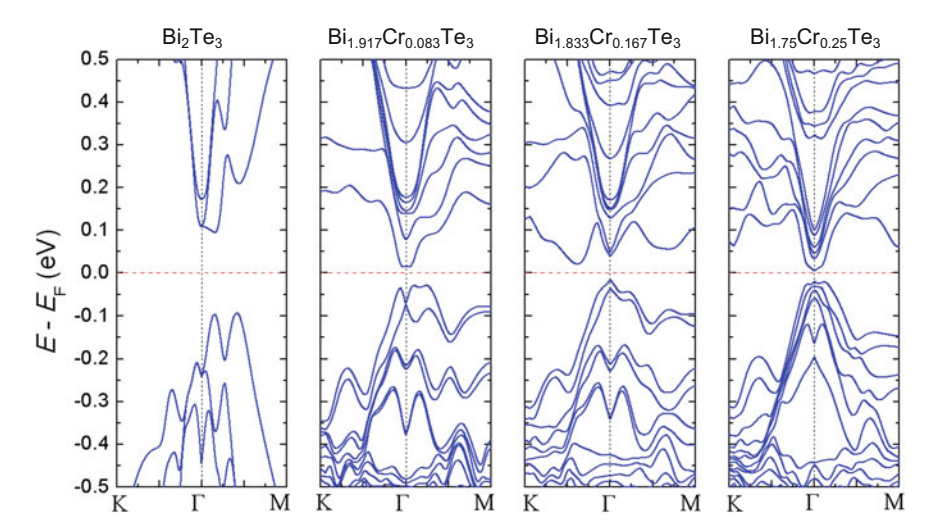
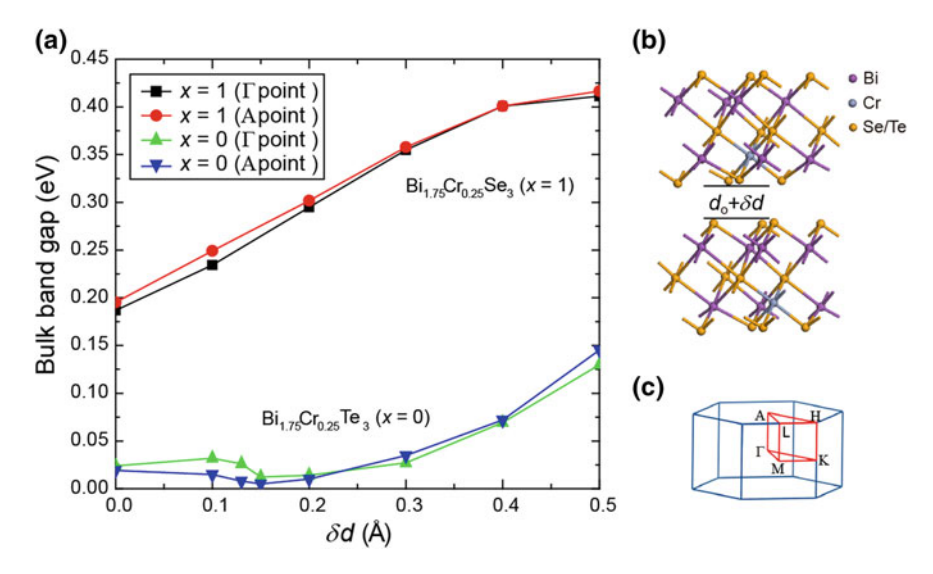


Fig. 4.22 DFT-calculated bulk band structures of  $Bi_{2-y}Cr_yTe_3$  with different Cr contents. From *left* to *right* y = 0, 0.083, 0.167, and 0.25, respectively

ultrathin Bi(111) film is in a topologically non-trivial case independent of film thickness [40]. Without the inter-QL coupling (inter-QL distance is infinite), the 3D bulk system is topologically trivial [41], because it can be viewed as a stack of 2D



**Fig. 4.23** a The band gaps of Bi<sub>1.75</sub>Cr<sub>0.25</sub>Te<sub>3</sub> and Bi<sub>1.75</sub>Cr<sub>0.25</sub>Se<sub>3</sub> at  $\Gamma$  and A points as a function of the increment of inter-QL distance  $\delta d$ . **b** The crystal structure (*side view*) of Bi<sub>1.75</sub>Cr<sub>0.25</sub>Te<sub>3</sub> or Bi<sub>1.75</sub>Cr<sub>0.25</sub>Se<sub>3</sub>. **c** The first Brillouin zone of the hexagonal lattice, indicating the  $\Gamma$  and A points

trivial insulator layers. Now, we start from the equilibrium inter-QL distance  $d_0$  and increase the distance to a quite large value. If the realistic system is in the inverted regime, with increasing  $\delta d$  a band gap closing and reopening process is expected. If the system with equilibrium inter-QL distance  $d_0$  is already a trivial insulator, on the other hand, the band gap should just increase monotonically.

As shown in Fig. 4.23a, when we continually increase the inter-QL distance, the band gaps of Bi<sub>1.75</sub>Cr<sub>0.25</sub>Te<sub>3</sub> at the  $\Gamma$  and A points decrease first and then increase with the increment of  $\delta d$  corresponding to a band inversion process. As discussed above, this is a strong indication that the bulk band structure of Bi<sub>1.75</sub>Cr<sub>0.25</sub>Te<sub>3</sub> is inverted and topologically non-trivial in the PM phase. In contrast, the band gaps of Bi<sub>1.75</sub>Cr<sub>0.25</sub>Se<sub>3</sub> at  $\Gamma$  and A points increase monotonically with increasing  $\delta d$ , consistent with the fact that it is a topologically trivial insulator. These conclusions are consistent with the ARPES results (Fig. 4.17) showing that Bi<sub>1.78</sub>Cr<sub>0.22</sub>Te<sub>3</sub> has well-defined topological surface states characteristic of a TI phase and the complete absence of topological surface states in Bi<sub>1.78</sub>Cr<sub>0.22</sub>Se<sub>3</sub>.

# 4.7.3 The Corroboration of Topological QPT in $Bi_{1.75}Cr_{0.25}(Se_xTe_{1-x})_3$

The signature of topological QPT in the bulk band structure is the existence of a gap closing point at the critical SOC strength. This can be seen clearly in the DFT

results on Cr-doped Bi<sub>2</sub>Se<sub>3</sub> shown in Figs. 4.20 and 4.21. The inverted energy gap with  $\Delta \sim 300$  meV in pristine Bi<sub>2</sub>Se<sub>3</sub> shrinks with increasing Cr doping and closes at  $y \sim 0.167$ . For y = 0.25, the gap reopens, but now the band structure becomes normal, indicative of a trivial band insulator. The origin of the topological QPT is quite straightforward. The Cr substitution of Bi not only introduces local moments, but also reduces the SOC strength. At sufficiently high Cr doping, the SOC is not strong enough to invert the bands, leading to a trivial bulk topology [28]. For Cr-doped Bi<sub>2</sub>Te<sub>3</sub>, on the contrary, our DFT calculations show that the bulk band remains inverted for Cr content up to y = 0.25 (Figs. 4.22 and 4.23). The more robust band inversion here is due to the larger SOC strength of Te than Se. To better simulate the experiments, we calculate the band structures of Bi<sub>1.75</sub>Cr<sub>0.25</sub>(Se<sub>x</sub>Te<sub>1-x</sub>)<sub>3</sub> with varied x. As shown in Fig. 4.24, indeed there is a transition from inverted to normal bands due to the reduced SOC strength with increasing Se/Te ratio. Figure 4.25 summarizes the calculated bulk gap at the  $\Gamma$  point, which clearly shows a topological QPT near  $x \sim 0.66$ , in excellent agreement with the experiments.

From DFT calculations, it is impossible to simulate the PM phase, so only the FM phase can be considered here. It is found that the Zeeman splitting of  $Bi_{1.75}Cr_{0.25}(Se_xTe_{1-x})_3$  induced by the ferromagnetic coupling is just dozens of meV. At x=0, the band structure has been inverted as discussed above, so the SOC strength to invert the bands should be larger than the band gap without SOC at  $\Gamma$  point (622 meV), which is larger by one order of magnitude than that of the Zeeman splitting. For  $Bi_{1.75}Cr_{0.25}(Se_xTe_{1-x})_3$ , although the SOC strength decreases with the increase of x, the magnitude of SOC is also in the same order with that of  $Bi_{1.75}Cr_{0.25}Te_3$ . Thus, the critical point ( $x_c=0.66$ ) from DFT calculation should be quite close to the realistic critical point of the topological QPT in the PM phase.

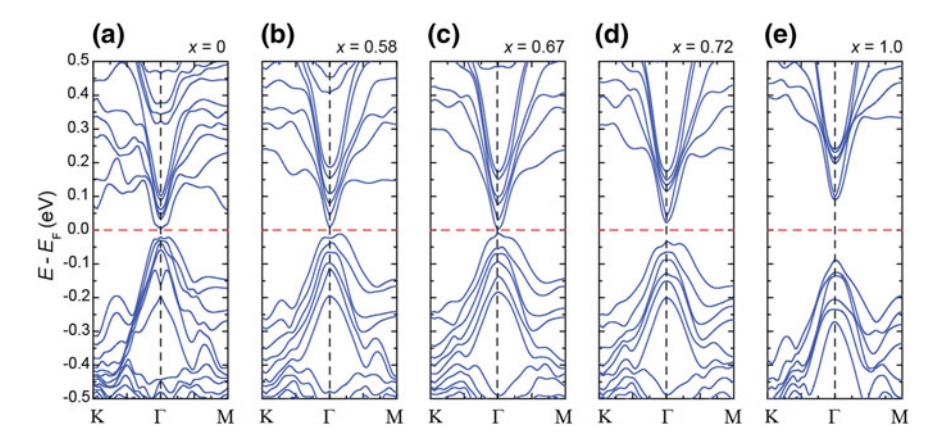
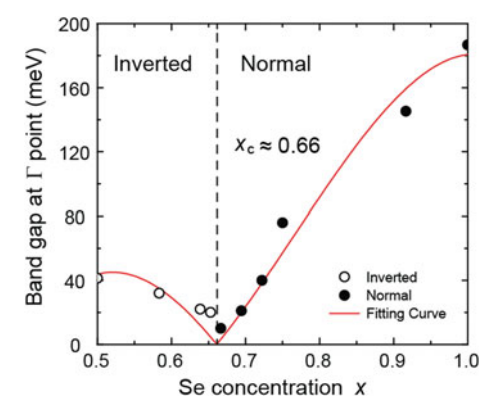


**Fig. 4.24** The bulk band structure of Bi<sub>1.75</sub>Cr<sub>0.25</sub>(Se<sub>x</sub>Te<sub>1-x</sub>)<sub>3</sub> calculated by the density functional theory with x = 0 (a),0.58 (b), 0.67 (c), 0.72 (d), and 1.0 (e), respectively. *Red dashed lines* indicate the positions of  $E_{\rm F}$ , and *black dashed lines* represent the locations of the Γ points

Fig. 4.25 The topological phase diagram. Starting from x = 0.5, the bulk band structure is inverted and the gap at the  $\Gamma$  point decreases with increasing x and closes at the critical point  $x_c = 0.66$ . Above that the gap reopens and increases with x, but the band structure becomes trivial



# **4.8** Relationship Between Topological QPT and Magnetic QPT

Now that the correlation between the magnetic and topological QPTs is firmly established, we turn to a more fundamental question: Which phase transition is the driving force and which one is the consequence? There are two pieces of evidence supporting the scenario that topology is the fundamental character that determines the magnetic ordering. Firstly, in the  $Bi_{1.78}Cr_{0.22}(Se_xTe_{1-x})_3$  samples studied here, the Cr content is fixed and only the Se/Te ratio is varied. This provides a knob for fine-tuning the SOC strength and hence the bulk band topology, but the magnetic property is not directly affected. Therefore, the magnetic QPT should be a secondary effect of the topological QPT. Secondly, the ARPES results show that even at high T when all the samples are in the PM state, the two regimes separated by the QCP already develop different topologies. The magnetic ground states form at low T following the preformed topological distinctions, where the FM phase results from the non-trivial  $Z_2$  topology and a transition to PM phase occurs when the bulk turns topologically trivial.

#### 4.9 Effective Four-Band Model Calculations

In this section, the magnetic properties of the TI thin films are calculated by the effective four-band model, which reveals a strong enhancement of the z direction spin susceptibility in the topologically non-trivial regime, thus in favor of FM ordering. Moreover, the sign change of the AHE at the QCP is also explicitly explained.

#### 4.9.1 The Spin Susceptibility in z Direction

The low-energy physics of Bi<sub>2</sub>Se<sub>3</sub> family materials can be described by the effective four-band model [10]

$$H_0' = \epsilon \left(\vec{k}\right) + \mathcal{M}\left(\vec{k}\right)\Gamma_5 + B_0\Gamma_4 k_z + A_0 \left(k_y \Gamma_1 - k_x \Gamma_2\right), \tag{4.2}$$

where  $\epsilon\left(\vec{k}\right)=C_0+C_1k_z^2+C_2k_\parallel^2$ , and  $\mathcal{M}\left(\vec{k}\right)=M_0+M_1k_z^2+M_2k_\parallel^2+\eta k^4$ , and  $k_\parallel^2=k_x^2+k_y^2$ . Here,  $C_0$ ,  $C_1$ ,  $C_2$ ,  $M_0$ ,  $M_1$ ,  $M_2$ ,  $A_0$ ,  $B_0$ , and  $\eta$  are all parameters and we add a small  $\eta k^4$  term in order to give a correct high energy cutoff of the effective model. This Hamiltonian is the same as that presented in Eq. (1.9) after performing a unitary transformation. The basis of the above Hamiltonian is given by  $|P1_-^+,1/2\rangle$ ,  $|P2_+^-,1/2\rangle$ ,  $|P1_-^+,1/2\rangle$ , and  $|P2_+^-,1/2\rangle$  denoted as  $|+,\uparrow,\rangle$   $|-,\uparrow,\rangle$   $|+,\downarrow\rangle$ , and  $|-,\downarrow\rangle$  for short [42]. The  $\Gamma$  matrices are defined as  $\Gamma_1=\sigma_x\tau_x$ ,  $\Gamma_2=\sigma_y\tau_x$ ,  $\Gamma_3=\sigma_z\tau_x$ ,  $\Gamma_4=\tau_y$ ,  $\Gamma_5=\tau_z$  and  $\Gamma_{ab}=[\Gamma_a,\Gamma_b]/2i$   $(a,b=1\dots 5)$  for other ten  $\Gamma$  matrices. Here, the Pauli matrix  $\sigma$  denotes spin and  $\tau$  denotes orbital.

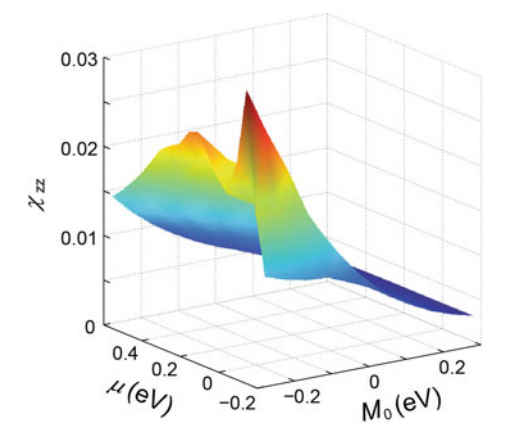
We consider the above Hamiltonian equation Eq. (4.2) in a thin film configuration with the thickness d=8 nm and solve the eigen equation  $H_0\Psi(z)=E\Psi(z)$  numerically [43] with the open boundary condition  $\Psi(0)=\Psi(d)=0$ . With the eigen energies and eigen states, we can calculate the electron spin susceptibility in the linear response regime with the formula

$$\chi_{zz}(\omega) = \int \frac{d^2k}{(2\pi)^2} \sum_{\alpha\beta} Tr(S_z P_\alpha S_z P_\beta) \frac{n_F(E_\beta) - n_F(E_\alpha)}{E_\beta - E_\alpha + \hbar\omega + i\eta}, \tag{4.3}$$

where  $S_z = \sigma_z/2$  is the spin operator,  $n_{\rm F}$  is the Fermi distribution function,  $E_\alpha$  is the  $\alpha$ th eigen energy, and the corresponding eigen states  $\Psi_\alpha(z)$  determine the projection operator  $P_\alpha = |\Psi_\alpha\rangle \langle \Psi_\alpha|$ . In this calculation, we do not have any magnetization, which corresponds to the PM phase, and the parameters are taken as  $C_0 = 0$ ,  $C_1 = 5.74 \text{ eV} \cdot \text{Å}^2$ ,  $C_2 = 30.4 \text{ eV} \cdot \text{Å}^2$ ,  $M_1 = 6.86 \text{ eV} \cdot \text{Å}^2$ ,  $M_2 = 44.5 \text{ eV} \cdot \text{Å}^2$ ,  $A_0 = 3.33 \text{ eV} \cdot \text{Å}$ ,  $B_0 = 2.26 \text{ eV} \cdot \text{Å}$ , and  $\eta = 50 \text{ eV} \cdot \text{Å}^4$ .

Figure 4.26 displays the calculated  $\chi_{zz}$  for different chemical potential ( $\mu$ ) and the mass term ( $M_0$ ). It is evident that for the normal (topologically trivial) regime with  $M_0 > 0$ ,  $\chi_{zz}$  reduces quickly when the band gap increases, whereas for the inverted (topologically non-trivial) regime with  $M_0 < 0$ ,  $\chi_{zz}$  always keeps a large value when  $\mu$  is around the gap. The reason for the large spin susceptibility in the non-trivial phase is the van Vleck mechanism proposed in reference [6], which explicitly states that the second-order matrix element is significantly enhanced when the band becomes inverted. The topologically non-trivial phase thus strongly favors a FM ordering, which naturally explains the topology-driven magnetic QPT discovered in the experiments. The van Vleck mechanism is further supported by the magnetization measurements (Fig. 4.15), which shows that the ferromagnetism occurs in

Fig. 4.26 The calculated spin susceptibility of the four-band model for different  $\mu$  and  $M_0$  in 8 QL thick films showing the significantly enhanced spin susceptibility in the topologically non-trivial regime



the bulk rather than being a surface FM order mediated by the RKKY mechanism [14, 15]. Furthermore, the out-of-plane magnetic anisotropy revealed by the field angle dependence of MR (Fig. 4.13) is also consistent with the van Vleck-type FM order in TIs [6].

## 4.9.2 Sign Change of the AHE at QCP

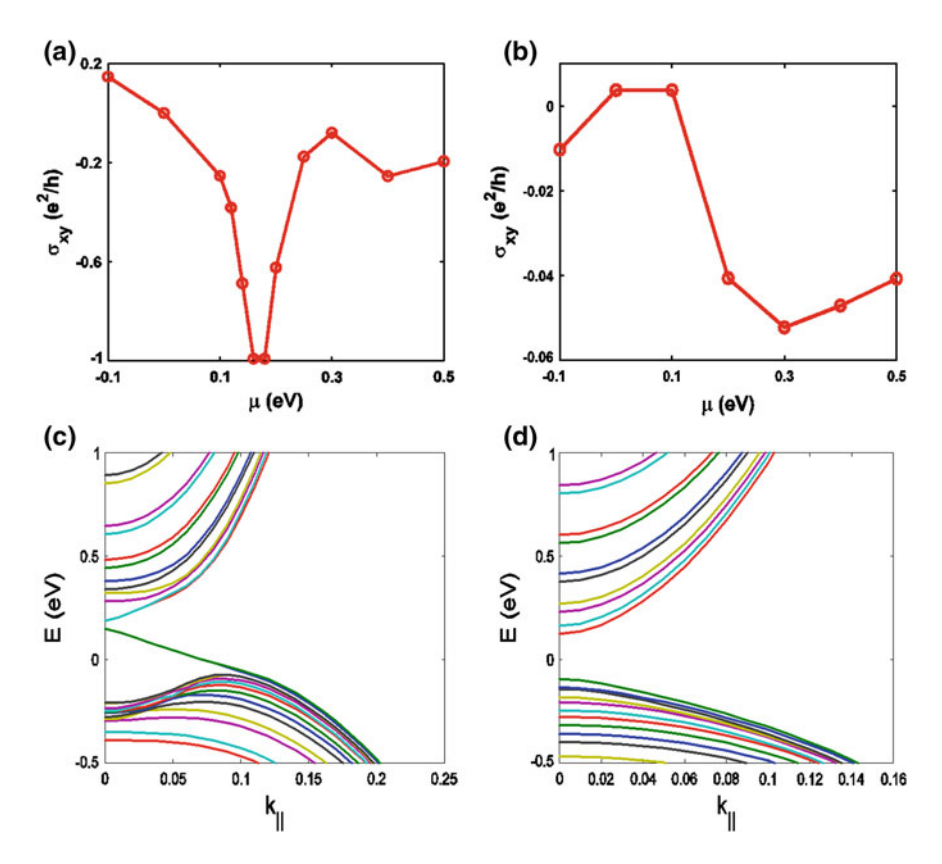
Next, we consider the anomalous Hall conductivity ( $\sigma_{xy}$ ) of the TI thin film. In order to have a nonzero  $\sigma_{xy}$ , we need to break time-reversal (TR) symmetry, which can be achieved by introducing Zeeman type of spin splitting due to the magnetization along z direction. According to the symmetry property of  $\Gamma$  matrices (e.g., Table 3 in reference [42]), two additional terms are allowed for the effective Hamiltonian

$$H_{\rm Z} = G_{z1}\Gamma_{12} + G_{z2}\Gamma_{34},\tag{4.4}$$

where  $G_{z1}$  and  $G_{z2}$  are the Zeeman splitting terms from the exchange coupling between the electrons and magnetic impurities. Similar to the calculation of  $\chi_{zz}$ , we solve the eigen problem of the Hamiltonian  $H_0 + H_Z$  and use the eigen energy and eigen wave function to obtain  $\sigma_{xy}$  with the Kubo formula

$$\sigma_{xy} = -\frac{i.e.^2}{\hbar} \int \frac{d^2k}{(2\pi)^2} \sum_{\alpha\beta} \frac{n_F(\epsilon_{\beta}) - n_F(\epsilon_{\alpha})}{(\epsilon_{\beta} - \epsilon_{\alpha})^2} Tr\left(\frac{\partial H}{\partial k_x} P_{\alpha} \frac{\partial H}{\partial k_y} P_{\beta}\right). \tag{4.5}$$

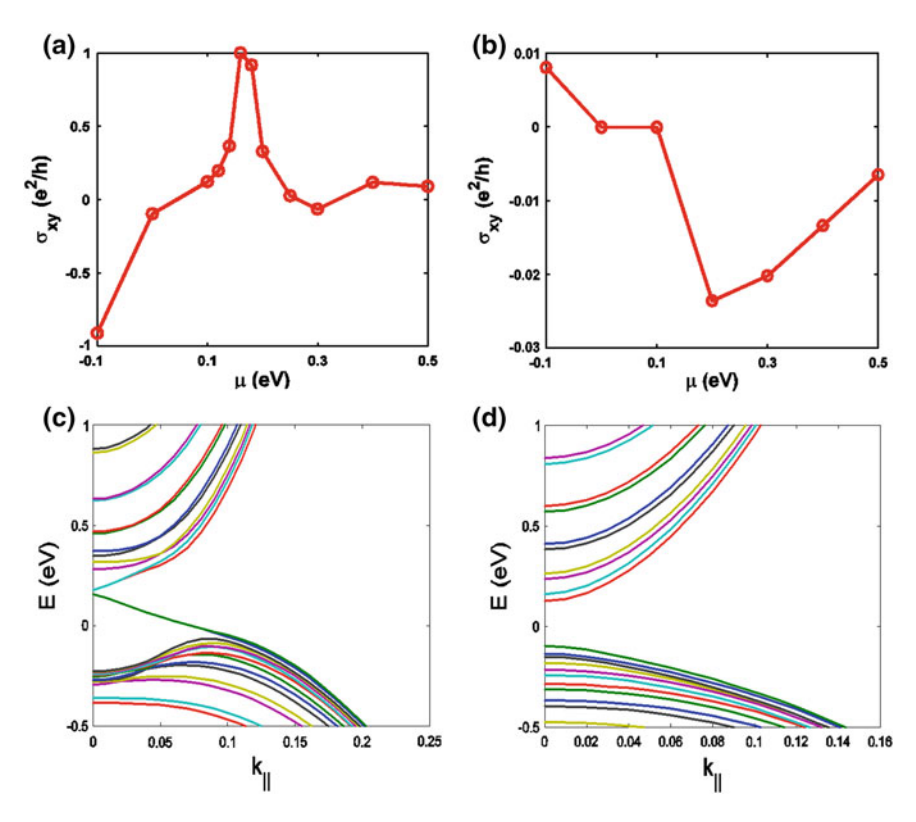
The  $\sigma_{xy}$  as a function of chemical potential ( $\mu$ ) for different parameters is shown in Figs. 4.27 and 4.28, where we only change  $G_{z1}$  and  $G_{z2}$  and keep all the other parameters the same as that used in the calculation of  $\chi_{zz}$ . For nonzero  $G_{z1}$  term, we find integer  $\sigma_{xy}$  (Fig. 4.27a) when the chemical potential  $\mu$  lies in the surface state gap (at the energy of around 0.16 eV in Fig. 4.27c). However, in the n-doped



**Fig. 4.27** The  $\sigma_{xy}$  of the four-band model in the inverted regime **a** with  $M_0 = -0.28$  eV,  $G_{z1} = 0.02$  eV, and  $G_{z2} = 0$  and the normal regime **b** with  $M_0 = 0.1$  eV,  $G_{z1} = 0.02$  eV, and  $G_{z2} = 0$ . **c** and **d** are the sub-band dispersion corresponding to (**a**) and (**b**)

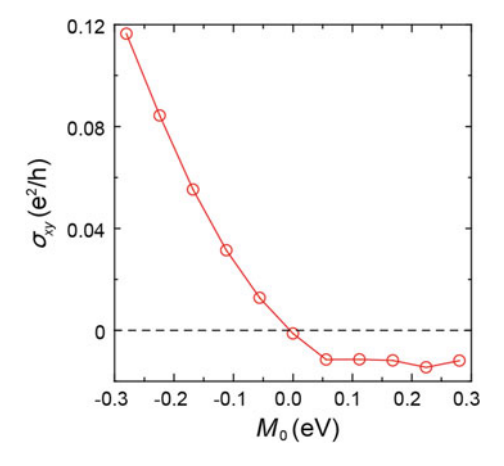
regime that is more relevant to our experiments, we always find a negative sign of  $\sigma_{xy}$  with  $G_{z1}=0.02$  eV and  $G_{z2}=0$  as shown in Fig. 4.27a and b. For nonzero  $G_{z2}$  term, we can also see integer  $\sigma_{xy}$  when  $\mu$  is in the surface gap. Interestingly, now in the n-doped regime, the sign of  $\sigma_{xy}$  is reversed between the normal and inverted regimes with  $G_{z2}=0.02$  eV and  $G_{z1}=0$  as shown in Fig. 4.28.

Figure 4.29 summarizes the  $\sigma_{xy}$  value as a function of  $M_0$  with fixed chemical potential ( $\mu = 0.4$  eV), which clearly uncovers a sign change when the band gap is reversed, in good agreement with the experimental observation. The close correlation between the AHE sign change and topological QPT suggests that it can be used as a transport fingerprint for the bulk topology. This is not unexpected given the growing recognition of the topological nature of the intrinsic AHE in recent years [44, 45]. The extrinsic AHE, which may be present in realistic materials, is ignored here because it typically dominates in highly metallic materials, whereas the disordered TI films studied here are poorly conductive [29].



**Fig. 4.28** The  $\sigma_{xy}$  of the four-band model in the inverted regime **a** with  $M_0 = -0.28$  eV,  $G_{z1} = 0$ , and  $G_{z2} = 0.02$  eV and the normal regime **b** with  $M_0 = 0.1$  eV,  $G_{z1} = 0$ , and  $G_{z2} = 0.02$  eV. **c** and **d** are the sub-band dispersion corresponding to (**a**) and (**b**)

**Fig. 4.29** A summary of the anomalous Hall conductivity  $\sigma_{xy}$  as a function of  $M_0$  with  $G_{z1}=0$  and  $G_{z2}=0.02$  eV at fixed  $\mu=0.4$  eV showing the sign reversal of  $\sigma_{xy}$  across the topological QPT



## 4.9.3 Physical Meaning and Estimation of G<sub>z1</sub> and G<sub>z2</sub>

From the low-energy effective Hamiltonian, it is found that for topologically non-trivial case, the spin splitting of the conduction band is  $2|G_{z1}-G_{z2}|$ , which can be expressed as  $|\Lambda_+,1/2\rangle=\mu_+^{\Lambda}|\Lambda,\,p_z^{\rm Se},\uparrow\rangle+v_+^{\Lambda}|\Lambda,\,p_z^{\rm Se},\downarrow\rangle$  and  $|\Lambda_+,1/2\rangle=(\mu_+^{\Lambda})^*$   $|\Lambda,\,p_z^{\rm Se},\uparrow\rangle+(v_+^{\Lambda})^*|\Lambda,\,p_+^{\rm Se},\downarrow\rangle$ . For the valance band, the splitting is  $2|G_{z1}+G_{z2}|$ , which is expressed as  $|\Lambda_-,1/2=\mu_-^{\Lambda}|\Lambda,\,p_z^{\rm Bi},\uparrow\rangle+v_-^{\Lambda}|\Lambda,\,p_+^{\rm Bi},\downarrow\rangle$  and  $|\Lambda_-,1/2\rangle=(\mu_-^{\Lambda})^*$   $|\Lambda,\,p_z^{\rm Bi},\uparrow\rangle+(v_-^{\Lambda})^*|\Lambda,\,p_+^{\rm Bi},\downarrow\rangle$ , where  $\mu_+^{\Lambda}$  and  $\nu_+^{\Lambda}$  are the normalized coefficients from DFT calculation,  $\Lambda$  stands for  $P1^+$  or  $P2^-$ , and  $p_+^{\rm Bi(Se)}$  means  $1/\sqrt{2}(p_x^{\rm Bi(Se)}+ip_y^{\rm Bi(Se)})$ . Therefore, if we obtain the spin splitting of  $p_x,\,p_y$ , and  $p_z$  orbitals from DFT calculation directly, we can estimate  $G_{z1}$  and  $G_{z2}$ .

Following this idea, we treat Bi<sub>1.917</sub>Cr<sub>0.083</sub>Se<sub>3</sub> as a prototype to estimate these parameters. Toward this structure, conduction band minimum and valence band maximum at the  $\Gamma$  point are mainly contributed by the  $p_z$  orbital of Se and Bi atoms; the contribution from Cr atom can be ignored. Because spin splitting is directly related to magnetic doping, the splitting of Bi<sub>1.75</sub>Cr<sub>0.25</sub>Se<sub>3</sub> is about three times of that in Bi<sub>1,917</sub>Cr<sub>0.083</sub>Se<sub>3</sub>. From DFT calculation without SOC, it is found that spin splitting of  $p_z$  orbital of Se and Bi atoms is about 48 and 8 meV, respectively. The splitting of the  $p_x$  and  $p_y$  orbitals of Se atom is about 25 meV. For intrinsic Bi<sub>2</sub>Se<sub>3</sub> with SOC, it is found that  $(\mu_+^{\Lambda})^2 = 00.5393, (v_+^{\Lambda})^2 = 00.460, (\mu_-^{\Lambda})^2 = 00.9844$  and  $(v_-^{\Lambda})^2=00.0156$ . Since  $(v_-^{\Lambda})^2\approx 0$ , the  $p_x$  and  $p_y$  orbitals of Bi atom are not considered here. Based on the above argument, the spin splitting for the conduction band is around 14 meV, and for the valence band, it is around 8 meV. This will lead to an estimate of  $G_{z1}$  and  $G_{z2}$  to be about 2 and 6 meV for Bi<sub>1.917</sub>Cr<sub>0.083</sub>Se<sub>3</sub>. In this case,  $G_{z1}$  and  $G_{z2}$  for  $Bi_{1.75}Cr_{0.25}Se_3$  are about 6 and 18 meV, respectively. Although the estimate here is quite rough, we believe the order of magnitude of  $G_{z1}$ and  $G_{72}$  is reliable.

#### 4.10 The van Vleck Mechanism in TIs

In the presence of a uniform magnetic field (**H**), the total kinetic energy operator of an ion (or atom) is replaced by [46]

$$\widetilde{T} = \frac{1}{2m} \sum_{i} \left[ \mathbf{P}_{i} + \frac{e}{c} \mathbf{A}(\mathbf{r}_{i}) \right]^{2} = \frac{1}{2m} \sum_{i} \left( \mathbf{P}_{i} - \frac{e}{2c} \mathbf{r}_{i} \times \mathbf{H} \right)^{2}.$$
(4.6)

Here, **A** is the magnetic vector potential and  $\mathbf{H} = \nabla \times \mathbf{A}$ . Then,  $\widetilde{T}$  can be expanded to give

$$\widetilde{T} = \widetilde{T}_0 + \mu_B \mathbf{L} \cdot \mathbf{H} + \frac{e^2}{8mc^2} H^2 \sum_i (x_i^2 + y_i^2),$$
 (4.7)

where  $\mu_B$  is Bohr magneton,  $\widetilde{T}_0$  is the original kinetic energy operator without magnetic field, and  $\mathbf{L}$  is the total orbital angular momentum. Combined with the Zeeman term, the total Hamiltonian is modified by

$$\Delta H = \mu_B(\mathbf{L} + g_0 \mathbf{S}) \cdot \mathbf{H} + \frac{e^2}{8mc^2} H^2 \sum_i (x_i^2 + y_i^2), \tag{4.8}$$

To compute the susceptibility, one must retain terms up to the second order in **H** and use the second-order perturbation theory:

$$\Delta E_n = \mu_B \mathbf{H} \cdot \langle n | \mathbf{L} + g_0 \mathbf{S} | n \rangle + \sum_{n' \neq n} \frac{|\langle n | \mu_B \mathbf{H} \cdot (\mathbf{L} + g_0 \mathbf{S}) | n' \rangle|^2}{E_n - E'_n} + \frac{e^2}{8mc^2} H^2 \langle n | \sum_i \left( x_i^2 + y_i^2 \right) | n \rangle,$$
(4.9)

where  $E_n$  and  $|n\rangle$  are the eigen energy and eigen state of an individual ion without any magnetic field. The second term in Eq. (4.9) is the origin of the van Vleck paramagnetism. Therefore, for an insulator that contains N/V such ions, the van Vleck susceptibility  $\chi_{zz}$  (in z direction) of the ground state can be expressed as follows:

$$\chi_{zz} = -\frac{N}{V} \frac{\partial^2 \Delta E_0}{\partial H^2} = 2\mu_B^2 \frac{N}{V} \sum_n \frac{|\langle 0 | (L_z + g_0 S_z) | n \rangle|^2}{E_n - E_0}.$$
 (4.10)

In a band insulator, such as the Bi<sub>2</sub>Se<sub>3</sub> family compound, one can rewrite the van Vleck spin susceptibility in the form of Bloch wave functions [6]:

$$\chi_{zz} = 4 \,\mu_B^2 \frac{N}{V} \sum_{E_{nk} < \mu: E_{mk} > \mu} \frac{\langle nk | S_z | mk \rangle \langle mk | S_z | nk \rangle}{E_{mk} - E_{nk}}, \tag{4.11}$$

where  $\mu$  is the Fermi energy and  $|mk\rangle$  and  $|nk\rangle$  are the Bloch functions in conduction and valence bands, respectively. Actually, this formula is just a simple expression as that shown in Eq. (4.3). Here,  $L_z$  term is neglected, because around  $\Gamma$  point the conduction and valence bands are mainly composed of the  $p_z$  orbitals of Bi and Se atoms.

In traditional semiconductors, the van Vleck paramagnetism is considerably small comparing with other mechanisms. However, in Bi<sub>2</sub>Se<sub>3</sub> family compounds, it is strongly enhanced due to the sizable matrix elements  $\langle nk|S_z|mk\rangle$ , which arise from the mixing of the conduction and valence bands induced by the spin operator

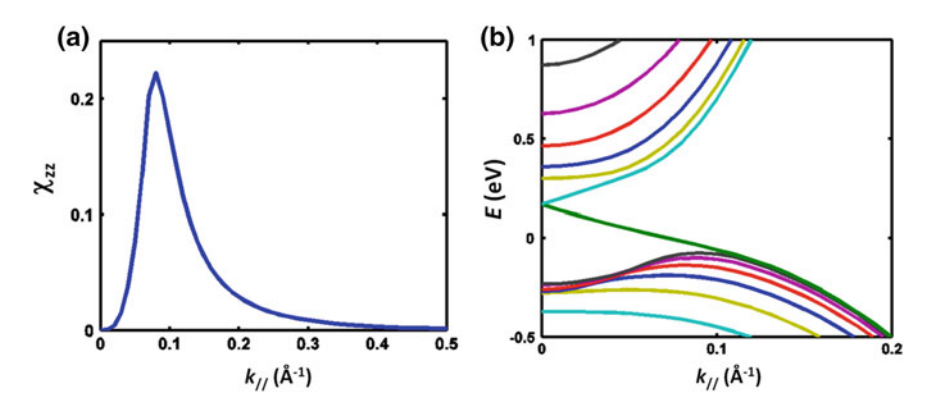


Fig. 4.30 a The van Vleck spin susceptibility  $\chi_{zz}$  shows a maximum value at  $k \sim 0.1 \text{ Å}^{-1}$ . b The corresponding sub-band dispersions

in the presence of SOC. Within the four-band model, this matrix element reaches the maximum when the condition  $\mathcal{M}(\vec{k})$  in the Hamiltonian equation Eq. (4.2) equals zero, which can only be satisfied in the inverted regime where  $M_0$  and  $M_{1,2}$  have opposite signs. In other words, for the normal regime,  $M_0$  and  $M_{1,2}$  have the same sign, and  $\mathcal{M}(\vec{k})$  can never reach zero. Thus, the maximum value of this matrix element cannot be reached and  $\chi_{zz}$  is less pronounced compared to the system with band inversion.

In order to show this more explicitly in the present quantum well system, we make a plot of the momentum k dependence of spin susceptibility by calculating Eq. (4.3) under four-band model without taking the momentum integral. As shown in Fig. 4.30a, the maximum of spin susceptibility occurs near  $k \sim 0.1$  Å<sup>-1</sup>. From the energy dispersion shown in Fig. 4.30b, we can see that the maximum of the valence band is not at k = 0, but at  $k \sim 0.1$  Å<sup>-1</sup>. This hump structure exactly indicates that  $\mathcal{M}(\vec{k})$  is minimized around  $k \sim 0.1$  Å<sup>-1</sup>. Another way to understand the maximized  $\chi_{zz}$  at  $k \sim 0.1$  Å<sup>-1</sup> is as follows: At this point, the conduction or valence band is composed of p orbitals from both Bi atoms and Se atoms. Thus, the overlap between the Bloch wave functions  $|mk\rangle$  and  $|nk\rangle$  is greatly enhanced compared with other momentums, where the conduction and valence bands consist of the p orbitals from different kinds of atoms.

#### 4.11 Conclusion

The transport and ARPES measurements, in concert with the first principle and effective theory calculations, reveal a coherent picture regarding the phases and phase transitions in Cr-doped  $Bi_2(Se_xTe_{1-x})_3$  TIs. We demonstrate that the magnetic

4.11 Conclusion 85

ordering is determined by the bulk band topology, which can be delicately tuned by the SOC strength by varying the Se/Te ratio. The topologically non-trivial FM states with tunable magnetic properties provide an ideal platform for realizing the exotic magnetoelectric effects proposed by theory. The topology-driven magnetic QPT may also inspire new ideas for topological magnetic phenomena and spintronic applications in TIs with broken TRS. We note that despite the excellent agreement between this picture and the observed phenomena, we cannot completely rule out all other possibilities for the disappearance of FM ordering across the topological QPT. For example, the ARPES results (Fig. 4.17) show that the bulk carrier density also varies with Se content, which may change an itinerant-driven FM mechanism.

#### References

- 1. Zhang J, Chang C-Z, Tang P, et al. Topology-driven magnetic quantum phase transition in topological insulators. Science. 2013;339:1582–6.
- 2. Moore JE. The birth of topological insulators. Nature. 2010;464:194-8.
- 3. Hasan MZ, Kane CL. Colloquium: topological insulators. Rev Mod Phys. 2010;82:3045-67.
- Qi X-L, Zhang S-C. The quantum spin Hall effect and topological insulators. Phys Today. 2010:63:33–8.
- Qi XL, Li R, Zang J, et al. Inducing a magnetic monopole with topological surface states. Science. 2009;323:1184–7.
- 6. Yu R, Zhang W, Zhang HJ, et al. Quantized anomalous Hall effect in magnetic topological insulators. Science. 2010;329:61–4.
- Nomura K, Nagaosa N. Surface-quantized anomalous Hall current and the magnetoelectric effect in magnetically disordered topological insulators. Phys Rev Lett. 2011;106:166802.
- 8. Tse WK, MacDonald AH. Giant magneto-optical Kerr effect and universal Faraday effect in thin-film topological insulators. Phys Rev Lett. 2010;105:057401.
- 9. Garate I, Franz M. Inverse spin-galvanic effect in the interface between a topological insulator and a ferromagnet. Phys Rev Lett. 2010;104:146802.
- 10. Zhang H, Liu C-X, Qi X-L, et al. Topological insulators in Bi<sub>2</sub>Se<sub>3</sub>, Bi<sub>2</sub>Te<sub>3</sub> and Sb<sub>2</sub>Te<sub>3</sub> with a single Dirac cone on the surface. Nat Phys. 2009;5:438–42.
- 11. Xia Y, Qian D, Hsieh D, et al. Observation of a large-gap topological-insulator class with a single Dirac cone on the surface. Nat Phys. 2009;5:398–402.
- 12. Chen YL, Analytis JG, Chu J-H, et al. Experimental realization of a three-dimensional topological insulator, Bi<sub>2</sub>Te<sub>3</sub>. Science. 2009;325:178–81.
- 13. Chen YL, Chu J-H, Analytis JG, et al. Massive Dirac fermion on the surface of a magnetically doped topological insulator. Science. 2010;329:659–62.
- 14. Liu Q, Liu C-X, Xu C, et al. Magnetic impurities on the surface of a topological insulator. Phys Rev Lett. 2009;102:156603.
- 15. Rosenberg G, Franz M. Surface magnetic ordering in topological insulators with bulk magnetic dopants. Phys Rev B. 2012;85:195119.
- 16. Wray LA, Xu S-Y, Xia Y, et al. A topological insulator surface under strong Coulomb, magnetic and disorder perturbations. Nat Phys. 2011;7:32–7.
- 17. Xu S-Y, Neupane M, Liu C, et al. Hedgehog spin texture and Berry's phase tuning in a magnetic topological insulator. Nat Phys. 2012;8:616–22.
- 18. Okada Y, Dhital C, Zhou W, et al. Direct observation of broken time-reversal symmetry on the surface of a magnetically doped topological insulator. Phys Rev Lett. 2011;106:206805.

- 19. Beidenkopf H, Roushan P, Seo J, et al. Spatial fluctuations of helical Dirac fermions on the surface of topological insulators. Nat Phys. 2011;7:939–43.
- 20. Hor YS, Roushan P, Beidenkopf H, et al. Development of ferromagnetism in the doped topological insulator  $Bi_{2-x}Mn_xTe_3$ . Phys Rev B. 2010;81:195203.
- 21. Kulbachinskii VA, Kaminskii AY, Kindo K, et al. Ferromagnetism in new diluted magnetic semiconductor Bi<sub>2-x</sub>Fe<sub>x</sub>Te<sub>3</sub>. Phys B. 2002;311:292–7.
- 22. Checkelsky JG, Ye J, Onose Y, et al. Dirac-fermion-mediated ferromagnetism in a topological insulator. Nat Phys. 2012;8:729–33.
- 23. Song YR, Yang F, Yao M-Y, et al. Large magnetic moment of gadolinium substituted topological insulator: Bi<sub>1.98</sub>Gd<sub>0.02</sub>Se<sub>3</sub>. Appl Phys Lett. 2012;100:242403.
- 24. Zhang D, Richardella A, Rench DW, et al. Interplay between ferromagnetism, surface states, and quantum corrections in a magnetically doped topological insulator. Phys Rev B. 2012;86:205127.
- 25. Ji H, Allred JM, Ni N, et al. Bulk intergrowth of a topological insulator with a room-temperature ferromagnet. Phys Rev B, 2012;85:165313.
- 26. Haazen PPJ, Laloe JB, Nummy TJ, et al. Ferromagnetism in thin-film Cr-doped topological insulator Bi<sub>2</sub>Se<sub>3</sub>. Appl Phys Lett. 2012;100:082403–4.
- 27. Zhang Y, He K, Chang C-Z, et al. Crossover of the three-dimensional topological insulator Bi<sub>2</sub>Se<sub>3</sub> to the two-dimensional limit. Nat Phys. 2010;6:584–8.
- 28. Jin H, Im J, Freeman AJ. Topological and magnetic phase transitions in Bi<sub>2</sub>Se<sub>3</sub> thin films with magnetic impurities. Phys Rev B. 2011;84:134408.
- Nagaosa N, Sinova J, Onoda S, et al. Anomalous Hall effect. Rev Mod Phys. 2010;82:1539–92.
- 30. He H-T, Wang G, Zhang T, et al. Impurity effect on weak antilocalization in the topological insulator Bi<sub>2</sub>Te<sub>3</sub>. Phys Rev Lett. 2011;106:166805.
- 31. Liu M, Zhang J, Chang C-Z, et al. Crossover between weak antilocalization and weak localization in a magnetically doped topological insulator. Phys Rev Lett. 2012;108:036805.
- 32. Xu S-Y, Xia Y, Wray LA, et al. Topological phase transition and texture inversion in a tunable topological insulator. Science. 2011;332:560–4.
- 33. Sato T, Segawa K, Kosaka K, et al. Unexpected mass acquisition of Dirac fermions at the quantum phase transition of a topological insulator. Nat Phys. 2011;7:840–4.
- 34. Perdew JP, Burke K, Ernzerhof M. Generalized gradient approximation made simple. Phys Rev Lett. 1996;77:3865–8.
- 35. Blöchl PE. Projector augmented-wave method. Phys Rev B. 1994;50:17953–79.
- 36. Kresse G, Furthmüller J. Efficient iterative schemes for ab initio total-energy calculations using a plane-wave basis set. Phys Rev B. 1996;54:11169–86.
- 37. Wyckoff RWG. Crystal structures, vol. 2. New York: Wiley; 1964.
- 38. Hobbs D, Kresse G, Hafner J. Fully unconstrained noncollinear magnetism within the projector augmented-wave method. Phys Rev B. 2000;62:11556–70.
- 39. Dudarev SL, Botton GA, Savrasov SY, et al. Electron-energy-loss spectra and the structural stability of nickel oxide: an LSDA+U study. Phys Rev B. 1998;57:1505–9.
- 40. Liu Z, Liu C-X, Wu Y-S, et al. Stable nontrivial Z<sub>2</sub> topology in ultrathin Bi(111) films: a first-principles study. Phys Rev Lett. 2011;107:136805.
- 41. Xu G, Weng H, Wang Z, et al. Chern semimetal and the quantized anomalous Hall effect in HgCr<sub>2</sub>Se<sub>4</sub>. Phys Rev Lett. 2011;107:186806.
- 42. Liu C-X, Qi X-L, Zhang H, et al. Model Hamiltonian for topological insulators. Phys Rev B. 2010;82:045122.
- 43. Liu C-X, Zhang H, Yan B, et al. Oscillatory crossover from two-dimensional to three-dimensional topological insulators. Phys Rev B. 2010;81:041307.
- Sinova J, Jungwirth T, Cerne J. Magneto-transport and magneto-optical properties of ferromagnetic (III, Mn)V semiconductors: a review. Int J Mod Phys B. 2004;18:1083–118.
- 45. MacDonald A, Niu Q. New twist for magnetic monopoles. Phys World. 2004;17:18-9.
- 46. Ashcroft NW, Mermin DN. Solid state physics. New York: Saunders College; 1976.

# Chapter 5 **Quantum Anomalous Hall Effect**

In this chapter, we report the observation of the quantum anomalous Hall effect (QAHE) in Cr-doped  $(Bi,Sb)_2Te_3$  TI thin films grown by MBE method. At zero magnetic field and ultralow temperature (30 mK), the gate-tuned anomalous Hall resistance reaches the predicted quantized value of  $h/e^2$ , accompanied by a considerable drop in the longitudinal resistance. Under a strong magnetic field (up to 18 T), the longitudinal resistance vanishes, whereas the Hall resistance remains at the quantized value. The realization of the QAHE may lead to the development of low-power-consumption electronics. The main findings and conclusions in this chapter have been published in Ref. [1], reprinted with the permission of full text and figures from AAAS.

## 5.1 Introduction to QAHE

In QAHE, a quantized version of anomalous Hall effect (AHE) [2], the transverse Hall resistance is exactly quantized into the plateau  $h/e^2$  even in the absence of an external magnetic field. Comparing with the traditional quantum Hall effect (QHE), the topologically non-trivial electronic structure in QAHE is generally caused by the combination of spontaneous magnetization and spin–orbit coupling rather than the magnetic field-induced Landau quantization. As a consequence, the quantized Hall effect produced by the dissipationless edge states can be observed without any external magnetic field.

Ever since the proposal of Haldane model [3], there have been numerous approaches to realize the AQHE [4–10]. Among these proposals, using magnetically doped TI thin films is one of the most promising routes. However, there are three crucial criteria for observing the QAHE: (i) FM order that breaks the TRS, (ii) topologically non-trivial band structure, and (iii) 2D insulating state. When all these criteria are fulfilled simultaneously, a plateau of Hall conductance ( $\sigma_{xy}$ ) of  $e^2/h$  together with a vanishing longitudinal conductance ( $\sigma_{xx}$ ) even at zero magnetic

field would be observed by tuning the Fermi level into the magnetically induced energy gap (Fig. 5.1).

Whether such an insulating ferromagnetic thin film with topologically non-trivial band structure could be achieved in principle? A positive answer is provided by Yu et al. [4] based on first-principle calculations. Here, we briefly introduce their proposal of realizing QAHE in magnetically doped Bi<sub>2</sub>Se<sub>3</sub> family compounds, in which we indeed observe the QAHE experimentally.

In the TIs doped with dilute magnetic ions, the whole system can be divided into two subsystems, the local moments and band electrons. And the magnetic exchange interaction among local moments is mediated by the band electrons. Thus, the total free energy of the system in an external magnetic field H can be expressed as follows:

$$F_{\text{total}} = \frac{1}{2} \chi_L^{-1} M_L^2 + \frac{1}{2} \chi_e^{-1} M_e^2 - J_{\text{eff}} M_L M_e - (M_L + M_e) H, \tag{5.1}$$

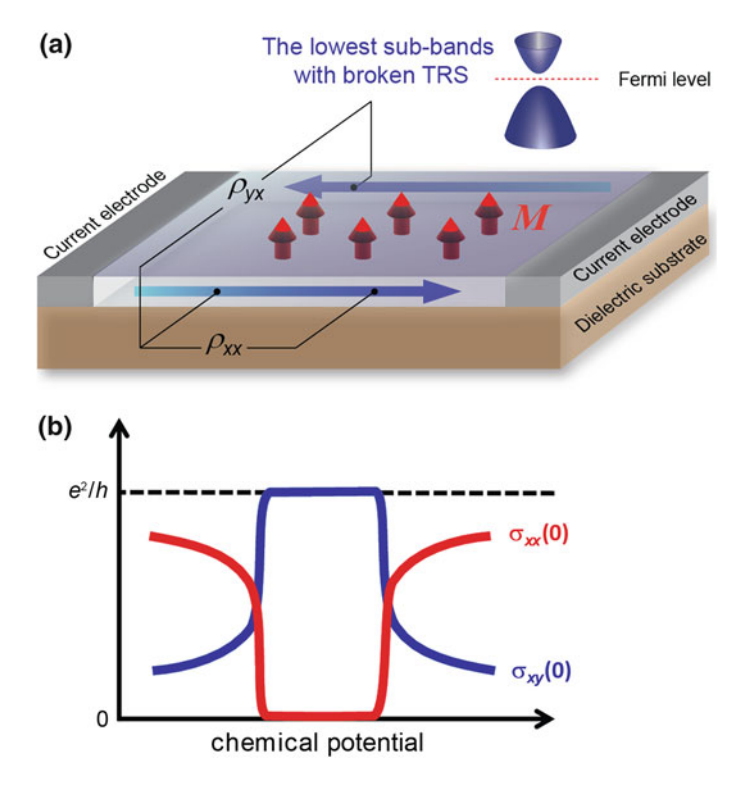


**Fig. 5.1 a** The schematic structure of QAHE in a TI thin film with ferromagnetism. The *blue arrows* indicate the dissipationless edge state of QAHE. The magnetization direction is indicated by *red arrows*. The chemical potential of the film can be controlled by a gate voltage applied on the backside of the dielectric substrate. **b** The schematic diagram of  $\sigma_{xx}$  (*red*) and  $\sigma_{xy}$  (*blue*) as a function of chemical potential without external magnetic field

where  $\chi_{L/e}$  is the spin susceptibility of the local moments/electrons,  $M_{L/e}$  denotes the magnetization for the local moment/electron subsystem, and  $J_{\text{eff}}$  is the magnetic exchange coupling between them. In order to have a nonzero FM transition temperature,  $F_{\text{total}}$  should be less than zero when H = 0, which leads to a requirement of  $\chi_L > 1/(J_{\rm eff}\chi_e)$ . In the dilute limit,  $\chi_L$  follows the Curie–Weiss law, proportional to  $T^{-1}$ . Therefore, a sizable  $\chi_e$  is necessary to form FM order at nonzero temperature. Comparing with the carrier-induced ferromagnetism in dilute magnetic semiconductors, the insulating Bi<sub>2</sub>Se<sub>3</sub> family compound possesses considerable spin susceptibility through the van Vleck paramagnetism, as discussed in Sect. 4.10. Meanwhile, a sizable  $J_{\text{eff}}$  is also required. We have calculated the exchange coupling between two magnetic impurities in Cr-doped  $Bi_2(Se_xTe_{1-x})_3$  by using the energy-mapping methods with DFT calculations [11]. We found that for the topologically non-trivial Cr-doped Bi<sub>2</sub>Te<sub>3</sub>, J<sub>eff</sub> is around 2.0 meV/(Cr atom), and for the topologically trivial Cr-doped Bi<sub>2</sub>Se<sub>3</sub>, J<sub>eff</sub> is only about 0.68 meV/(Cr atom). The significantly enhanced exchange coupling and spin susceptibility in the topologically non-trivial phase are both highly favorable for the formation of spontaneous ferromagnetic ordering even in the insulating state.

In the presence of exchange field, the sub-band evolution is illustrated in Fig. 5.2. For the case of  $Bi_2Se_3$  family thin films, the four sub-bands  $(|+,\uparrow\rangle, |-,\downarrow,|+,\downarrow)$ , and  $|-,\uparrow\rangle$ ) are composed of the top and surface states

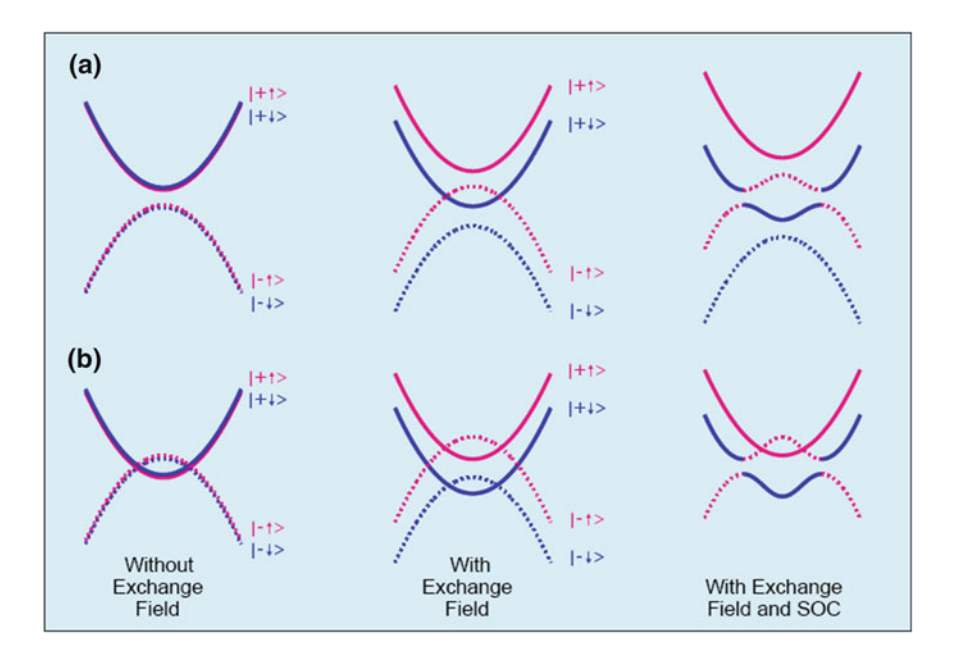


**Fig. 5.2** Evolution of the sub-band structure upon increasing the exchange field for noninverted (a) and inverted bands (b). The parity of sub-bands is indicated by the *solid* (+) or *dashed* (-) *lines*. The spin *up/down* elections are represented by *red/blue* color

before coupling with each other. Note that these sub-bands are different from the four bases that are used to describe bulk states in Chap. 4. As shown in Fig. 5.2a, when the four-band system is originally in the topologically trivial state, the exchange field will induce a band inversion in the one block  $(|+,\downarrow\rangle, |-,\uparrow\rangle)$  and increase the band gap for the other block  $(|+,\uparrow\rangle, |-,\downarrow\rangle)$ . On the other hand, if the system is originally in the topologically non-trivial state (Fig. 5.2b), a sufficiently large exchange field can increase the band inversion of one block  $(|+,\downarrow\rangle, |-,\uparrow\rangle)$  and eliminate it in the other block  $(|+,\uparrow\rangle, |-,\downarrow\rangle)$ . Therefore, regardless of the original states, an adequate exchange field will produce a single inverted block, which would contribute  $e^2/h$  for the Hall conductance. Such a mechanism is common in thin film TI systems with FM ordering on the condition that the surface states on the top and bottom surfaces have the same g factor.

### 5.2 Sample Preparation and Characterization

As proposed in Ref. [4], Cr-doped  $Bi_2Se_3$  family compounds are expected to exhibit QAHE in the thin film structure. Moreover, despite band structure engineering in  $(Bi_{1-x}Sb_x)_2Te_3$  ternary alloys (Chap. 3), we already have the ability of achieving truly insulating bulk and tunable surface states with Fermi level close to vicinity of the Dirac point. Meanwhile, in Chap. 4, we have established a well-defined out-of-plane ferromagnetism in Cr-doped  $Bi_2Te_3$  films with  $T_C$  about 20 K. Based on the above experimental capabilities and theoretician predictions, we decide to trace the QAHE in Cr-doped  $(Bi,Sb)_2Te_3$  films grown on dielectric  $SrTiO_3$  (111) substrates by MBE method.

The composition of the sample in which we indeed observed the QAHE is  $Cr_{0.15}(Bi_{0.1}Sb_{0.9})_{1.85}Te_3$  with a thickness of 5 QLs. With this composition, the film is nearly charge neutral so that the chemical potential can be fine-tuned to the electron- or hole-conductive regime by a positive or negative voltage, applied on the backside of the  $SrTiO_3$  substrate. The film is manually cut into a Hall bar configuration for transport measurements as shown in Fig. 2.8b. Varying the width (from 50 to 200  $\mu$ m) and the aspect ratio (from 1:1 to 2:1) of Hall bar does not influence the transport results.

Compared with the samples studied in our previous work [12], the quality of the current samples is significantly improved as the result of a systematic optimization of the MBE growth of Cr-doped (Bi,Sb)<sub>2</sub>Te<sub>3</sub> films. We replaced the old components (effusion cells, manipulators, etc.) in the MBE chamber to achieve a better UHV environment. We modified the surface treatment conditions of SrTiO<sub>3</sub> substrate for better morphology. We used a little bit lower substrate temperature during growth so that Cr could be incorporated more homogeneously into the films. The film thickness and composition are also fine-tuned and carefully checked. These efforts lead to larger terraces, reduced bulk carrier density, and higher mobility, which in turn result in larger anomalous Hall resistance and lower longitudinal resistance. Unlike the samples studied in Chaps. 3 and 4, the samples prepared for QAHE measurements

do not have any capping layers on the top, because we found that the amorphous Te capping layer which is used to protect film from contamination for ex situ measurements is deleterious to the occurrence of the QAHE. Besides the 5 QL samples, we also carried out the measurements on Cr-doped (Bi,Sb)<sub>2</sub>Te<sub>3</sub> films with a thickness of 3 QL, 4 QL, and 8 QL. The 3 QL and 4 QL films are too insulating for transport measurements, most likely due to the less-ideal sample quality and possible ambient oxidation at such thin limit. For 8 QL films, the anomalous Hall resistance is much smaller than the quantized value at 30 mK, which probably results from the involvement of bulk or surface conductive channels.

Figure 5.3a shows the ARPES band structure of the  $Cr_{0.15}(Bi_{0.1}Sb_{0.9})_{1.85}Te_3$  film measured at 100 K along the K– $\Gamma$ –K direction. The well-defined surface states with linear dispersions are clearly observed and highlighted by red and blue dashed lines. The Dirac point is located at the position of  $E_F$  and in the bulk gap, which is a strong indication that the sample is close to the charge neutral situation and would exhibit an insulating behavior at low temperatures. Figure 5.3b displays an AFM image (2  $\mu$ m × 2  $\mu$ m) of the surface topography of  $Cr_{0.15}(Bi_{0.1}Sb_{0.9})_{1.85}Te_3$  film grown on  $SrTiO_3$  (111) substrate. The surface has one single terrace over the entire scan range with tiny islands (1 QL thick) randomly distributed on the top. The thickness of the film can be obtained by measuring the height difference between the film and the substrate. The line profile taken cross the edge shows a film thickness of 5 QL, which is consistent with that estimated from the MBE growth parameters.

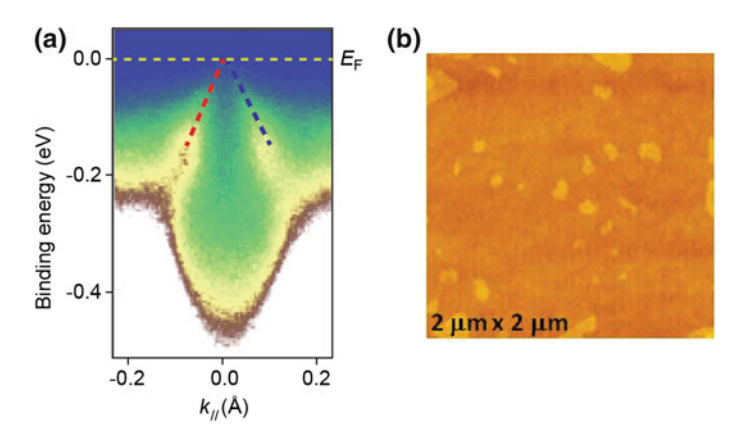


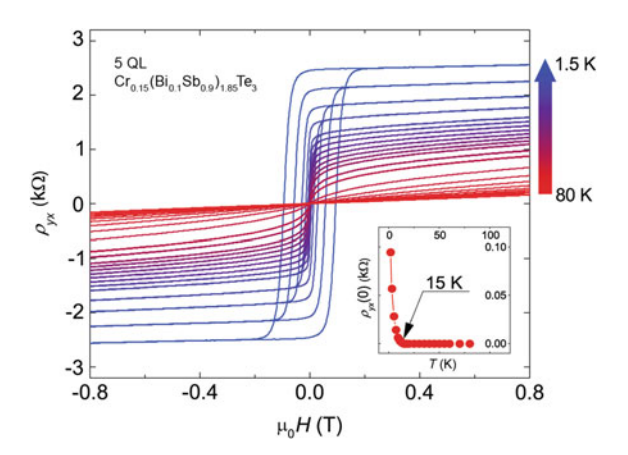
**Fig. 5.3** Characterizations of the 5 QL  $Cr_{0.15}(Bi_{0.1}Sb_{0.9})_{1.85}Te_3$  film grown on SrTiO<sub>3</sub> (111) substrate. **a** ARPES band mapping at T = 100 K along the K–Γ–K direction. The *red* and *blue dashed lines* indicate the surface states. The *yellow dotted line* represents the position of the Fermi level. **b** AFM surface morphology (2 μm × 2 μm) shows a large-scale flat terrace

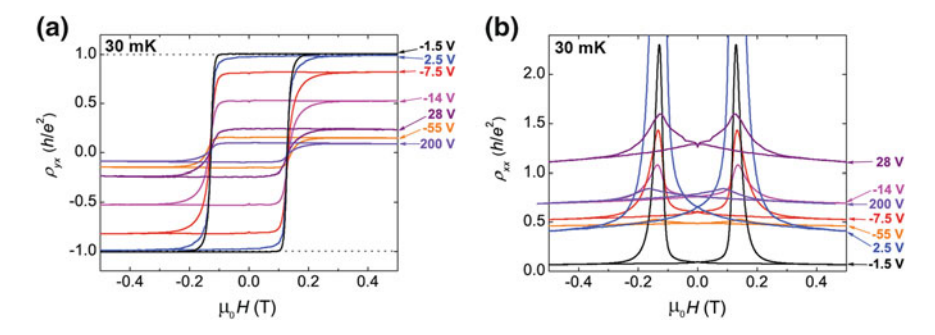
#### 5.3 Quantized Hall Resistance at Zero Magnetic Field

Figure 5.4 displays a series of magnetic field ( $\mu_0 H$ )-dependent Hall sheet resistances ( $\rho_{yx}$ ) of 5 QL Cr<sub>0.15</sub>(Bi<sub>0.1</sub>Sb<sub>0.9</sub>)<sub>1.85</sub>Te<sub>3</sub> film measured at different temperatures. At high temperatures,  $\rho_{yx}$  exhibits linear magnetic field dependence due to ordinary Hall effect (OHE). The electron's mobility can be estimated from the measured longitudinal sheet resistance ( $\rho_{xx}$ ) and the carrier density determined by OHE. And the result is only about 760 cm<sup>2</sup>/(V s), which is greatly enhanced compared with the samples in our previous work [12], but still much lower than that necessary for QHE [13]. With decreasing temperature,  $\rho_{yx}$  develops a hysteresis loop characteristic of the AHE, induced by the ferromagnetic order in the film [14]. The square-shaped loop with large coercivity ( $H_{coer}$  = 970 Oersted at 1.5 K) indicates a long-range ferromagnetic order with out-of-plane magnetic anisotropy. The Curie temperature is estimated to be ~15 K (Fig. 5.4, inset) from the temperature dependence of the zero-field  $\rho_{yx}$  that reflects spontaneous magnetization of the film. Based on the mean-field approximation, we can estimate the magnetically induced gap at the Dirac point to be around 2–3 meV.

Figure 5.5 shows the magnetic field dependence of  $\rho_{yx}$  and  $\rho_{xx}$ , respectively, measured at T=30 mK at different bottom gate voltages ( $V_{\rm g}$ s). The shape and coercivity of the  $\rho_{yx}$  hysteresis loops vary little with  $V_{\rm g}$ , thanks to the robust ferromagnetism probably mediated by the van Vleck mechanism [4]. In the magnetized states,  $\rho_{yx}$  is nearly independent of the magnetic field, suggesting perfect ferromagnetic ordering and charge neutrality of the sample. On the other hand, the anomalous Hall resistance (height of the loops) changes dramatically with  $V_{\rm g}$ , with a maximum value of  $h/e^2$  around  $V_{\rm g}=-1.5$  V. The magnetoresistance (MR) curves exhibit the typical shape for a ferromagnetic material: two sharp symmetric peaks at the coercive fields, which are induced by the enhanced scattering between elections in magnetization reversal process.

Fig. 5.4 The anomalous Hall resistance  $\rho_{yx}$  as a function of magnetic field measured at different temperatures (from 80 to 1.5 K). The inset shows the temperature dependent of  $\rho_{yx}$  at zero field, which gives a Curie temperature 15 K for the  $Cr_{0.15}(Bi_{0.1}Sb_{0.9})_{1.85}Te_3$  film





**Fig. 5.5** Transport results of 5 QL  $Cr_{0.15}(Bi_{0.1}Sb_{0.9})_{1.85}Te_3$  film at T=30 mK. **a** The anomalous Hall resistance changes dramatically with the bottom gate voltages and shows a quantized value of  $h/e^2$  around  $V_g^0 = -1.5$  V at zero magnetic field. **b** The MR curves exhibit a hysteresis characteristic with the peak values at the coercive fields

The  $V_{\rm g}$  dependences of  $\rho_{yx}$  and  $\rho_{xx}$  at zero field [labeled  $\rho_{yx}(0)$  and  $\rho_{xx}(0)$ , respectively] are plotted in Fig. 5.6a. The most important observation here is that the zero-field Hall resistance exhibits a distinct plateau with the quantized value  $h/e^2$  centered at charge neutral point, which corresponds a gate voltage  $V_{\rm g}^0 = -1.5$  V. This observation constitutes the discovery of the QAHE. Accompanying the quantization in  $\rho_{yx}(0)$ , the longitudinal resistance  $\rho_{xx}(0)$  exhibits a sharp dip down to 0.098  $h/e^2$  at the same gate voltage. The  $\rho_{yx}(0)/\rho_{xx}(0)$  ratio corresponds to a Hall angle of 84.4°. For comparison with theory, we transform  $\rho_{yx}(0)$  and  $\rho_{xx}(0)$  into sheet conductance through the relations  $\sigma_{xy} = \rho_{yx}/(\rho_{xx}^2 + \rho_{yx}^2)$  and  $\sigma_{xx} = \rho_{xx}/(\rho_{xx}^2 + \rho_{yx}^2)$ , and plot them in Fig. 5.6b. Around  $V_{\rm g}^0$ ,  $\sigma_{xy}(0)$  has a notable plateau at 0.987  $e^2/h$ , whereas  $\sigma_{xx}(0)$  has a dip down to 0.096  $e^2/h$ , similar to the behavior of the corresponding resistances.

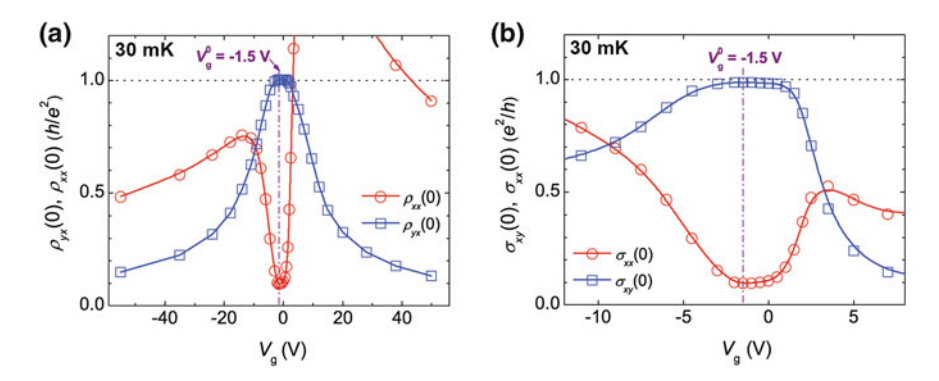


Fig. 5.6 a Dependence of  $\rho_{yx}(0)$  (empty blue squares) and  $\rho_{xx}(0)$  (empty red circles) on  $V_g$ . The resistance plateau at  $h/e^2$  extends about 3.5 V. Away from the plateau range,  $\rho_{yx}(0)$  and  $\rho_{xx}(0)$  have similar behaviors, which can be attributed to variation in carrier density. **b** Dependence of  $\sigma_{xy}(0)$  (empty blue squares) and  $\sigma_{xx}(0)$  (empty red circles) on  $V_g$ . The purple dash-dotted lines indicate the  $V_g$  for the charge neutral point  $(V_g^0)$ 

In addition to the observation of QAHE, the MR ratio,  $[\rho_{xx}(H_{coer}) - \rho_{xx}(0)]/\rho_{xx}(0)$ , is dramatically enhanced at  $V_g^0$  to a surprisingly large value of 2251 % (Fig. 5.5b). The huge MR can be understood in terms of quantum anomalous Hall (QAH) phenomenology. In the magnetized QAH state, the existence of dissipationless edge state leads to a nearly vanishing  $\rho_{xx}$ . At the coercive field, the magnetization reversal of a QAH system leads to a quantum phase transition between two QH states [5] via a highly dissipative phase with a large  $\rho_{xx}$ , although the exact mechanism may be complex [15]. The huge MR thus reflects the distinct difference in transport properties between an ordinary insulator and a QAH insulator.

For a QH system, when the Fermi level lies in the gap between Landau levels,  $\sigma_{xy}$  reaches a plateau at  $ve^2/h$  and  $\sigma_{xx}$  drops to zero. If the system contains non-localized dissipative conduction channels,  $\sigma_{xx}$  has a nonzero value, whereas  $\sigma_{xy}$  deviates slightly from the quantized plateau [16]. For a QAH system, only one  $\sigma_{xy}$  plateau of  $e^2/h$  appears at zero field when the Fermi level falls in the mobility edges around the magnetically induced gap (Fig. 5.1b). The observations of  $\sigma_{xy}(0) = e^2/h$  plateau and the dip in  $\sigma_{xx}(0)$  near the charge neutral point in Fig. 5.6b agree well with the theoretical prediction for a QAH system with residual dissipative channels which are expected to vanish completely at zero temperature [6, 16]. Recently, the coexistence of gapless non-chiral edge states and dissipationless chiral edge state has been predicted by the first-principle calculations in Cr-doped (Bi,Sb)<sub>2</sub>Te<sub>3</sub> films, where exact quantization of  $\rho_{yx}$  can be guaranteed with nonzero  $\rho_{xx}$  [17].

### 5.4 Vanishing Residual Resistance at High Magnetic Field

To confirm the QAHE observed in Fig. 5.5, we apply a high magnetic field, aiming to localize all possible dissipative states in the sample. Figure 5.7a, b displays the magnetic field dependence of  $\rho_{yx}$  and  $\rho_{xx}$  of the same sample in Fig. 5.5. Besides the large MR at  $H_{\text{coer}}$ , increasing the field further suppresses  $\rho_{xx}$  toward zero. Above

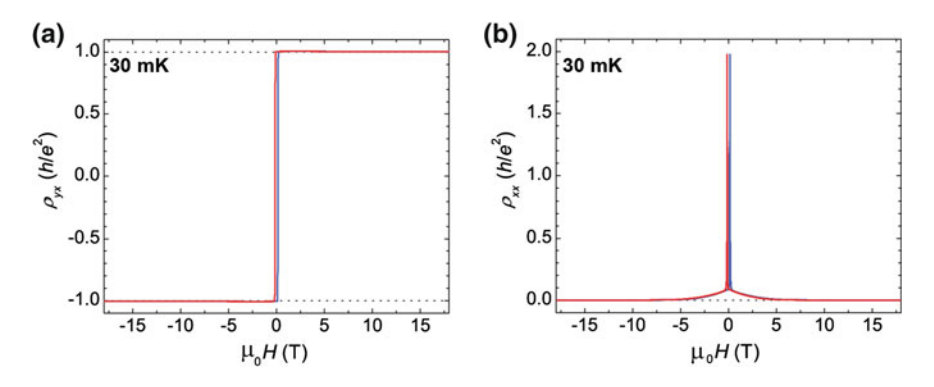


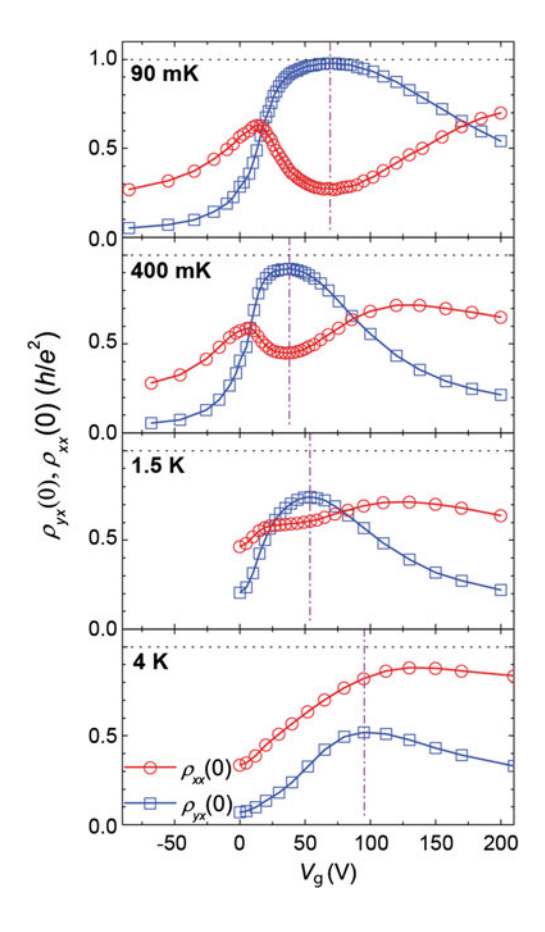
**Fig. 5.7** High magnetic field measurements of  $\rho_{yx}$  (**a**) and  $\rho_{xx}$  (**b**) at  $V_g^0$  up to 18 T at 30 mK. The *blue* and *red lines* indicate the data taken at increasing and decreasing fields, respectively

10 T,  $\rho_{xx}$  vanishes completely, corresponding to a perfect QH state. It is noteworthy that the increase in  $\rho_{xx}$  from zero (above 10 T) to 0.098  $h/e^2$  (at zero field) is very smooth and  $\rho_{yx}$  remains at the quantized value  $h/e^2$ , which indicates that no quantum phase transition occurs, and the sample stays in the same QH phase as the field sweeps from 10 T to zero. Therefore, the complete quantization above 10 T can only be attributed to the same QAH state at zero field.

#### 5.5 Evolution of QAHE with Varied Temperatures

The observation of the QAHE is further supported by the behavior with varying temperatures. In Fig. 5.8, we show  $V_g$  dependences of  $\rho_{yx}(0)$  and  $\rho_{xx}(0)$  measured at different temperatures in another sample with the same growth conditions. The  $\rho_{yx}(0)$  always exhibits a single maximum, with the peak value considerably suppressed by increasing temperatures, accompanied by a disappearance of the dip in

Fig. 5.8 Temperature dependence of OAHE. a Gate voltage dependent of  $\rho_{vx}(0)$ and  $\rho_{xx}(0)$  measured at 90 mK, 400 mK, 1.5 K, and 4 K, respectively. The purple dash-dotted lines indicate the  $V_{g}$  for the charge neutral point  $(\tilde{V}_{g}^{0})$ . The variation in the position and width of the  $\rho_{vx}(0)$  peak at different temperatures is due to the change in substrate dielectric properties induced by temperature and charging cycles



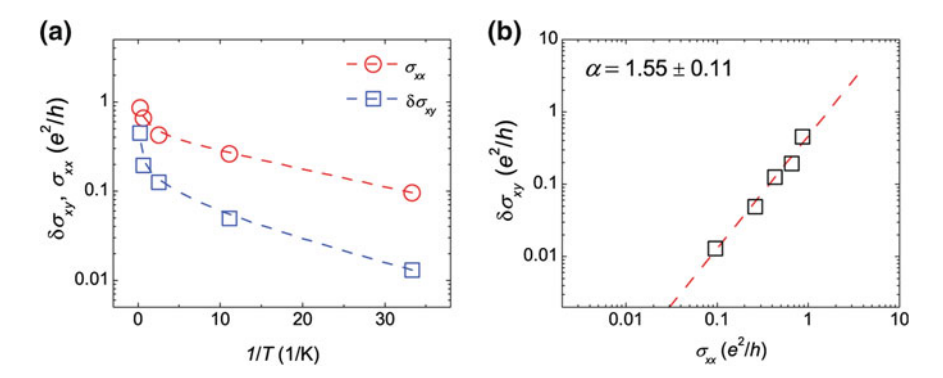


Fig. 5.9 a Dependence of logarithmically scaled  $\sigma_{xx}(0)$  (*empty blue squares*) and  $\delta\sigma_{xy}(0)$  (*empty red circles*) at  $V_g^0$  on inverse temperature. The *blue* and *dashed lines* are to guide the eyes. **b** The relation between  $\delta\sigma_{xy}(0)$  and  $\sigma_{xx}(0)$  at  $V_g^0$  in double logarithmic scale (*empty black squares*). The *red dashed line* indicates the fitting result with power function  $\delta\sigma_{xy} \propto \sigma_{xx}^{\alpha}$ , from which the fitted power  $\sigma \sim 1.55$  is obtained

 $\rho_{xx}(0)$ . At T=4 K,  $\rho_{xx}(0)$  returns to a typical behavior of a magnetic semiconductor with the  $\rho_{xx}(0)$  peak located at the right side of  $\rho_{yx}(0)$  peak, which can be attributed to lower mobility of electrons than holes in the sample. The vanishing indication of QAHE at high temperatures can be attributed to the increasing of dissipative channels generated by thermal activation.

The  $\sigma_{xx}(0)$  extracted from these measurements (in logarithmical scale) (Fig. 5.9a) exhibits a temperature dependence similar to that in integer QH systems: The drop of  $\sigma_{xx}$  is at first rapid, resulting from the freezing of the thermal activation mechanism, and then becomes much slower when the temperature is below 1 K. It can be attributed to variable range hopping (VRH) [16], but its exact mechanism remains unknown. Similar to the QHE, zero-field  $\sigma_{xx}$  is expected to decrease to zero at sufficiently low temperature. In Fig. 5.9b, we plot the relation between  $\sigma_{xx}(0)$  and  $\delta\sigma_{xy}(0)$  ( $\delta\sigma_{xy} = e^2/h - \sigma_{xy}$ , which reflects the contribution of dissipative channels). A power law relation  $\delta\sigma_{xy} \propto \sigma_{xx}^{\alpha}$ , with  $\alpha \sim 1.55$ , is obtained. For a ferromagnetic insulator in the VRH regime, the anomalous Hall conductivity is related to the longitudinal conductivity through  $\sigma_{AH} = A\sigma_{xx}^{\alpha}$ , where the power  $\alpha$  is  $\sim 1.6$  and the prefactor A can be positive or negative depending on materials [14]. The above result can thus be qualitatively understood within the VRH framework.

#### 5.6 Conclusion

Our results demonstrate the realization of the QAHE in magnetic TIs. Compared with QHE systems, all the samples studied in this work have a rather low mobility (< 1000 cm<sup>2</sup>/V s). Such robust QAH states not only reflect the topological character of TIs but also make the QAH systems readily achievable in experiments.

5.6 Conclusion 97

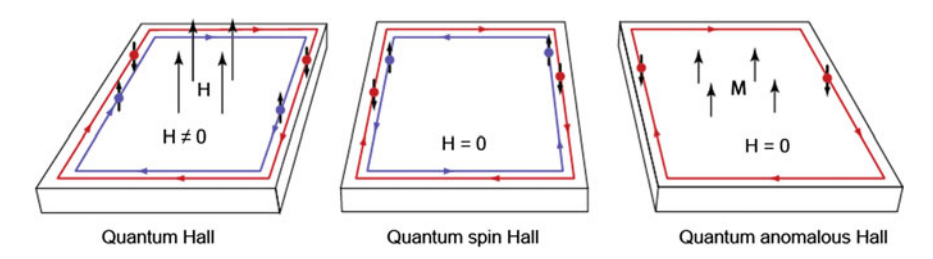


Fig. 5.10 The quantum Hall trio. H and M represent external magnetic field and the magnetization. The red and blue loops stand for dissipationless edge states with the arrows indicating the moving direction of electrons (red/blue solid circles). The spin polarization of each loop is marked by the black arrows

Because the realization of the QAHE and dissipationless edge states does not require any magnetic field, the present work paves a path for developing low-power-consumption, topological quantum electronic, and spintronic devices.

Up to now, the Quantum Hall trio has been completed [18]. As shown in Fig. 5.10, for all three quantum Hall effects, electrons flow through the dissipationless edge channels, while the rest of the sample remains insulating. In QH system, when there is a net forward flow of electrons (from bottom to top) for Hall resistance measurement, those extra electrons occupy only the left edge channels regardless of their spins. Moreover, the number of these edge channels v determines the quantized Hal resistance value  $h/ve^2$ . Whenever quantization occurs in the Hall resistance, the longitudinal resistance of the sample will reduce to zero. In QSH system, the dissipationless edge channels are demonstrated to exist in the absence of external magnetic field. And the flowing direction of each channel is either clockwise or counterclockwise, determined by its spin orientation (either up or down). When a net current is required for transport measurement, extra electrons with opposite spins would flow on both sides within different channels. Therefore, the Hall resistance remains zero and the longitudinal resistance is quantized to a certain value determined by the measurement geometry. If one of the spin channels in the QSH system is killed, for example, by ferromagnetism, it naturally develops into the QAH system, in which only one edge channel survives with unique spin orientation and flowing direction. The QAH system can also be simply regarded as a specific OH system with v = 1 and the role of magnetic field is replaced by the magnetization.

#### References

- 1. Chang C-Z, Zhang J, Feng X, et al. Experimental observation of the quantum anomalous Hall effect in a magnetic topological insulator. Science. 2013;340:167–70.
- 2. Hall EH. On the "Rotational Coefficient" in nickel and cobalt. Philos Mag. 1881;12:157–72.

- 3. Haldane FDM. Model for a quantum Hall effect without Landau levels: condensed-matter realization of the "parity anomaly". Phys Rev Lett. 1988;61:2015–8.
- 4. Yu R, Zhang W, Zhang HJ, et al. Quantized anomalous Hall effect in magnetic topological insulators. Science. 2010;329:61–4.
- 5. Qi X-L, Hughes TL, Zhang S-C. Topological field theory of time-reversal invariant insulators. Phys Rev B. 2008;78:195424.
- Nomura K, Nagaosa N. Surface-quantized anomalous Hall current and the magnetoelectric effect in magnetically disordered topological insulators. Phys Rev Lett. 2011;106:166802.
- 7. Onoda M, Nagaosa N. Quantized anomalous Hall effect in two-dimensional ferromagnets: quantum Hall effect in metals. Phys Rev Lett. 2003;90:206601.
- 8. Qi X-L, Wu Y-S, Zhang S-C. Topological quantization of the spin Hall effect in two-dimensional paramagnetic semiconductors. Phys Rev B. 2006;74:085308.
- 9. Liu C-X, Qi X-L, Dai X, et al. Quantum anomalous Hall Effect in Hg1-yMnyTe quantum wells. Phys Rev Lett. 2008;101:146802.
- Qiao Z, Yang SA, Feng W, et al. Quantum anomalous Hall effect in graphene from Rashba and exchange effects. Phys Rev B. 2010;82:161414.
- 11. Li ZL, Yang JH, Chen GH, et al. Strong single-ion anisotropy and anisotropic interactions of magnetic adatoms induced by topological surface states. Phys Rev B. 2012;85:054426.
- 12. Chang C-Z, Zhang J, Liu M, et al. Thin films of magnetically doped topological insulator with carrier-independent long-range ferromagnetic order. Adv Mater. 2013;25:1065–70.
- von Klitzing K, Dorda G, Pepper M. New method for high-accuracy determination of the fine-structure constant based on quantized Hall resistance. Phys Rev Lett. 1980; 45:494–7.
- 14. Nagaosa N, Sinova J, Onoda S, et al. Anomalous Hall effect. Rev Mod Phys. 2010;82:1539–92.
- 15. Checkelsky JG, Ye J, Onose Y, et al. Dirac-fermion-mediated ferromagnetism in a topological insulator. Nat Phys. 2012;8:729–33.
- Jeckelmann B, Jeanneret B. The quantum Hall effect as an electrical resistance standard. Rep Prog Phys. 2001;64:1603.
- 17. Wang J, Lian B, Zhang H, et al. Anomalous edge transport in the quantum anomalous Hall state. Phys Rev Lett. 2013;111:086803.
- 18. Oh S. The complete quantum Hall trio. Science. 2013;340:153-4.

# **Chapter 6 Dichotomy Between Electrical and Thermoelectric Properties**

Electrons in topological insulators can be classified as uniformly distributed bulk band electrons and topologically protected surface Dirac fermions. These electrons have different responses to the electrical and thermal excitations, leading to unexpected collective effects. In this chapter, we report a detailed study on the transport properties of ultrathin (Bi<sub>1-x</sub>Sb<sub>x</sub>)<sub>2</sub>Te<sub>3</sub> topological insulator films grown on SrTiO<sub>3</sub> substrates by MBE method. A sign anomaly between the Hall effect and the Seebeck coefficient is observed at certain Sb concentrations and temperatures, which can be quantitatively explained by two-band model calculations. This anomalous effect reveals that when the Fermi level lies in the vicinity of valence band maximum (VBM), the high-mobility surface Dirac fermions dominate the electrical transport, while the thermoelectric effect is determined by the bulk states at high temperatures. The dichotomy between the electrical and the thermoelectric transport properties demonstrated here opens a new route for designing high zT thermoelectric devices with surface-state-dominated conductance and bulk-state-dominated Seebeck coefficient. The main conclusions in this chapter have been published in Ref. [1], reprinted with the permission of full article from American Physical Society, copyright 2015.

### 6.1 Introduction to Thermoelectric Effect in TIs

The thermoelectric effect is the conversion of either temperature differences to electric voltage (Seebeck effect) or electric current to heat current (Peltier effect). At the basic level, these phenomena can be understood by the Drude model. An applied temperature gradient causes charge carriers to diffuse from the hot side to the cold side and accumulate at the cold side, thus generating an electric potential difference; on the other hand, electric current can drive "hot" charge carriers from one side of the junction to the other side, resulting in a heat flow. Based on these effects, thermoelectric devices can be used in applications including power generation and refrigeration.

The performance of a thermoelectric material for both power generation and refrigeration is determined by its figure of merit (zT):

$$zT = \frac{S^2 \sigma}{\kappa} T. \tag{6.1}$$

where S,  $\sigma$ , T, and  $\kappa$  are the Seebeck coefficient, electrical conductivity, absolute temperature, and thermal conductivity, respectively. To reach higher zT, a larger S, a better  $\sigma$ , and a lower  $\kappa$  are required. However, these parameters are entangled with each other: A higher S prefers lower carrier density, which leads to a worse  $\sigma$ ; a better  $\sigma$  comes together with a higher  $\kappa$  contributed from elections. As shown in Fig. 6.1, the optimum zT of bulk Bi<sub>2</sub>Te<sub>3</sub> is obtained when the charge carrier density is around  $5 \times 10^{19} \ {\rm cm}^{-3}$ . At this carrier concentration, Bi<sub>2</sub>Te<sub>3</sub> is heavily doped and behaves more like a metal.

It is well known as early as 1950s that the 3D TIs such as  $Bi_2Te_3$  and  $Sb_2Te_3$  are among the best thermoelectric materials at room temperature [2, 3], as shown in Fig. 6.2. This is because TIs and good thermoelectric compounds usually have the same traits such as heavy elements and narrow band gap. Therefore, both the non-trivial topological effect and high thermoelectric performance could be found in the same materials [4].

Although extensive efforts have been made to improve the zT, the maximum value for commercial materials based on  $\mathrm{Bi_2Te_3}$  and its alloys remains around 1 (Fig. 6.2), which is not efficient enough to be widely used in most applications [2–5]. However, twenty years ago, a theoretical prediction suggested that zT could be greatly enhanced in low-dimensional thermoelectric materials [6, 7], which led to a revival of experimental interest in searching for the proof-of-principle and high-efficiency devices, particularly in nanostructured alloys [5, 8] and superlattice [9, 10].

Fig. 6.1 The calculated results of the Seebeck coefficient S, electrical conductivity  $\sigma$ , and thermal conductivity  $\kappa$  as a function of carrier concentration in Bi<sub>2</sub>Te<sub>3</sub>. The optimized zT is reached via a compromise of these three parameters. Reprinted with the permission from Macmillan Publishers Ltd: Ref. [2], copyright 2008

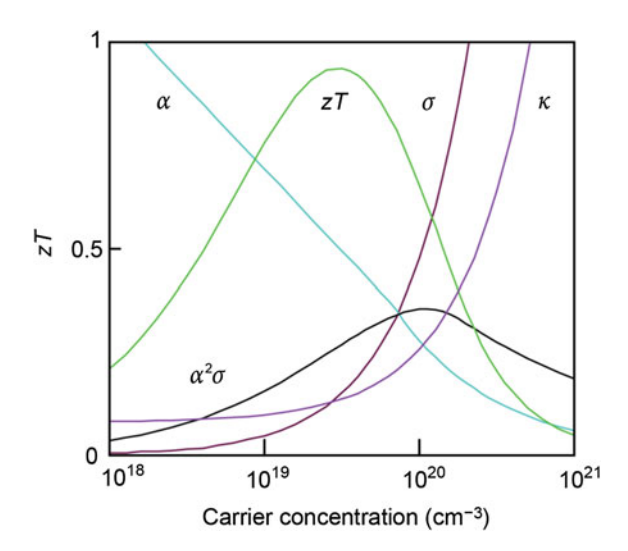
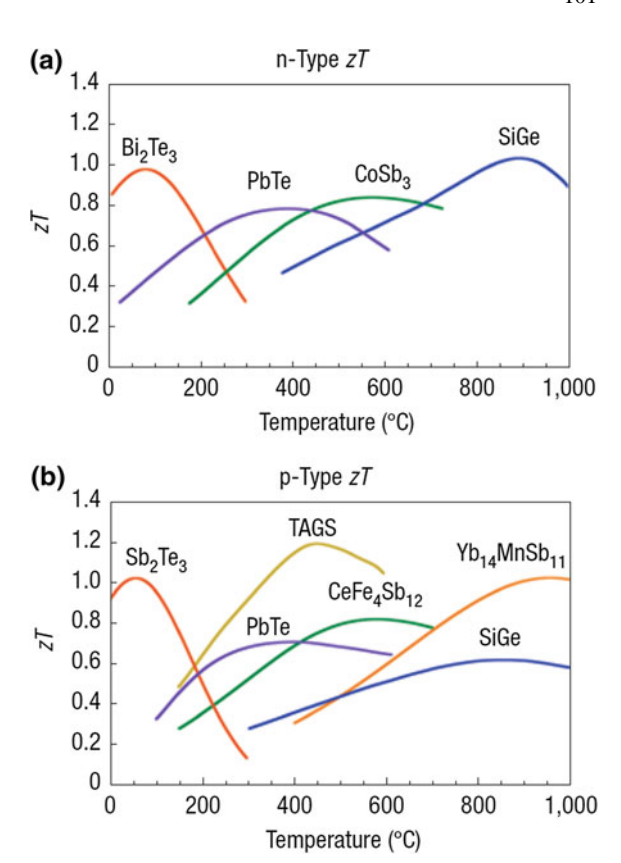


Fig. 6.2 The temperature dependence of zT for the of state-of-the-art commercial materials with n-type (a) and p-type (b) charge carriers. Reprinted with the permission from Macmillan Publishers Ltd: Ref. [2], copyright 2008



### 6.2 Experimental Design

Inspired by the above theoretical prediction, we decided to explore the thermoelectric properties of ultrathin  $(Bi_{1-x}Sb_x)_2Te_3$  TI films in which the coexistence of surface states and low dimensionality may produce some unexpected transport effects. In Chap. 3, we have systematically tuned the band structure and Fermi level  $(E_F)$  by carefully varying the Bi/Sb ratio in  $(Bi_{1-x}Sb_x)_2Te_3$  ternary alloys grown by means of MBE. Here, the same TI films are grown on SrTiO<sub>3</sub> substrates instead of the good thermal conductor sapphire. All the films have the same thickness d=5QL, so that the top and bottom surfaces do not hybridize with each other. Moreover, a layer of amorphous Te is deposited on the top to prevent unintentional contamination.

### **6.3** Electrical and Thermoelectric Measurements

Thermoelectric measurements on the TI films are made in the presence of a temperature gradient  $(\nabla T)$  in the lengthwise direction (Fig. 2.9), but for the electrical measurements the heater has to be shut off to keep the films isothermal. In pure Bi<sub>2</sub>Te<sub>3</sub> (x = 0) and Sb<sub>2</sub>Te<sub>3</sub> (x = 1), the two-dimensional (2D) resistivity shows metallic behavior at high T and becomes weakly insulating at T < 10 K. This behavior is typical in the TI films with higher carrier density as that shown in Fig. 3.7 with x = 0, 1. The Seebeck coefficients  $(S_{xx})$  of these two samples are shown in Fig. 6.3a, which displays a quasi-linear relationship as increasing T, but with opposite signs. This is because the  $E_{\rm F}$  of Bi<sub>2</sub>Te<sub>3</sub> lies in the bulk conduction band due to the n-type bulk carriers (Fig. 6.3b), which exhibit negative  $S_{xx}$ . However, in Sb<sub>2</sub>Te<sub>3</sub> the  $E_F$  is lower than the maximum of bulk valence band and the positive  $S_{xx}$  is produced by the p-type bulk carriers (Fig. 6.3b). At room temperature, the  $S_{xx}$  of Sb<sub>2</sub>Te<sub>3</sub> is 120  $\mu$ V/K, comparable to the best bulk value [3]. While for  $Bi_2Te_3$ , the  $S_{xx}$  is only about 30 μV/K, much lower than that reported for the best n-type bulk materials. This is because  $S_{xx}$  can be strongly suppressed by the effect of non-stoichiometry [11], which is caused by excessive Te vacancies and further demonstrated by the extremely large charge carrier density as that shown in Fig. 6.3b.

To introduce the thermoelectric contribution of Dirac fermions in the surface states, we fabricated  $(Bi_{1-x}Sb_x)_2Te_3$ , an isostructural and isovalent mixture of  $Bi_2Te_3$  and  $Sb_2Te_3$ . Figure 6.4a displays the Seebeck coefficient of five  $(Bi_{1-x}Sb_x)_2Te_3$  films with  $0.7 \le x \le 0.97$ . For the samples with x = 0.7 and 0.8, the  $S_{xx}$  reveals a sign change from negative to positive with increasing temperatures. However, the Hall effect does not show any sign change and remains negative in the same temperature range (Fig. 6.4b). As the Sb content is increased to x = 0.9, the

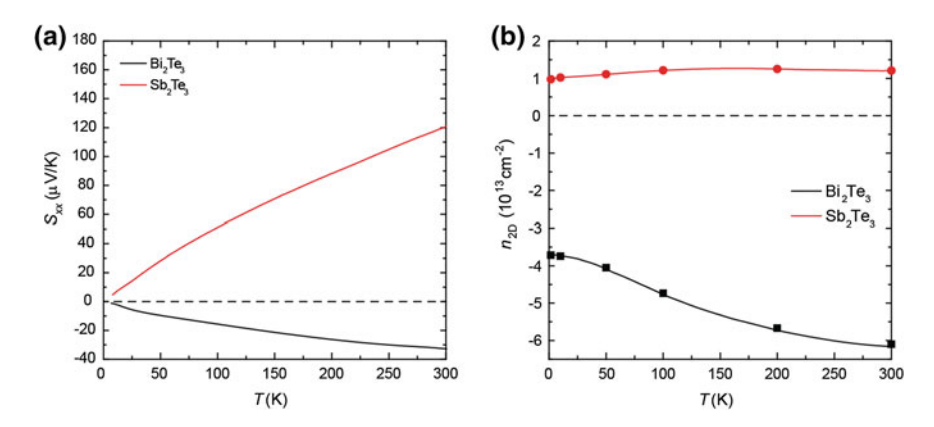


**Fig. 6.3** Transport measurements in 5 QL Bi<sub>2</sub>Te<sub>3</sub> and Sb<sub>2</sub>Te<sub>3</sub> films. **a** Both in Bi<sub>2</sub>Te<sub>3</sub> and in Sb<sub>2</sub>Te<sub>3</sub>, the  $S_{xx}$  has a quasi-linear T dependence, but with opposite signs. **b** The charge carriers in Bi<sub>2</sub>Te<sub>3</sub> are electron-like and thus contribute negative  $S_{xx}$ , whereas in Sb<sub>2</sub>Te<sub>3</sub> the hole-like charge carriers contribute positive  $S_{xx}$ 

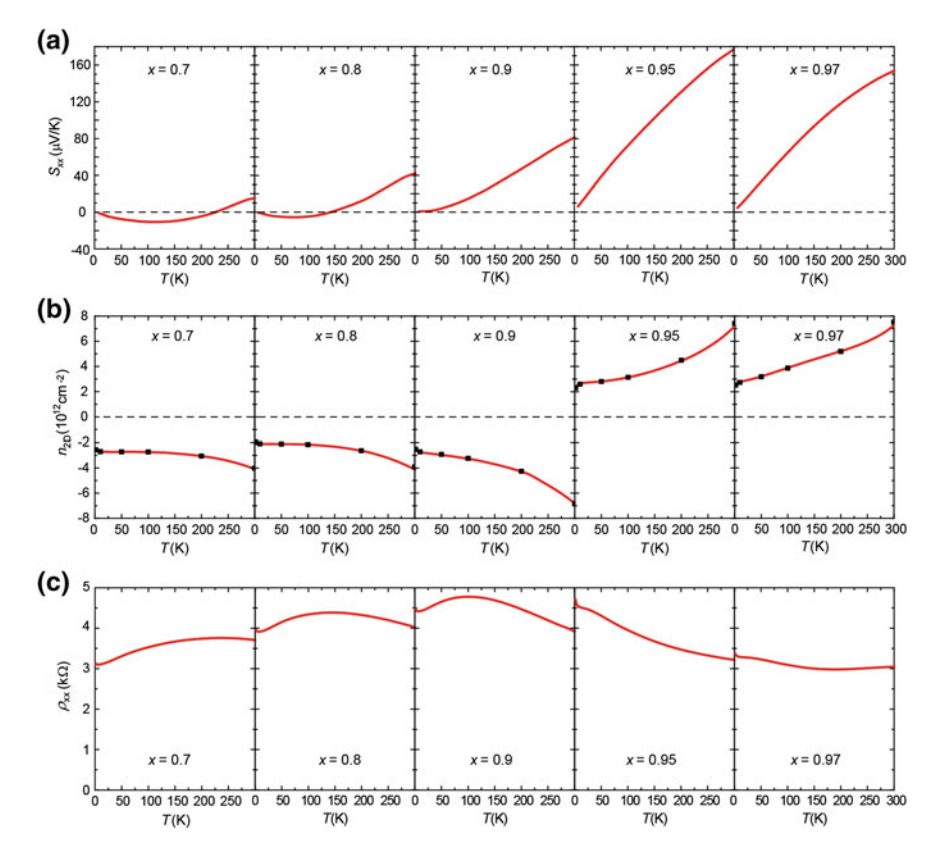
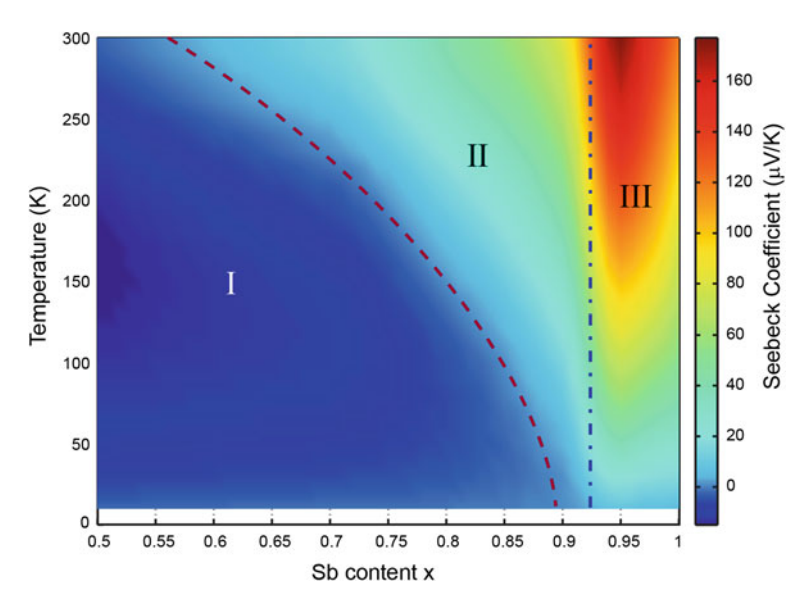


Fig. 6.4 The transport results of the 5 QL  $(Bi_{1-x}Sb_x)_2Te_3$  films with  $0.7 \le x \le 0.97$ . **a** In the samples with x = 0.7 and 0.8, a sign reversal of  $S_{xx}$  from negative to positive is revealed as T rises. As x is further increased from x = 0.9 to 0.97, the sign reversal totally disappears and a positive maximum value is obtained for x = 0.95. **b** For each sample the sign of  $n_{2D}$  is unchanged as increasing T (negative for  $x \le 0.9$  and positive for  $x \ge 0.95$ ), only the magnitude is increased due to the thermal excitation. At high T, the sign anomaly between the  $S_{xx}$  and  $n_{2D}$  is clearly revealed for  $0.7 \le x \le 0.9$ . **c** The  $\rho_{xx}$  shows an enhanced insulating tendency and maximum value when x is close to 0.95

 $S_{xx}$  is always positive and the sign change disappears at all temperatures. However, the Hall effect in this sample remains negative, totally opposite to the sign of  $S_{xx}$ . With further increase of x to 0.95 and 0.97, a positive maximum value of  $S_{xx}$  is obtained for x = 0.95 with value as large as 180  $\mu$ V/K at room temperature. Then, it decreases as x is increased from 0.97 to 1.0 (Figs. 6.3a and 6.4a). Moreover, the sign of the Hall effect changes to positive right at x = 0.95 (Fig. 6.4b). For these five samples with  $0.7 \le x \le 0.97$ , the absolute value of nominal charge carrier densities ( $n_{\text{2D}} = 1/eR_{\text{H}}$ ) are all less than  $3 \times 10^{12}$  cm<sup>-2</sup> at T = 1.5 K, indicating that the  $E_{\text{F}}$  is very close to the Dirac point (DP). We note that the carrier density is only a rough estimate due to the existence of two surfaces and some bulk conductions. Figure 6.4c shows the evolution of two-dimensional resistivity ( $\rho_{xx}$ ) with T for



**Fig. 6.5** Thermoelectric phase diagram of  $(Bi_{1-x}Sb_{x})_{2}Te_{3}$  films summarizing the  $S_{xx}$  as a function of x and T. The contours with  $S_{xx} = 0$  (wine dashed line) and  $n_{2D} = 0$  (blue dash-dotted line) divide this phase diagram into three regions: negative  $S_{xx}$  and  $n_{2D}$  (region I), positive  $S_{xx}$  but negative  $n_{2D}$  (region II), and positive  $S_{xx}$  and  $n_{2D}$  (region III)

these five samples. The  $\rho_{xx}$  reveals a maximum and enhanced insulating behavior at x = 0.95, where the lowest p-type carrier density and largest positive  $S_{xx}$  coexist.

The thermoelectric effect of the  $(Bi_{1-x}Sb_x)_2Te_3$  system is summarized in Fig. 6.5 as a function of T and Sb content x. In this phase diagram, there are three distinct regions: negative  $S_{xx}$  with n-type charge carries (region I), positive  $S_{xx}$  with n-type charge carries (region II), and positive  $S_{xx}$  with positive charge carries (region III). For most thermoelectric systems, the sign of  $S_{xx}$  is always consistent with the type of charge carriers estimated from the Hall effect [3, 12, 13]. In other words, if the sign of  $S_{xx}$  changes at some critical point due to the chemical doping [14], then the type of charge carriers would also be reversed at the same transition point. However, in 5 QL  $(Bi_{1-x}Sb_x)_2Te_3$  TI films, the sign consistency between the Seebeck coefficient and Hall effect is violated, resulting in a dichotomy between the electrical and the thermoelectric transport properties.

#### **6.4 DFT Calculated Band Structures**

The DFT calculations are performed by the method similar to that described in Sect. 4.7. Here, the simulation package is BSTATE instead of Vienna. A k-mesh is taken as  $8 \times 8 \times 1$  for the 5 QL free-standing slabs with a 25 Bohr vacuum layer.

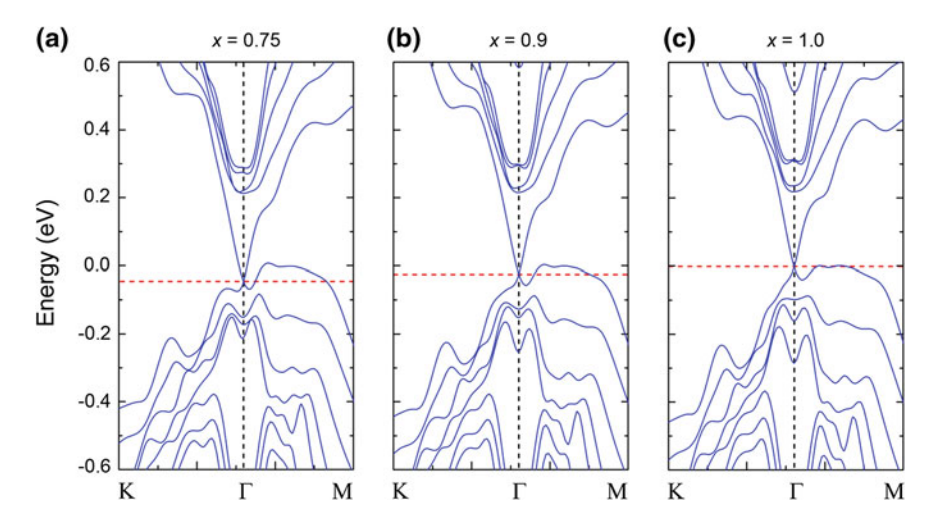


**Fig. 6.6** The bulk band structure of 5 QL  $(Bi_{1-x}Sb_x)_2Te_3$  calculated by the density functional theory with x = 0.75 (**a**), 0.9 (**b**), and 1.0 (**c**), respectively. Red dashed lines indicate the positions of Dirac points, and black dashed lines represent the locations of the Γ points

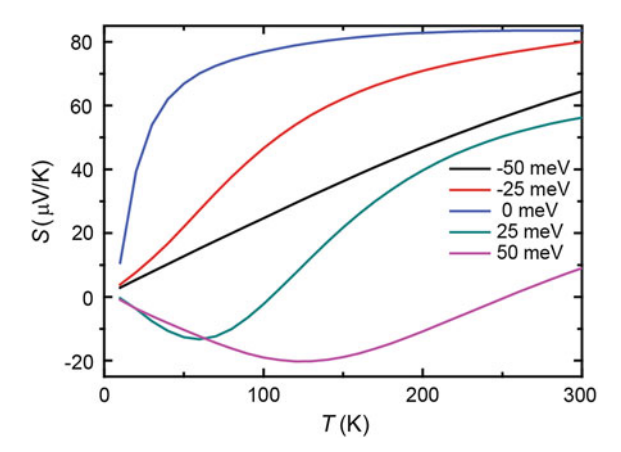
Virtual crystal method [15] is used to simulate the mixing of Bi and Sb. The lattice constant and the atomic position are obtained by linearly interpolating between Bi<sub>2</sub>Te<sub>3</sub> and Sb<sub>2</sub>Te<sub>3</sub>.

Figure 6.6 displays the band structures of 5 QL  $(Bi_{1-x}Sb_x)_2Te_3$  films along K- $\Gamma$ -M direction. The surface states can be clearly identified by two linear bands crossing at the  $\Gamma$  point around the Fermi level. With  $0.75 \le x \le 1.0$ , the overall band structures are almost the same and the only differences happen at the relative positions between DP and the VBM along the  $\Gamma$ -M direction. As shown in Fig. 6.6a, the energy of DP is about -45 meV for x = 0.75, which is lower than the energy of VBM. With increasing x to 0.9, the DP moves upward to about -25 meV but still lower than the VBM. For the pure  $Sb_2Te_3$  (x = 1.0), the DP now is aligned with the VBM and stay around zero energy. This variation tendency of DP is similar to that shown in Figs. 3.4 and 3.5 in  $\Gamma$ -K direction.

### 6.5 Calculated Seebeck Coefficient

The Seebeck coefficient is calculated by the Landauer approach with the constant mean free path model [16] based on the band structure in a dense k-mesh  $400 \times 400 \times 1$  from the maximally localized Wannier functions [17]. Here, two constant mean free paths of surface ( $\lambda_s$ ) and bulk states ( $\lambda_b$ ) are used to describe the transport properties, and their ratio  $r_{\lambda} = \lambda_s / \lambda_b$  is the only variable relevant to  $S_{xx}$ . Intuitively,  $r_{\lambda}$  should be larger than 1 due to the higher mobility of surface states, and it is selected to be 5 in our calculations.

**Fig. 6.7** The calculated Seebeck coefficient as a function of temperature with different Fermi levels relative to the valence band maximum



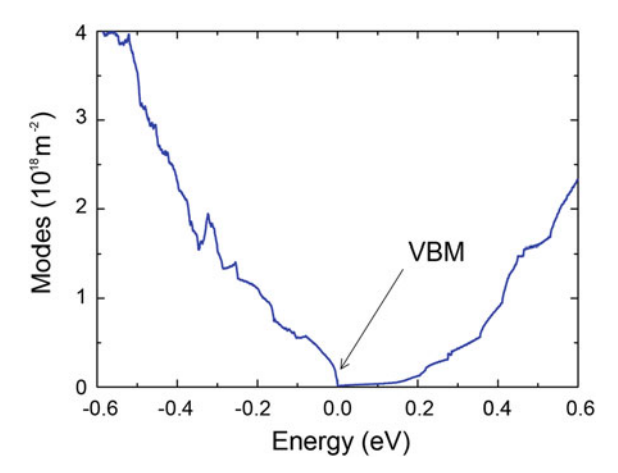
Since the overall band structures of 5 QL  $(Bi_{1-x}Sb_x)_2Te_3$  system with  $0.75 \le x \le 1.0$  remain nearly the same (Fig. 6.6), now we just focus on the band structure with x = 0.9 and calculate the  $S_{xx}$  at difference Fermi levels  $(E_Fs)$ . As shown in Fig. 6.7, for  $E_F \le 0$  (relative to VBM), the  $S_{xx}$  is always positive and shows a maximum value at  $E_F = 0$ . When  $E_F$  is further increased to above VBM  $(E_F > 0)$ ,  $S_{xx}$  reveals a sign reversal from negative to positive with increasing T. Meanwhile, the critical point  $T_C$ , where the sign change happens, gets higher for increasing  $E_F$ . All these features are qualitatively consistent with the experimental observations as shown in Fig. 6.4.

### 6.6 Discussion on the Sign Anomaly Between $R_{\rm H}$ and $S_{xx}$

In TI thin films, the thermoelectric properties are mainly contributed by charge carriers of surface states and bulk valence band states. Thus,  $S_{xx}$  can be described as  $S_{xx} = (\sigma_s S_s + \sigma_b S_b)/(\sigma_s + \sigma_b)$ , where  $\sigma_{s,b}$  and  $S_{s,b}$  represent the electrical conductivity and Seebeck coefficient of surface and bulk states.  $S_s$  is positive/negative when  $E_F$  is below/above the DP. While  $S_b$  keeps positive and gets increased as  $E_F$  is approaching the VBM and further moves into the bulk gap. Because of the gapless band structure of surface states,  $|S_s|$  is significantly smaller than  $S_b$ , which can be confirmed by the density of modes shown in Fig. 6.8. Therefore, bulk states dominate the Seebeck coefficient for low  $E_F$  or high T, giving rise to a positive  $S_{xx}$ . For a relatively high  $E_F$  in the bulk gap, the low temperature transport is mainly contributed by the metallic surface states, which introduces a small negative  $S_{xx}$ .

On the other hand, when  $E_{\rm F}$  is above the DP, the Hall coefficient  $R_{\rm H}$  is described as  $R_{\rm H} = (-\sigma_{\rm s}\mu_{\rm s} + \sigma_{\rm b}\mu_{\rm b})/(\sigma_{\rm s} + \sigma_{\rm b})^2$ , where  $\mu$  represents the charge carrier mobility. Interestingly, when  $E_{\rm F}$  is above the DP and close to the VBM where  $S_{xx} > 0$ ,  $R_{\rm H}$  is found to be negative by analyzing the charge carrier concentration and assuming  $\mu_{\rm s} \sim 12\mu_{\rm b}$  as suggested by previous experiment [18]. In general, when the surface

**Fig. 6.8** The density of modes of 5 QL  $(Bi_{1-x}Sb_x)_2Te_3$  films with x = 0.9. The abrupt increase at VBM indicates a larger  $S_{xx}$  contributed from bulk states



and bulk states have different types of charge carriers, the sign anomaly between  $R_{\rm H}$  and  $S_{xx}$  can be observed under the condition  $\mu_{\rm b}/\mu_{\rm s} \le \sigma_{\rm s}/\sigma_{\rm b} \le |S_{\rm b}/S_{\rm s}|$ , which can be achieved in TI films because  $\mu_{\rm b}/\mu_{\rm s} \ll 1 \ll |S_{\rm b}/S_{\rm s}|$  and  $\sigma_{\rm s}$  is comparable to or even larger than  $\sigma_{\rm b}$ . Therefore, in a sizable  $E_{\rm F}$  region and temperature range,  $R_{\rm H}$  and  $S_{xx}$  could be dominated by the n-type surface states and p-type bulk states, respectively.

### 6.7 Conclusion

When the  $E_F$  lies in the vicinity of VBM of the ultrathin  $(Bi_{1-x}Sb_x)_2Te_3$  TI films, the Hall effect measurements reveal that electron-like charge carriers contributed by surface states would always dominate electrical transport properties up to room temperature. However, the thermoelectric effect at high temperatures is predominately controlled by bulk band states, which always exhibit positive  $S_{xx}$  when  $E_F$  is close to VBM. The dichotomy between the electrical and the thermoelectric properties may create a new pathway for designing high-efficiency thermoelectric devices through carefully engineering the surface and bulk states in heterojunction and superlattice devices.

### References

- Zhang J, Feng X, Xu Y, et al. Disentangling the magnetoelectric and thermoelectric transport in topological insulator thin films. Phys Rev B. 2015;91:075431.
- Snyder GJ, Toberer ES. Complex thermoelectric materials. Nat Mater. 2008;7:105–14.
- Scherrer H, Scherrer S. In: Rowe DM editor. CRC handbook of thermoelectrics (Ch. 19). Boca Raton, FL: CRC Press; 1995.
- Müchler L, Casper F, Yan B, et al. Topological insulators and thermoelectric materials. Phys Status Solidi (RRL). 2013;7:91–100.

- 5. Poudel B, Hao Q, Ma Y, et al. High-thermoelectric performance of nanostructured bismuth antimony telluride bulk alloys. Science. 2008;320:634–8.
- Hicks LD, Dresselhaus MS. Effect of quantum-well structures on the thermoelectric figure of merit. Phys Rev B. 1993;47:12727–31.
- 7. Dresselhaus MS, Chen G, Tang MY, et al. New directions for low-dimensional thermoelectric materials. Adv Mater. 2007;19:1043–53.
- 8. Biswas K, He J, Blum ID, et al. High-performance bulk thermoelectrics with all-scale hierarchical architectures. Nature. 2012;489:414–8.
- 9. Venkatasubramanian R, Siivola E, Colpitts T, et al. Thin-film thermoelectric devices with high room-temperature figures of merit. Nature. 2001;413:597–602.
- Harman TC, Taylor PJ, Walsh MP, et al. Quantum dot superlattice thermoelectric materials and devices. Science. 2002;297:2229–32.
- 11. Kim Y, DiVenere A, Wong GKL, et al. Structural and thermoelectric transport properties of Sb<sub>2</sub>Te<sub>3</sub> thin films grown by molecular beam epitaxy. J Appl Phys. 2002;91:715–8.
- 12. Satterthwaite CB, Ure RW. Electrical and thermal properties of Bi<sub>2</sub>Te<sub>3</sub>. Phys Rev. 1957;108:1164–70.
- 13. Boulouz A, Chakraborty S, Giani A, et al. Transport properties of V–VI semiconducting thermoelectric BiSbTe alloy thin films and their application to micromodule Peltier devices. J Appl Phys. 2001;89:5009–14.
- 14. Hor YS, Qu D, Ong NP, et al. Low temperature magnetothermoelectric effect and magnetoresistance in Te vapor annealed Bi<sub>2</sub>Te<sub>3</sub>. J Phys Condens Matter. 2010;22:375801.
- 15. Bellaiche L, Vanderbilt D. Virtual crystal approximation revisited: application to dielectric and piezoelectric properties of perovskites. Phys Rev B. 2000;61:7877–82.
- Maassen J, Lundstrom M. A computational study of the thermoelectric performance of ultrathin Bi<sub>2</sub>Te<sub>3</sub> films. Appl Phys Lett. 2013;102:093103.
- Marzari N, Vanderbilt D. Maximally localized generalized Wannier functions for composite energy bands. Phys Rev B. 1997;56:12847–65.
- 18. Qu D-X, Hor YS, Xiong J, et al. Quantum oscillations and hall anomaly of surface states in the topological insulator Bi<sub>2</sub>Te<sub>3</sub>. Science. 2010;329:821–4.

# Chapter 7 Concluding Remarks

In this thesis, we present transport studies of topological insulator thin films. The unique electrical, magnetic, and thermoelectric properties revealed here manifest the unique physics of the massless surface Dirac fermions and the interplay between non-trivial topology and magnetism. In this chapter, we will summarize our findings and discuss the implications for future work.

### (1) Surface-state-dominated electrical transport

In 5QL  $(Bi_{1-x}Sb_x)_2Te_3$  films, with increasing Sb concentration, the transport measurements revealed a sign reversal of charge carriers from electron to hole type around the charge neutral point as well as a minimum charge density in the order of  $1 \times 10^{12}$  cm<sup>-2</sup>. This behavior is further confirmed by ARPES band mapping, in which the Dirac point moves from below the Fermi level to above it as the Sb concentration is increased. Moreover, the Dirac point is shown to be exposed in the bulk gap when the sign reversal happens. The good agreement with ARPES results suggests that the electrical transport is dominated by the surface Dirac fermions without bulk contribution. Therefore, the  $(Bi_{1-x}Sb_x)_2Te_3$  system has proved itself as one of the best candidates to achieve ideal TIs with truly insulating bulk and tunable surface states.

Future direction for the  $(Bi_{1-x}Sb_x)_2Te_3$  system is to probe the unconventional quantum Hall effect of the topological surface states. High-quality films with low carrier concentration are needed to uncover this effect under a strong magnetic field. Furthermore, by applying the idea of compositionally graded doping to the TI thin films may lead to the observation of topological exciton condensation. The manipulation of spin current can also be realized by using the spin-momentum locking in the topological surface states.

### (2) Edge-state induced quantum anomalous Hall effect

The Cr-doped (Bi,Sb)<sub>2</sub>Te<sub>3</sub> TI thin films (5 QL) have been proved to exhibit an insulating ferromagnetic phase with single dissipationless edge channel, which generates the quantum anomalous Hall effect (QAHE). By tuning the Fermi level

into the sub-band gap, the anomalous Hall resistance reaches the predicted quantized value of  $h/e^2$  in the absence of magnetic field. Most remarkably, the exact quantization is achieved on a macroscopic-scale sample with a relatively low mobility (<1000 cm²/V s) and nonzero bulk conduction. Such a robust QAHE implies that it can be used as a platform to achieve a number of applications, such as low-energy-consumption spintronic devices and quantum computation.

Future work on the QAHE is to increase the temperature at which it can be observed and generalize it to other systems. This may be achieved by attempting different kinds of dopants with larger magnetic moment and higher ferromagnetic transition temperature. Alternatively, growing ultrathin TI films on an insulating ferromagnetic substrate is also promising.

### (3) Topology-driven magnetic quantum phase transition

In 8 QL Cr-doped  $\mathrm{Bi}_2(\mathrm{Se}_x\mathrm{Te}_{1-x})_3$  films, the anomalous Hall effect measurements present a magnetic quantum phase transition from ferromagnetism to paramagnetism as the Se concentration is increased. Meanwhile, across the same critical point  $x_c$ , both ARPES measurements and density functional theory calculations reveal a topological quantum phase transition from non-trivial to trivial topology caused by the reduced spin–orbit-coupling strength with increasing Se/Te ratio. In the non-trivial regime, the effective model calculations show an increased value of  $\chi_{zz}$  arising from the enhanced van Vleck mechanism under inverted bulk bands. Therefore, the bulk band topology is the fundamental driving force for the magnetic quantum phase transition. In other words, the magnetic ground state develops following the preformed topological character, with the ferromagnetic phase resulting from the non-trivial topology and evolving to the paramagnetic phase when the bulk turns topologically trivial.

### (4) Bulk-state-dominated thermoelectric effect

The electrical and thermoelectric measurements in 5 QL  $(Bi_{1-x}Sb_x)_2Te_3$  films have displayed a sign anomaly between the Hall and Seebeck coefficients at certain Sb concentrations and temperatures. Based on the two-band model calculations (surface and bulk), we find that this anomalous effect is produced by the high-mobility surface Dirac fermions and the large bulk Seebeck effect when the Fermi level is in the vicinity of valence band maximum. Near the charge neutral point, the surface Dirac fermions dominate electrical transport properties up to room temperature and the thermoelectric effect is predominately controlled by bulk electrons at high temperatures.

Prospective investigations on gate voltage dependence of the electrical and thermoelectric properties would be more interesting and convincing. Moreover, high-efficiency thermoelectric devices could be achieved with heterojunction and superlattice structures by carefully engineering the surface and bulk states

# Appendix A Complete Transport Results of QAHE

Besides the transport results in Chap. 5, here we will show the complete data of quantum anomalous Hall effect (the same sample in Fig. 5.5). Figure A.1a, b displays the magnetic hysteresis loops of  $\rho_{yx}$  at different bottom-gate voltages ( $V_g$ s). At zero field,  $\rho_{yx}(0)$  increases from 0.5 ( $h/e^2$ ) at  $V_g = -55$  V to 1 ( $h/e^2$ ) at  $V_g = -1.5$  V and then decreases to 0.59 ( $h/e^2$ ) at  $V_g = 200$  V. Figure A.1c, d displays the MR curves at different  $V_g$ s, which show a more complex behavior.

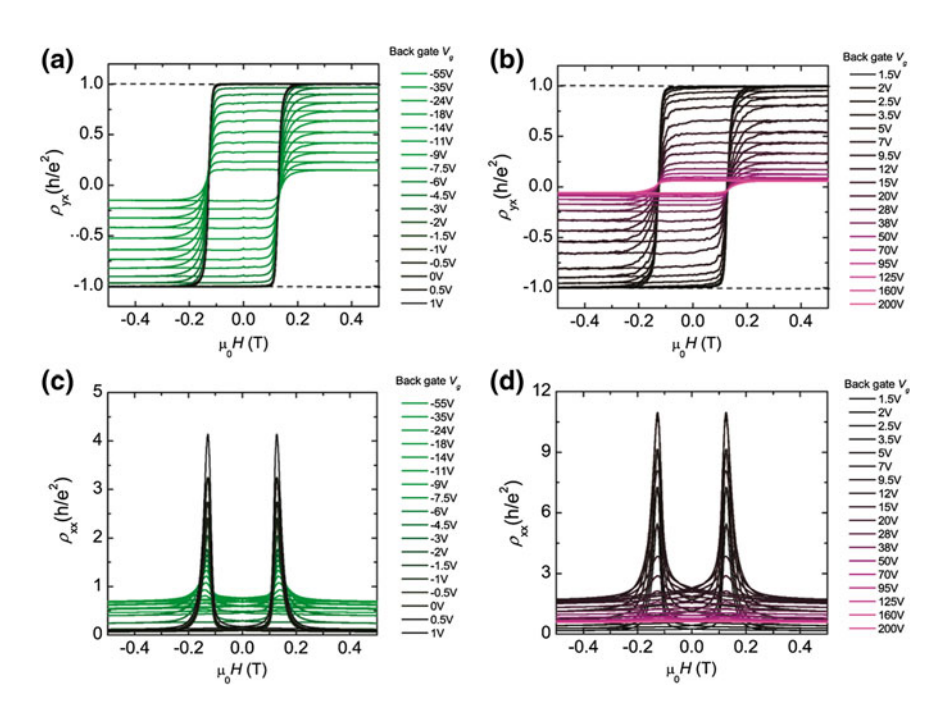


**Fig. A.1** The complete transport data on the 5 QL  $Cr_{0.15}(Bi_{0.1}Sb_{0.9})_{1.85}Te_3$  film on  $SrTiO_3$  (111) substrate. **a** Hysteresis loops of  $\rho_{yx}$  with  $V_g$  varying from -55 to 1 V. **b** Hysteresis loops of  $\rho_{yx}$  with  $V_g$  varying from 1.5 to 200 V. **c** MR curves with  $V_g$  varying from -55 to 1 V. **d** MR curves with  $V_g$  varying from 1.5 to 200 V

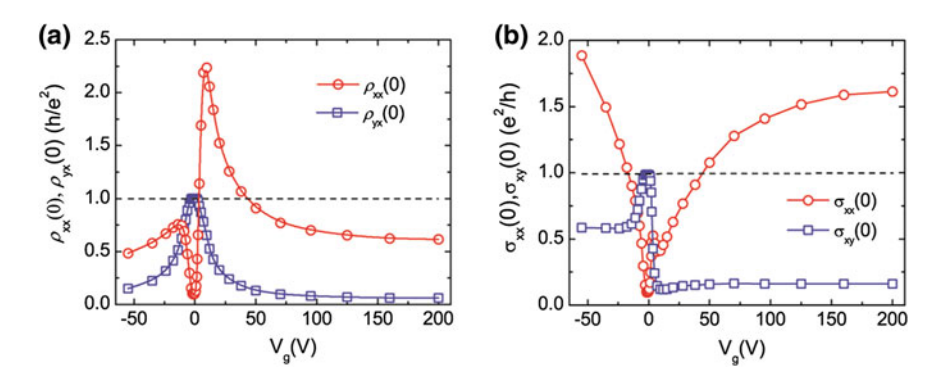


**Fig. A.2** The large-scale results of  $\rho_{yx}(0)$ ,  $\rho_{xx}(0)$  (**a**), and  $\sigma_{xy}(0)$ ,  $\sigma_{xx}(0)$  (**b**) on the dependence of  $V_g$ 

Figure A.2a presents  $V_g$ -dependent  $\rho_{yx}(0)$  and  $\rho_{xx}(0)$  with  $V_g$  varying from -55 to 200 V.  $\rho_{yx}(0)$  shows a plateau around  $V_g = -1.5$  V.  $\rho_{xx}(0)$  exhibits a double-peak structure, with a dip between two peaks also located at  $V_g = -1.5$  V. Outside the two  $\rho_{xx}(0)$  peaks,  $\rho_{yx}(0)$  and  $\rho_{xx}(0)$  basically have similar  $V_g$  dependence, which is due to  $V_g$ -induced variation in carrier density. Figure A.2b shows the corresponding zero field  $\sigma_{xy}$  and  $\sigma_{xx}$  (indicated by  $\sigma_{xy}(0)$  and  $\sigma_{xx}(0)$ , respectively). The curves exhibit similar  $V_g$  dependence with  $\rho_{yx}(0)$  and  $\rho_{xx}(0)$  near  $V_g = -1.5$  V.

## Appendix B

### Simple Picture for the Sign of AHE

In Chap. 4 of the main text, we have presented a magnetic quantum phase transition accompanied by the sign reversal of the anomalous Hall effect (AHE) across the quantum critical point (QCP) in 8 QL Cr-doped  $Bi_2(Se_xTe_{1-x})_3$  films at the base temperature. Here, we report a simple picture to understand the sign change of AHE conductance  $\sigma_{xy}$  in the *n*-doped regime.

In order to take into account the quantum confinement along z direction, an approximation is applied for the nth bulk sub-bands by treating  $\langle k_z^2 \rangle = (n\pi/d)^2$  and  $\langle k_z \rangle = 0$  (Ref. [1] in the main text). The couplings between sub-bands with different n are neglected in this approximation. We emphasize that this approximation can be used for bulk sub-band since the coupling between different sub-bands is weak once they are well-separated in energy, but it will miss surface states because the surface states originate from the linear k term in the off-diagonal part of Hamiltonian [Eq. (4.2) in Chap. 4], which is neglected. However, in the metallic regime, the main physics should be dominated by the bulk carriers so that it is useful to apply this approximation to understanding the underlying physics. Then in the basis as  $|+,\uparrow\rangle, |-,\downarrow\rangle, |+,\downarrow\rangle$  and  $|-,\uparrow\rangle$ , the Hamiltonian for the nth sub-bands is simplified as follows:

$$H_{0}(n) = \tilde{\epsilon}_{k_{\parallel}} + egin{pmatrix} \widetilde{M}(k_{\parallel}) & A_{0}ig(k_{y} + ik_{x}ig) & 0 & 0 \ A_{0}ig(k_{y} - ik_{x}ig) & -\widetilde{M}ig(k_{\parallel}ig) & 0 & 0 \ 0 & 0 & \widetilde{M}ig(k_{\parallel}ig) & A_{0}ig(k_{y} - ik_{x}ig) \ 0 & 0 & A_{0}ig(k_{y} + ik_{x}ig) & -\widetilde{M}ig(k_{\parallel}ig) \end{pmatrix},$$

$$(B.1)$$

where 
$$\widetilde{\epsilon}_{k_{\parallel}} = C_0 + C_1 (n\pi/d)^2 + C_2 k_{\parallel}^2 = \widetilde{C}_0 + C_2 k_{\parallel}^2, \\ \widetilde{M}(k_{\parallel}) = M_0 + M_1 (n\pi/d)^2 + M_2 k_{\parallel}^2 = \widetilde{M}_0 + M_2 k_{\parallel}^2, \text{ and }$$

Now it is clear that the approximated Hamiltonian is block diagonal with each block taking the form of 2D Dirac Hamiltonian, and correspondingly the four bands can be divided into two groups, one mainly consists of  $|+,\uparrow\rangle$  and  $|-,\downarrow\rangle$  components, forming the bands  $|C_1\rangle$  and  $|V_1\rangle$  as shown by the red line in Fig. B.1a, b, while the other one consists of  $|+,\downarrow\rangle$  and  $|-,\uparrow\rangle$  components, forming the bands  $|C_2\rangle$  and  $|V_2\rangle$ , as shown by the blue line in Fig. B.1a, b. The band  $|C_1(V_1)\rangle$  is related to  $|C_2(V_2)\rangle$  by TR operation. With zero magnetization,  $\sigma_{xy}$  from these two groups always takes the opposite sign and cancels each other, no matter in the inverted or normal regime. However, the  $\sigma_{xy}$  for each  $2\times 2$  block of the Hamiltonian behaves quite different for the normal and inverted regime. For the normal regime,  $\sigma_{xy}$  from one single group will drop to zero when  $\mu$  is in the gap, while it stays at some finite maximum values for the inverted regime, as shown in Fig. B.1c, d.

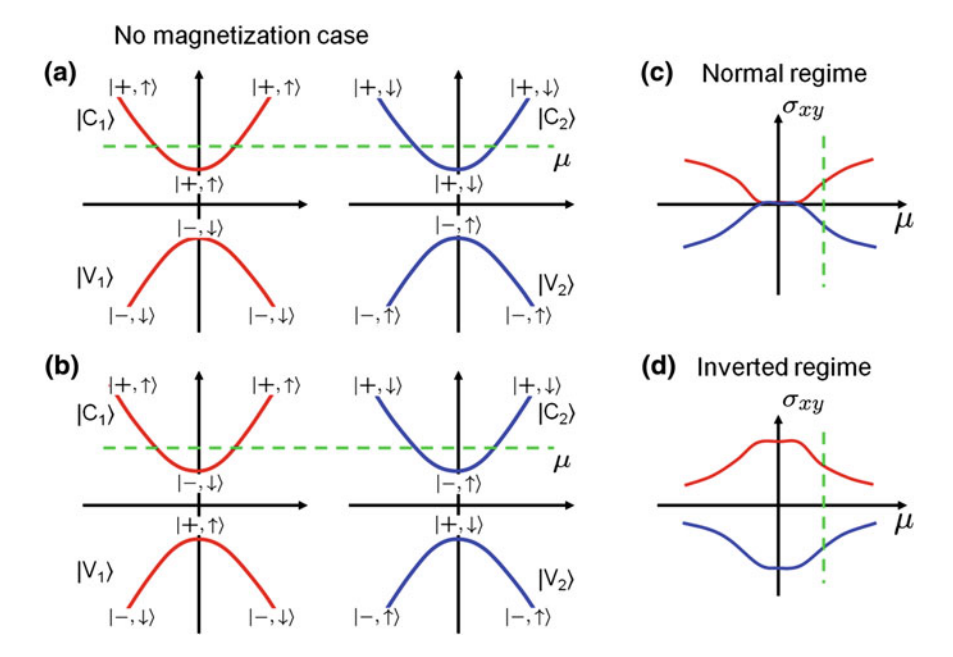


**Fig. B.1** The schematic of bulk sub-band dispersion is shown in **a** for the normal regime and **b** for the inverted case. **c**, **d** The  $\sigma_{xy}$  of each group for the normal and inverted regimes. Here, both  $G_{z1}$  and  $G_{z2}$  are zero

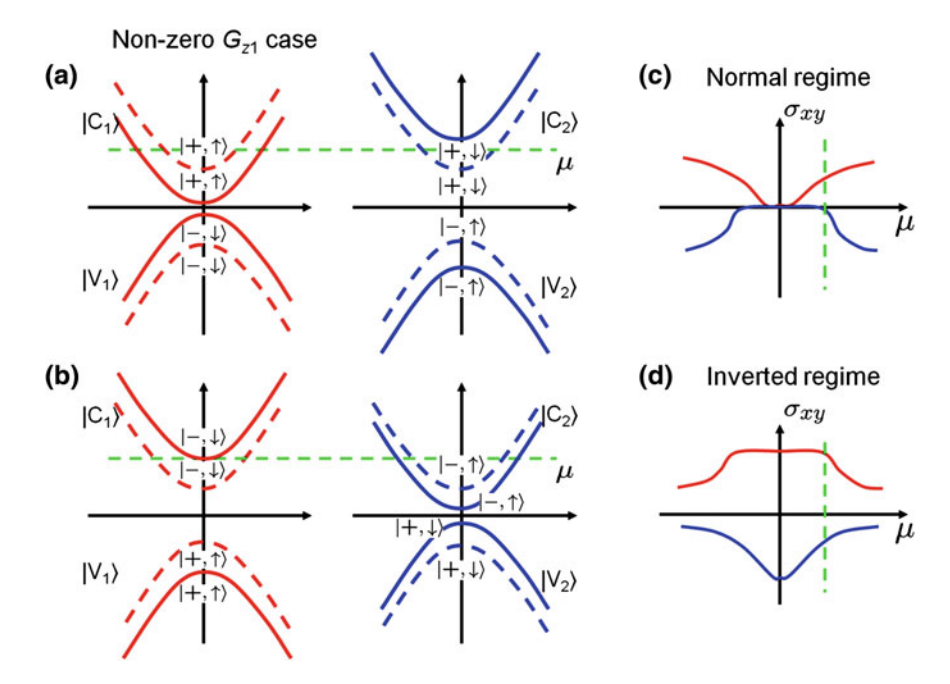
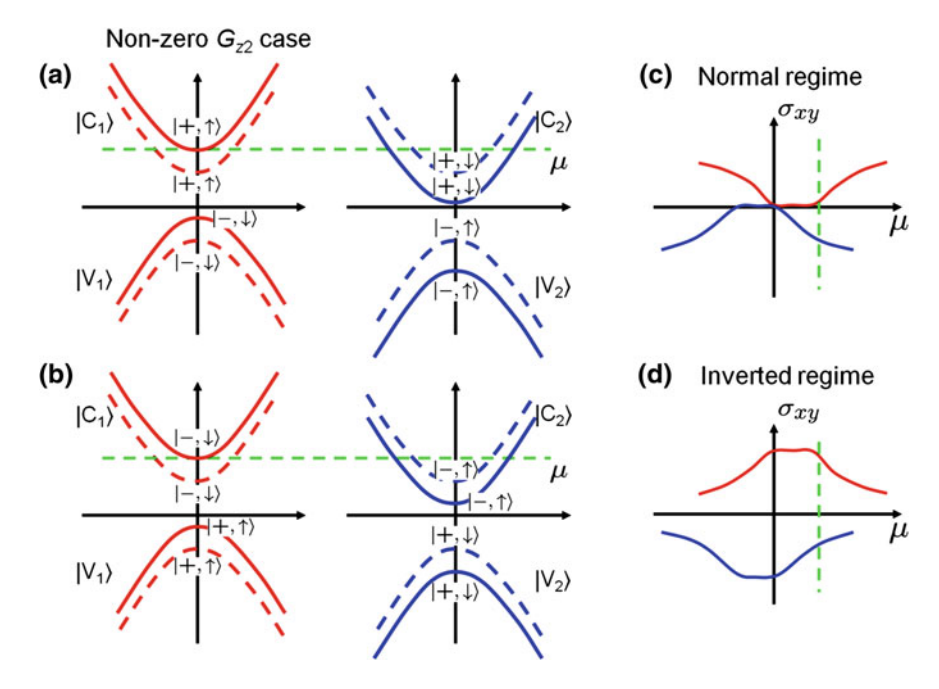


Fig. B.2 The schematic of bulk sub-band dispersion is shown in **a** for the normal regime and **b** for the inverted case. **c**, **d** The  $\sigma_{xy}$  of each group for the normal and inverted regimes. Here,  $G_{z1}$  is nonzero,  $G_{z2}$  is zero

When the ferromagnetism is introduced, the  $G_{z1}$  and  $G_{z2}$  terms should be treated separately. For  $G_{z1}$  term, it takes the opposite sign for the two states within one block in the Hamiltonian and increases the band gap for one block but decreases the band gap for the other one, as shown in Fig. B.2a, b. Consequently, it will induce different  $\mu$  dependence of  $\sigma_{xy}$  of the two blocks. However, we can see from Fig. B.2c, d that once  $G_{z1}$  is fixed, the total  $\sigma_{xy}$  always takes the same sign, no matter in the normal or inverted regime. For  $G_{z2}$  term, it has the same sign within one block and opposite sign for different blocks. Therefore, it shifts the bands in one block up and the other block down (Fig. B.3a, b). Such a shift leads to the differences between the inverted and normal regimes, and hence, the sign change of



**Fig. B.3** The schematic of bulk sub-band dispersion is shown in **a** for the normal regime and **b** for the inverted case. **c**, **d** The  $\sigma_{xy}$  of each group for the normal and inverted regimes. Here,  $G_{z1}$  is zero,  $G_{z2}$  is nonzero

the total  $\sigma_{xy}$  is shown in Fig. B.3c, d. Therefore, our simple picture here explains the numerical results for  $\sigma_{xy}$ . Compared with the experiment, our numerical results indicate that the influence of the magnetization should be dominated by the  $G_{z2}$  term. However, we do not know how the other mechanism, such as skew scattering or side jump, contributes to  $\sigma_{xy}$ , and therefore, we cannot exclude other possibilities.

### Reference

 Liu C-X, Zhang H, Yan B, et al. Oscillatory crossover from two-dimensional to threedimensional topological insulators. Phys Rev B. 2010;81:041307.